ТЕЛЕКОМУНИКАЦИЈЕ
/
TELECOMMUNICATIONS

(TE/TEI)

Eksperimentalna karakterizacija turbulencije u bežičnom optičkom kanalu

Dejan Milić, *Member, IEEE*, Jelena Anastasov, *Student Member, IEEE*, Daniela Milović i Nenad Milošević, *Member, IEEE*

***Apstrakt*— U ovom radu prikazani su eksperimentalni rezultati dobijeni u laboratorijski kontrolisanim uslovima za karakterizaciju pojave turbulencije u slobodnom prostoru pri optičkom prenosu (FSO - free space optics). Prikupljeni podaci korišćeni su za statističku karakterizaciju funkcije gustine verovatnoće (pdf - probability density function) fluktuacija optičkog signala. U literaturi postoji niz empirijskih modela za različite režime turbulencije. Dobijeni pdf je upoređivan sa odabranim modelima iz literature u cilju definisanja statističkih osobina realnog turbulentnog kanala što je značajno za proračun performansi FSO sistema. Analiza je pokazala da se rezultati dobijeni pod datim eksperimentalnim uslovima dobro poklapaju sa eksponencijalno - Vejbulovim modelom turbulencije.**

***Ključne reči*—funkcija gustine verovatnoće; FSO link; turbulencija; scintilacija.**

I. UVOD

Optičke komunikacije kod kojih se optički signali prostiru kroz slobodni prostor (FSO - free space optical communication) nude pristup optičkom delu spektra, rešavajući tako probleme sa zagušenjem radio spektra [1], [2]. Pored toga, FSO sistemi su značajni kao odgovor na sve veću potrebu za brzom bežičnom komunikacijom. Danas, FSO sistemi se upotrebljavaju u lokalnim i metro mrežama, u komunikaciji između zemaljskih stanica i satelita [3]. Često su i rešenje u prevazilaženju problema takozvane "poslednje milje", koriste se za dovođenje interneta u ruralna područja i međusobno povezivanje mobilnih baznih stanica.

Glavni nedostatak FSO sistema je slabljenje optičkog signala u slobodnom prostoru usled prisustva nepovoljnih atmosferskih uslova (kiša, sneg, uslovi slabe vidljivosti) [4]. Apsorpcija i rasejanje svetlosti u magli, oblacima, prašini i dimu značajno slabe laserski snop i ograničavaju performanse sistema i dostupnost optičke veze [1, 2, 4, 5]. Velike varijacije slabljenja mogu čak prouzrokovati relativno duge periode prekida optičke veze.

Performanse optičkog sistema koji radi u uslovima turbulencije mogu se definisati ukoliko je poznat matematički model funkcije gustine verovatnoće (pdf - probability density function) zračenja optičkog signala (scintilacije) [2], [5]. Prema tome, prvi korak u proučavanja prenosa optičkog talasa kroz slobodni prostor je identifikacija pdf-a koji opisuje promenu intenziteta signala u svim uslovima turbulencije. Tokom godina, u literaturi se pojavljuje veći broj različitih teorijskih modela [4], [6]-[12], ali još uvek ne postoji jedinstvena raspodela koja opisuje varijacije intenziteta prenosnog signala u svim režimima turbulencije.

Raspodele koje su najčešće korišćene u literaturi su lognormalna (LN - lognormal) [4], inverzna Gausova kao manje složena raspodela u poređenju sa LN raspodelom [6], takozvana Beckmanova raspodela [7], Gama-Gama (GG - Gamma-Gamma) [8], eksponencijalno-Vejbulova (EW - exponentiated Weibull) [9], [10] i Malaga (M) raspodela [11], [12]. LN model dobro opisuje optički signal u uslovima slabe turbulencije, dok je GG model odličan u uslovima srednjih do visokih turbulencija, a takođe dobro aproksimira promene signala u uslovima slabe turbulencije. Bez obzira na to što je Beckmanova raspodela pokazala dobro poklapanje sa eksperimentalnim rezultatima, zbog kompleksne matematičke forme nije bila povoljna za širu primenu u analitičkoj analizi FSO sistema. U novije vreme, kao alternativa LN i GG raspodelama, predloženi su EW i M modeli raspodele. M model je predložen kao generalni statistički model koji dobro opisuje i sferne i ravanske talase u različitim režimima turbulencije.

Neke od strategija koje se mogu koristiti za prevazilaženje scintilacionih efekata signala uključuju povećanje prenosne optičke snage, upotrebu različitih talasnih dužina, korišćenje više predajnika/prijemnika. U svakom slučaju, veoma je važno tačno opisati uslove turbulencije u FSO kanalu, kako bi se ublažili negativni efekti i poboljšale performanse posmatranog optičkog sistema. U radovima [9] i [10], EW je predložen kao pogodan model za opis realnog kanala turbulencije između krovova dve zgrade duž naseljenog terena srednje gustine u Barseloni. Prikazana je eksperimentalna i uporedna analiza sa ostalim modelima turbulencije, zajedno sa rezultatima simulacije. U radu [13], zabeležena je eksperimentalna validacija FSO kanala u priobalnom okruženju modelovanjem koeficijenta slabljenja u kanalu u zavisnosti od temperature i relativne vlažnosti vazduha, i temperature kondenzacije. Određivanje slabljenja FSO veze u uslovima tropske kiše dato je u radu [14], a eksperimentalna verifikacija modela magle u turbulentnom kanalu u laboratorijskim uslovima u radu [15].

U ovom radu prikazani su rezultati dobijeni u laboratorijski kontrolisanim uslovima u zatvorenom prostoru za

Dejan Milić – Elektronski fakultet, Univerzitet u Nišu, Aleksandra Medvedeva 14, 18115 Niš, Srbija, (e-mail: dejan.milic@ elfak.ni.ac.rs).

Jelena Anastasov – Elektronski fakultet, Univerzitet u Nišu, Aleksandra Medvedeva 14, 18115 Niš, Srbija, (e-mail: jelena.anastasov@ elfak.ni.ac.rs).

Daniela Milović – Elektronski fakultet, Univerzitet u Nišu, Aleksandra Medvedeva 14, 18115 Niš, Srbija, (e-mail: daniela.milovic@ elfak.ni.ac.rs).

Nenad Milošević – Elektronski fakultet, Univerzitet u Nišu, Aleksandra Medvedeva 14, 18115 Niš, Srbija, (e-mail: nenad.milosevic@elfak.ni.ac.rs).

modelovanje slabljenja signala u FSO kanalu. Detaljan opis eksperimenta i deo dobijenih rezultata prikazan je i u radu [16]. U eksperimentalne svrhe, korišćena je kratka turbulentna komora, dužine 3 m, napravljena od PVC cevi. Modulisani predajni signal je emitovan duž komore u kojoj su prisutni efekti turbulencije. Primljeni signal je demodulisan. Izmereni podaci su obrađeni i dobijeni histogram tj. pdf inteziteta primljenog optičkog signala upoređivan sa modelima koji su već predloženi u literaturi. Dobijeni rezultati pokazuju najbolje poklapanje sa EW raspodelom.

II. EKSPERIMENTALNA POSTAVKA

Šematski prikaz izvedenog eksperimenta dat je na Sl. 1. Postavka se sastoji od tri glavna dela:

- izvor svetlosti
- komora za turbulenciju
- fotodetektor sa sistemom za akviziciju podataka

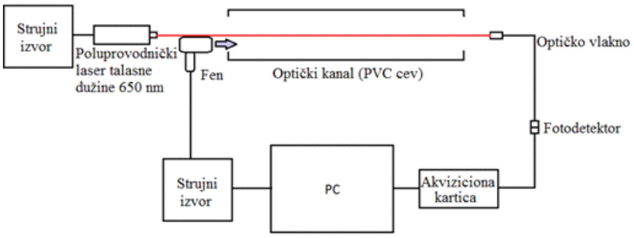

Sl. 1. Šematski prikaz eksperimenta

Na Sl. 2. prikazana je fotografija eksperimenta u Laboratoriji za telekomunikacione sisteme Univerziteta u Nišu, na Elektronskom fakultetu.

Kao izvor svetlosti korišćen je poluprovodnički laser. Talasna dužina emitovane svetlosti je 650 nm, što je u crvenom delu vidljivog spektra, pa je snop vidljiv i zbog toga se njegov položaj može lako prilagoditi. Korišćen je izvor konstantne struje za pobudu laserskih dioda. Injekciona struja je prilagođena u opsegu od nula do 50 mA, što odgovara emitovanoj optičkoj snazi između nula i 10 mW. Strujni prag laserskog zračenja je detektovan na 10,5 mA, na sobnoj temperaturi. Optička snaga izmerena je pomoću termopilot detektora koji je dostupan u laboratoriji, a merenja su potvrdila dobru stabilnost emitovane snage nakon izvesnog vremena potrebnog da se temperatura stabilizuje.

Turbulentna komora, unutrašnjeg prečnika 20 cm izgrađena je korišćenjem više međusobno povezanih PVC cevi, ukupne dužine 3 m. Duž komore raspoređena su četiri ventilatora (fena), pri čemu je svaki ventilator usmeren na osu komore, tj. na smer prostiranja laserskog snopa. Ventilatori se kontrolišu pojedinačno u smislu nivoa napona napajanja, što rezultira kontrolom brzine kojom se okreću, a time i kontrolom brzine protoka vazduha koji proizvode. Pored toga, temperaturni gradijent je dodat pomoću fena za kosu koji duva vrući vazduh na jednom kraju komore. Pored toplotnog gradijenta, fen dodaje snagu turbulencije svojim dodatnim protokom vazduha. Promenom ugla pod kojim je fen usmeren u odnosu na putanju širenja laserskog zraka mogu se postići različiti uslovi turbulencije, zahvaljujući različitim gradijentima temperature i uslovima protoka vazduha.

Sl. 2. Fotografija eksperimenta iz laboratorije

Laserski zrak pada na čeonu površinu konektora multimodnog optičkog vlakna, a zatim se vodi kratkim vlaknom do prijemnika sa PIN fotodiodom. Optički prijemnik je dizajniran i izrađen u laboratoriji i povezan sa sistemom za akviziciju. Sistem akvizicije zasnovan je na Arduino platformi i koristi svoj interni ADC (analogno-digitalni) pretvarač kako bi uzorkovao analogni signal iz prijemnika. Nakon svake konverzije, mikrokontroler prenosi podatke putem USB veze na host računar gde se podaci čuvaju za dalju obradu.

III. INTERPRETACIJA EKSPERIMENTALNIH PODATAKA

Na početku eksperimenta utvrđeni su referentni nivoi signala testiranjem kombinacije predajnik/prijemnik bez ikakvih turbulencija u prenosnom kanalu. Prijemnik je tipa visoke impedanse. ADC rezolucija je 4,9 mV. Prijemnik je ograničen nivoom šuma predpojačavača koji iznosi $40\text{nV}/\sqrt{\text{Hz}}$, a za propusni opseg koji se razmatra može se prevesti u ulaznu struju šuma od 16 nA. Zbog toga je nivo šuma prijemnika ispod granice ADC rezolucije i prijemnik je u stanju da precizno detektuje konstantnu optičku snagu.

Pojam turbulencije često se karakteriše normalizovanom varijansom fluktuacija zračenja [5] ili indeksom scintilacije, kao

$$\sigma_I^2 = \frac{\mathrm{E}[I^2]}{\left(\mathrm{E}[I]\right)^2} - 1, \tag{4}$$

gde je *I* nivo zračenja na prijemnoj strani, a E[.] je operator matematičkog očekivanja [17]. Zračenje je direktno proporcionalno izmerenoj fotostruji, a samim tim i proporcionalno procesa na izlazu sistema akvizicije, *X*. Momenti stohastičkog procesa *X* se estimitraju na osnovu skupa odmeraka $\{x_i, 1 \le i \le N\}$ i mogu se definisati na sledeći način

$$\mathrm{E}[X^k] = \frac{1}{N}\sum_{i=1}^{N} x_i^k \ , \tag{5}$$

gde je indeks scintilacije $\sigma_I^2 = \mathrm{E}[X^2]/\left(\mathrm{E}[X]\right)^2 - 1$, sve dok je proces ergodičan.

Kako se ventilatori uključuju u raznim kombinacijama, uspostavljaju se različiti uslovi turbulencije, a nivoi primljenog signala pokazuju manje ili veće varijacije. Nakon prikupljanja velikog broja uzoraka, podaci su obrađeni u cilju definisanja statističkih parametara signala. Da bismo procenili pdf koji opisuje detektovane nivoe signala, iz svake serije uzoraka konstruisan je histogram, a zatim normalizovana skala tako da se ispuniti uslov normalizacije verovatnoće (Sl. 3). Ovako dobijeni pdf je dalje upoređivan sa postojećim modelima u literaturi. Na Sl. 3, prikazane su i krive funkcije gustine verovatnoće LN, GG i EW modela.

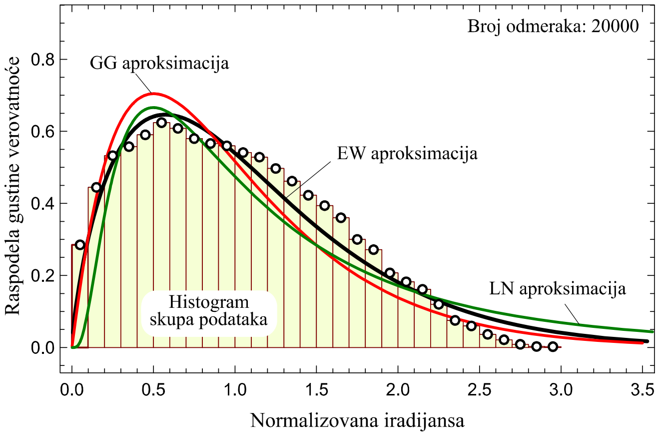

Sl. 3. Histogram prikupljenih podataka, normalizovan za procenu pdf-a Indeks scintilacije je $\sigma_I^2 = 0.3614$

IV. PREGLED MODELA TURBULENCIJE U LITERATURI

Idealan teorijski model koji opisuje promene nivoa prenosnog signala bio bi onaj koji je validan u svim režimima turbulencije, za bilo koju veličinu prijemne aperture. Potreban je zatvoreni matematički oblik modela, a da njegovi parametri budu direktno povezani sa fizičkim parametrima atmosferskih uslova. Nažalost, takav savršeni model još uvek nije poznat, ako postoji. Neki od najčešće korišćenih modela u literaturi definisani su u ovom odeljku i upoređeni sa dobijenim eksperimentalnim rezultatima u sledećem.

LN model je najčešće korišćeni model u uslovima slabe turbulencije [1], [4]. Dobijen je na osnovu prvog reda Ritove aproksimacije i pdf fluktuacija inteziteta signala ima sledeći oblik

$$p_I(x) = \frac{1}{x\sigma_i\sqrt{2\pi}} \exp\Big[-\frac{(\log x + \sigma_i^2/2)^2}{2\sigma_i^2}\Big], \quad x > 0 \qquad (6)$$

gde je σ_i^2 varijansa normalizovanog log-zračenja i $E[\log I] = -\sigma_i^2/2$. Indeks scintilacije koji odgovara LN modelu turbulencije se izračunava kao ${\sigma_{I_{LN}}}^2 = -1 + \exp(\sigma_i^2)$.

Nakagami-*m* model koji je poznat u karakterizaciji radio prenosa može se primeniti i u opisu prenosa optičkog talasa [7] kao Backman/modifikovani Rician model turbulencije. Funkcija gustine verovatnoće normalizovanog intenziteta signala, *I*, u tom slučaju, ima sledeći oblik

$$p_I(x) = \frac{1}{b}\exp\Big(-\frac{1+x}{b}\Big) I_0\Big(2\frac{\sqrt{x}}{b}\Big), \quad b, x > 0, \qquad (7)$$

gde je $I_0(.)$ modifikovana Beselova funkcija prve vrste [17]. Model je validan za indekse scintilacije ispod 2. Teorijski indeks scintilacije je ${\sigma_{I_{MR}}}^2 = -1 + \frac{2}{(1+1/b)^2} L_2(-1/b)$, gde je $L_2(x)$ Lagerov polinom drugog reda $L_2(x) = x^2/2 - 2x + 1$.

GG model turbulencije [2], [8] predstavlja stohastički model baziran na teoriji scintilacije. Ovaj model podrazumeva fluktuacije inteziteta signala kao proces modulacije koji nastaje zbog small-scale i large-scale vrtloga turbulencije. I small-scale i large scale efekti se opisuju Gama raspodelom, odakle i potiče ime ovog modela turbulencije. Konačni pdf normalizovane iradijanse, *I*, ima sledeći oblik

$$p_I(x) = \frac{2(\alpha\beta)^{(\alpha+\beta)/2}}{\Gamma(\alpha)\Gamma(\beta)} x^{(\alpha+\beta)/2-1} K_{\alpha-\beta}(2\sqrt{\alpha\beta x}), \quad \alpha, \beta, x > 0 \qquad (8)$$

gde je $\Gamma(.)$ Gama funkcija i $K_\nu(.)$ Beselova funkcija drugog reda [17]. Parametri α i β su parametri broja efektivnih large-scale i small-scale sketerera, respektivno, koji su u direktnoj vezi sa atmosferskim parametrima C_n^2 i l_0. Indeks scintilacije se može izračunati korišćenjem ${\sigma_{I_{GG}}}^2 = \big(1+\frac{1}{\alpha}\big)\big(1+\frac{1}{\beta}\big) - 1$.

M statistički model [11], [12] je predložen kao generalizovani model koji se može svesti na skoro sve prethodno pomenute modele u literaturi. Formulacija ovog modela je u vidu sledećeg pdf-a iradijanse *I*

$$p_I(x) = A^{(G)} \sum_{k=1}^{\infty} a_k^{(G)} x^{\frac{\alpha+k}{2}-1} K_{\alpha-k}\Big(2\sqrt{\frac{\alpha x}{\gamma}}\Big), \quad \alpha, \theta, \gamma, x > 0 \qquad (9)$$

gde je $A^{(G)} = \frac{2}{\gamma\Gamma(\alpha)} \left(\frac{\alpha}{\gamma}\right)^{\frac{\alpha}{2}} \big(\frac{\gamma\theta}{\gamma\beta+1}\big)^{\theta}$ i $a_k^{(G)} = \frac{(\theta)_{k-1}(\alpha\gamma)^{\frac{k}{2}}}{\big[(k-1)!\big]^2 \gamma^{k-1}(\gamma\theta+1)^{k-1}}$, a $(t)_i$ Pohamerov simbol i θ parameter Nakagami-*m* raspodele.

EW model turbulencije [9], [10] je pokazao odlično poklapanje sa rezultatima simulacije i eksperimentalnim rezultatima u uslovima slabih do srednjih turbulencija u FSO kanalu u svim uslovima usrednjavanja aperture. Još jedna karakteristika ovog modela je jednostavan zatvoreni analitički oblik pdf-a, koji se može prikazati kao [9]

$$p_I(x) = \alpha\beta x^{\beta-1} \exp(-x^\beta)\big[1 - \exp(-x^\beta)\big]^{\alpha-1}, \quad \alpha, \beta, x > 0, \qquad (10)$$

Indeks scintilacije ima oblik ${\sigma_{I_{EW}}}^2 = \frac{\Gamma(1+2/\beta) g_2(\alpha,\beta)}{\alpha\big(\Gamma(1+1/\beta) g_1(\alpha,\beta)\big)^2} - 1$, gde je

$$g_n(\alpha,\beta) = \Gamma(\alpha) \sum_{j=0}^{\infty} \frac{(-1)^j}{j!(j+1)^{1+n/\beta}\Gamma(\alpha-j)}.$$

V. EKSPERIMENTALNI REZULTATI I DISKUSIJA

Promenom uglova i brzina ventilatora dobijeni su uslovi u kanalu koji rezultiraju vrednostima indeksa scintilacije u rasponu od 0.0053 do 0.3614, koji su stoga klasifikovani kao uslovi slabe turbulencije. Uslovi jake turbulencije zahtevaju duže prenosne deonice i/ili jače ventilatore. Koristeći prikupljene podatke, vršili smo upoređivnje dobijenog modela sa modelima navedenih u prethodnom odeljku. Prikazane krive su fitovane na osnovu kriterijuma najmanje srednje kvadratne vrednosti, pozivanjem Levenberg-Markuardt algoritma [18].

Na Sl. 4 i 5 prikazane su funkcije gustine verovatnoće normalizovane iradijanse *I* za različite indekse scintilacije.

Suprotno očekivanjima, LN model je pokazao najslabije poklapanje sa dobijenim rezultatima osim u uslovima najslabije turbulencije. Ovo je posebno važno kada se razmatraju pdf repovi, jer verovatnoća repa ima veliki značaj u proceni performansi telekomunikacionih sistema. U tom delu grafika, vidno je odstupanje LN modela u odnosu na dobijeni eksperimentalni model.

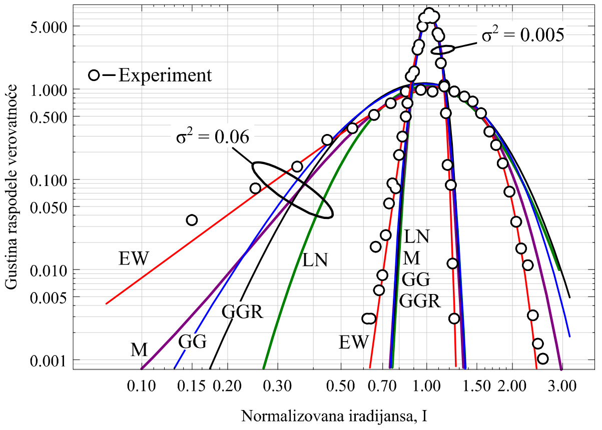

Sl. 4. Eksperimentalni rezultati dobijeni u režimu slabe turbulencije, upoređeni sa modelima iz literature kada je indeks scintilacije $\sigma_I^2 = 0.06$ i $\sigma_I^2 = 0.005$

Nešto bolje poklapanje se postiže u poređenju sa GG modelom. Razmatrana su dva slučaja: jedan koji odgovara parametrima prema Ritovoj teoriji za ravne talase (GGR), a drugi koji odgovara slobodnom izboru vrednosti parametara (GG). Primećeno je da u najslabijim uslovima turbulencije postoji mala razlika između ova dva slučaja. Sa slika se uočava bolje poklapanje sa eksperimentalnim rezultatima kada indeks scintilacije raste. Drugi razmatrani slučaj GG modela daje bolje rezultate, što dovodi do zaključka da Ritovova aproksimacija ravnog talasa nije validna u potpunosti za uslove koji se ispituju. Kada su parametri u GG modelu nezavisni, rezultati pokazuju da su fitovane vrednosti parametra α mnogo veće od vrednosti parametra β. Ovo potvrđuje da je laserski snop koji se koristi samo delimično koherentan i da je dužina koherentnosti relativno mala [19].

Sa slika se može primetiti vidno odstupanje M modela od izmerenih podataka, što ukazuje na veliku kompleksnost ovog modela. Tačnije, postoje značajne numeričke poteškoće pri pokušaju da se podaci o slaboj turbulenciji prilagode ovom opštem M modelu. Slični problemi su primećeni i za opšti GG model u uslovima slabe turbulencije.

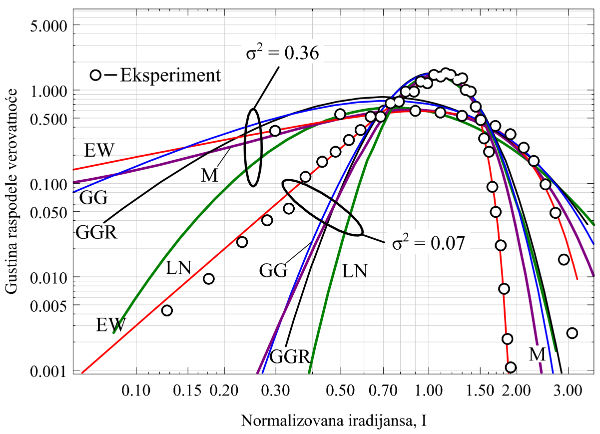

Sl. 5. Eksperimentalni rezultati dobijeni u režimu slabe turbulencije i upoređeni sa modelima iz literature kada je indeks scintilacije $\sigma_I^2 = 0.36$ i $\sigma_I^2 = 0.07$

Rezultati pokazuju da se EW raspodela najbolje poklapa sa izmerenim eksperimentalnim rezultatima. U analizi su parametri ove raspodele birani nezavisno s obzirom na to postoji ograničenja za definisanje parametara u različitim atmosferskim uslovima. Za niže vrednosti normalizovane iradijanse, EW grafik se dobro slaže sa dobijenim grafikom, dok je to slaganje za veće vrednosti *I* skoro pa odlično.

VI. ZAKLJUČAK

U ovom radu prikazan je deo originalnih rezultata dobijenih u laboratorijskim uslovima u cilju karakterizacije pdf-a iradijanse signala u FSO kanalu sa turbulencijama. Analiza je pokazala da je EW model turbulencije adekvatan matematički model za izmerene rezultate pod datim ograničenjima. Uslovi turbulencije u opisanom laboratorijskom okruženju zatvorenog prostora samo su približno reprezentativni za atmosferske uslove u realnim komunikacionim FSO sistemima. Zbog toga bi dalja istraživanja u ovoj oblasti trebalo usmeriti ka izvođenju eksperimenata u uslovima turbulencije na otvorenom i pri prenosu na dužim deonicama FSO kanala.

ZAHVALNICA

Ovaj rad je podržan od strane Ministarstva prosvete, nauke i tehnološkog razvoja Republike Srbije.

LITERATURA

[1] V.I. Tatarskii: Wave Propagation in Turbulent Atmosphere [in Russian], Moscow, SSSR: Nauka, 1967.

[2] L. Andrews, R. Philips: Laser Beam Propagation through Random Media, 2^{nd} ed., Bellingham, Washington, USA: Spie Press, 2005.

[3] M. Toyoshima, H. Takenaka, Y. Takayama: Atmospheric turbulence-induced fading channel model for space-to-ground laser communications links, Optics Express, Vol. 19, No. 17, 2011, pp. 15965 – 15975.

[4] X. Zhu, J.M. Kahn: Free-Space Optical Communication through Atmospheric Turbulence Channels, IEEE Transactions on Communications, Vol. 50, No. 8, Aug. 2002, pp. 1293 – 1300.

[5] L.C. Andrews, R.L. Philips, C.Y. Hopen: Laser Beam Scintillation with Applications, Bellingham, Washington, USA: Spie Press, 2001.

[6] N.D Chatzidiamantis, H.G. Sandalidis, G.K. Karagiannidis, M. Matthaiou: Inverse Gaussian modeling of turbulence-induced fading in free-space optical systems, Journal of Lightwave Technology, Vol. 29, No. 10, May 2011, pp. 1590 – 1596.

[7] J.H. Churnside, S.F. Clifford: Log-normal Rician probability density function of optical scintillations in the turbulent atmosphere, Journal of the Optical Society of America A, Vol. 4, No. 10, 1987, pp. 1923 – 1930.

[8] M.A. Al-Habash, L.C. Andrews, R.L. Phillips: Mathematical model for the irradiance probability density function of a laser beam propagating through turbulent media, Optical Engineering, Vol. 40, No. 8, Aug. 2001, pp. 1554 – 1562.

[9] R. Barrios, F. Dios: Exponentiated Weibull distribution family under aperture averaging for Gaussian beam waves, Optics Express, Vol. 20, No. 12, 2012, pp. 13055 – 13064.

[10] R. Barrios, F. Dios: Exponentiated weibull model for the irradiance probability density function of a laser beam propagating through atmospheric turbulence, Optics & Laser Technology, Vol.45, Feb. 2013, pp. 13 – 20.

[11] A. J-Navas, J.M. G-Balsells, J.F. Paris, A. P-Notario: A Unifying Statistical Model for Atmospheric Optical Scintillation, Numerical Simulations of Physical and Engineering Processes, InTech, DOI: 10.5772/25097, July 2011.

[12] J.M. G-Balsells, A. J-Navas, J.F. Paris, M. C-Vázquez, A. P-Notario: Novel formulation of the M model through the Generalized-K distribution for atmospheric optical channels, Optics Express, Vol. 23, No. 5, 2015, pp. 6345 – 6358.

[13] W.G Alheadary, K.-H. Park, N. Alfaraj, Y. Guo, E. Stegenburgs, T.K. Ng, B.S. Ooi, M.-S. Alouini: Free-space optical channel characterization and experimental validation in a coastal environment, Optics Express, Vol. 26, No. 6, 2018, pp. 6614 – 6628.

[14] S.A. Al-Gailani, A.B. Mohammad, U.U. Sheikh, R.Q. Shaddad: Determination of rain attenuation parameters for free space optical link in tropical rain, Optik, Vol. 125, No. 4, Feb. 2014, pp. 1575 – 1578.

[15] M. Ijaz, Z. Ghassemlooy, H. Le-Minh, S. Zvanovec, J. Perez, J. Pesek, O. Fiser: Experimental validation of fog models for FSO under laboratory controlled conditions, 24th IEEE Annual International Symposium on Personal, Indoor, and Mobile Radio Communications (PIMRC), London, UK, 8-11 Sept. 2013, pp. 19 – 23.

[16] D. N. Milić, D. M. Milović, J. A. Anastasov, "Experimental indoor validation of weak intensity fluctuations over free-space optical communication link", Serbian Journal of Electrical Engineering, Vol. 18, No. 1, February 2021, pp. 15-27.

[17] I.S. Gradshteyn, I.M. Ryzhik: Table of Integrals, Series, and Products. 6th ed., New York: Academic, 2000.

[18] J. More: The Levenberg-Marquardt Algorithm: Implementation and Theory Numerical Analysis, Springer, Berlin Heidelberg, 1977.

[19] O. Korotkova, L.C. Andrews, R.L. Phillips: Model for a partially coherent Gaussian beam in atmospheric turbulence with application in Lasercom, Optical Engineering, Vol. 43, No. 2, Feb. 2004, pp. 330 – 341.

ABSTRACT

In this paper, experimental results obtained in laboratory - controlled conditions for the characterization of turbulence over indoor free space optical (FSO) link are presented. The collected data is used for statistical characterization of the probability density function (pdf) of fluctuations of transmitted optical signal. There are several empirical models in the literature for different turbulence regimes. The obtained pdf is compared with selected models from the literature in order to define the statistical properties of the real turbulent channel, which is important in determining the performance of the FSO system. The analysis has shown that the results obtained under the given conditions coincide well with the exponential - Weibull model of turbulence.

Experimental Turbulence Characterization over Free-space Optical Communication Link

Dejan Milić, Daniela Milović, Jelena Anastasov, Nenad Milošević

Pregled postojećih DPD modela sa ograničenom širinom propusnog opsega

Tamara Muškatirović-Zekić, *Elektrotehnički fakultet Beograd, Regulatorna agencija za elektronske komunikacije i poštanske usluge,* Milan Čabarkapa, *Elektrotehnički fakultet Beograd,* Nataša Nešković, *Elektrotehnički fakultet Beograd,* Đurađ Budimir, *University of Westminster, London*

***Apstrakt*—Novi zahtevi za sve bržim i pouzdanijim servisima i uslugama putem mobilnih mreža dovode do potrebe za razvijanjem sofisticiranijih tehnika digitalne predistorzije (DPD) pojačavača (*power amplifier* - PA). Stoga je u ovom radu dat pregled postojećih DPD modela sa ograničenom širinom propusnog opsega (*band-limited* DPD). Ukratko su opisana predložena rešenja za *band-limited* DPD i data je njihova komparativna analiza. Takođe je izvedena i analiza kompleksnosti predloženih modela.**

***Ključne reči*— *band-limited* DPD, PA, LDMOS Doherty PA, LTE, PAPR, MIMO, mMIMO.**

I. UVOD

SVE je veći broj pametnih uređaja koji se putem mobilnih mreža nove generacije (4G i 5G) povezuju na Internet, pružajući korisnicima nove servise i istovremeno povećavajući potrebu za prenosom velike količine podataka, velikim brzinama. Očekuje se da će 5G pristupne mreže zahtevati signale širokog propusnog opsega, reda stotinak MHz, pa sve do nekoliko GHz [1]. Usled porasta propusnog opsega (*bandwidth*), povećavaju se i zahtevi koji se stavljaju pred pojačavač (PA), koji predstavlja najveći potrošač u predajniku, i DPD (*Digital PreDistortion*) sistem koji se koristi u cilju održavanja linearnosti i poboljšanja efikasnosti rada PA.

Kod konvencionalnih DPD sistema, potrebna širina propusnog opsega je minimum 5 puta veća od širine signala, kako bi se kompenzovala nelinearna distorzija usled širenja spektra. Razlog je taj što većina *predistorted* signala obuhvata pored osnovne komponente i intermodulacione proizvode trećeg i petog reda [2]. Tako se za signal širine 500 MHz dobija zahtevana širina propusnog opsega od 2500 MHz, odnosno brzina odabiranja DAC i ADC od 3200 Msps, za vrednost roll-of faktora od 0.28 [3]. Konvertori sa ovako velikim brzinama odabiranja su izuzetno skupo i energetski neisplativo rešenje. Cilj je realizovati širokopojasni DPD sa A/D konvertorom male brzine *(low-speed ADC*).

Na slici 1 je prikazana blok šema konvencionalnog DPD sistema.

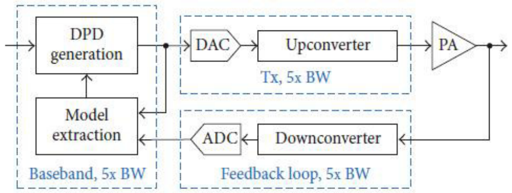

Sl. 1. Konvencionalni DPD sistem [3].

II. DPD SISTEMI SA OGRANIČENOM ŠIRINOM PROPUSNOG OPSEGA

Većina istraživača se fokusirala na smanjenje širine propusnog opsega u povratnoj grani.

U [4] i [5] je predložen *band-limited* DPD model koji rešava problem širine propusnog opsega u Tx i povratnoj grani. Kod ovog modela je *band-limiting* funkcija ubačena u *Volterra* operator u DPD modelu, kako bi se kontrolisala širina propusnog opsega izlaznog signala. *Band-limited Volterra* operator *p*-tog reda se može predstaviti sa:

$$T_p(x(n)) = D_p(x(n)) \otimes f(n) \qquad (1)$$

gde je: D_p- *Volterra* operator *p*-tog reda, *f* - *band-limiting* funkcija, a $\otimes$ predstavlja operaciju konvolucije. Za *band-limiting* funkciju je korišćen 40 MHz *low-pass complex equiripple* FIR filter. Predložen DPD model je eksperimentalno verifikovan u više testova na *high-power* LDMOS Doherty PA na 2.14 GHz. Izvršeno je poređenje konvencionalnog DPD modela sa potrebnom širinom propusnog opsega, konvencionalnog DPD modela sa ograničenom širinom propusnog opsega i predloženog DPD modela. Korišćen je WCDMA signal širine 20 MHz sa 4 nosioca i PAPR=6.5 dB. Zatim je izvršena eksperimentalna provera uticaja promene propusnog opsega sistema na performanse linearizacije, pri čemu je korišćen UMTS signal širine 60 MHz sa 12 nosioca i PAPR=6.5 dB. I na kraju je eksperimentalno proveren predložen DPD model kod sistema sa signalima šireg propusnog opsega i sa različitim kofiguracijama signala. Teorijska analiza i eksperimentalni rezultati u [5] su pokazali da ova tehnika značajno poboljšava performanse sistema i smanjuje troškove implementacije

---

Tamara Muškatirović-Zekić – Elektrotehnički fakultet u Beogradu, Bulevar kralja Aleksandra 73, 11120 Beograd, Srbija; Regulatorna agencija za elektronske komunikacije i poštanske usluge, Palmotićeva 2, 11000 Beograd, Srbija (e-mail: tamara.muskatirovic@ratel.rs)
Milan Čabarkapa – Elektrotehnički fakultet u Beogradu, Bulevar kralja Aleksandra 73, 11120 Beograd, Srbija (e-mail: milan.cabarkapa@gmail.com)
Nataša Nešković – Elektrotehnički fakultet u Beogradu, Bulevar kralja Aleksandra 73, 11120 Beograd, Srbija (e-mail: natasha@etf.rs)
Đurađ Budimir – Wireless Communications Research Group, University of Westminster, London W1W 6UW, U.K. (e-mail: d.budimir@wmin.ac.uk).

DPD, i što je još važnije, eliminiše ograničenja u pogledu propusnog opsega sistema koja postoje kod konvencionalnih DPD tehnika.

Na slici 2 je prikazana blok šema *band-limited* DPD sistema.

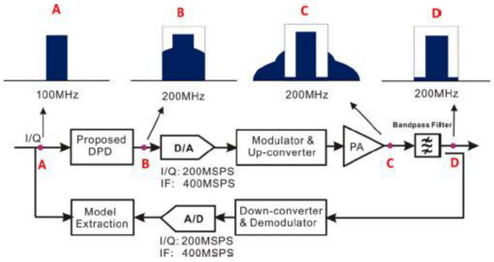

Sl. 2. *Band-limited* DPD sistem [5].

U [6] je predložen LS (*least squares*) model za procenu parametara DPD modela sa ograničenom širinom propusnog opsega, kako bi se poboljšale performanse *band-limited* DPD. Prilagođenje je izvršeno postavljanjem frekvencijskog ograničenja na širinu propusnog opsega konvencionalnog LS modela ekstrakcije. Predloženi model je eksperimentalno verifikovan na širokopojasnom *Doherty* PA izlazne snage 37 dBm, koji je dizajniran za 3G/4G sisteme. Korišćen je pojednostavljen DDR (*Dynamic Deviation Reduction*) *Volterra* model drugog reda i UMTS signal širine 40 MHz sa 8 nosioca i PAPR=6.5 dB. Primenom predloženog modela postignut je ACLR (*Adjacent Channel Leakage Ratio*) ispod -55 dBc.

Određivanje koeficijenata *band-limited* DPD modela u [7] je formulisano kao uopšten LS (GLS - *Generalized Least Squares*) problem posmatrano u frekvencijskom domenu. Ovom metodom je operacija konvolucije u vremenskom domenu zamenjena efikasnom operacijom FFT, čime je značajno smanjena računska kompleksnost. Eksperimentalni rezultati, sa WCDMA signalom širine 20 MHz i LTE signalom širine 40 MHz sa 2 nosioca, su pokazali da su performanse sa FDD-BL-DPD (*Frequency Domain Data Based Band-Limited DPD*) podjednako dobre kao sa TDD-BL-DPD (*Time Domain Data Based Band-Limited DPD*).

U [8] je predložen metod određivanja DPD parametara metodom direktnog učenja (*Direct Learning Algorithm* - DLA) sa ograničenom širinom propusnog opsega u povratnoj grani. Eksperimentalna merenja su pokazala da se predloženim algoritmom mogu postići slične performanse kao kod konvencionalnih DPD sistema, uz značajno smanjenje širine propusnog opsega u povratnoj grani.

Na slici 3 je prikazana blok šema DLA DPD sistema sa ograničenom širinom propusnog opsega u povratnoj grani.

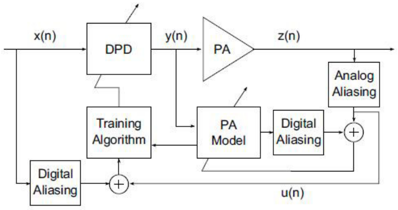

Sl. 3. DLA sa ograničenom širinom propusnog opsega u povratnoj grani [8].

U [9] je predstavljen DPD model sa ograničenom širinom propusnog opsega u povratnoj grani, kod koga se za određivanje parametara PA koristi *memory polinomial* (MP) model. Dobijeni parametri PA su zatim korišćeni u algoritmu direktnog učenja (DLA) kako bi se dobila DPD funkcija koja se zatim koristi za linearizaciju PA. Model je eksperimentalno potvrđen na LTE-A signalu širine 100 MHz sa 5 nosioca. Eksperimentalni rezultati su potvrdili poboljšanje ACLR od 22 dB, čak i kada se opseg u povratnoj grani ograniči na 100 MHz, a brzina odabiranja ADC značajno smanji na 368.64 Msps, čime se značajno smanjuju teškoće u projektovanju sistema kao i troškovi implementacije.

Na slici 4 je prikazana blok šema MP DLA DPD sistema sa ograničenom širinom propusnog opsega u povratnoj grani.

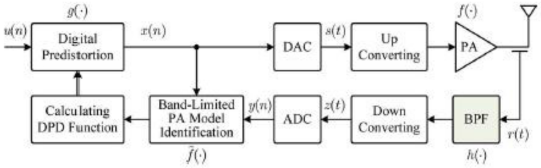

Sl. 4. MP DLA DPD sa ograničenom širinom propusnog opsega u povratnoj grani [9].

Kod DPD modela sa ograničenom širinom propusnog opsega u povratnoj grani u [10] je za određivanje parametara PA korišćen PTNTB *(Parallel Twin Nonlinear Two-Box)* model i algoritam indirektnog učenja (ILA). Eksperimentalni rezultati, na LTE-A signalu širine 100 MHz sa 5 nosioca, pokazali su da predložen model poboljšava ACLR performanse za 23 dB, čak i kada se širina propusnog opsega u povratnoj grani smanji sa 500 MHz na 140 MHz.

Na slici 5 je prikazana blok šema PTNTB ILA DPD sistema sa ograničenom širinom propusnog opsega u povratnoj grani.

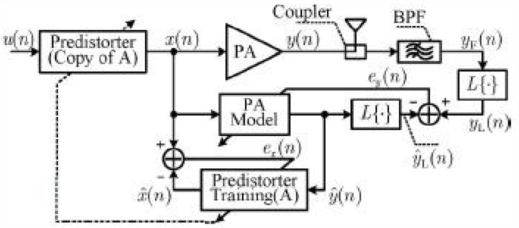

Sl. 5. PTNTB ILA DPD sa ograničenom širinom propusnog opsega u povratnoj grani [10].

Kako bi omogućili korišćenje sporih (*low-speed*) ADC konvertora, autori u [11] su predložili korišćenje spektralne ekstrapolacije signala sa ograničenom širinom propusnog opsega u povratnoj grani. Za optimalno određivanje DPD parametara korišćenog MP modela predložen je *dumped Gauss Newton* algoritam. Eksperimentalno je pokazano da širina propusnog opsega u povratnoj grani može da bude i manja od širine signala, a da se i dalje dobiju dobre performanse.

RDRS (*random demodulation based reduced sampling rate*) metod za modelovanje i linearizaciju PA, predložen u [12], značajno redukuje brzinu odabiranja u odnosu na metod spektralne ekstrapolacije, pri čemu i dalje zadržava dobre performanse. Ovaj metod koristi tehniku slučajne demodulacije u povratnoj grani sa ograničenom širinom propusnog opsega. Značajna karakteristika ove metode je ta što množenje signala pseudoslučajnom sekvencom u vremenskom domenu, širi signal preko celog spektra, pa svaka tačka na frekvencijskoj osi sadrži sve informacije o signalu. Ovo implicira da je za vraćanje signala dovoljno koristiti veoma mali deo spektra.

Na slici 6 je prikazana blok šema DPD sistema zasnovanog na slučajnoj demodulaciji (RDRS).

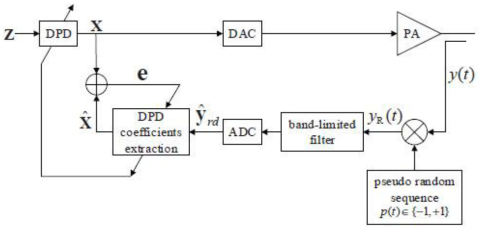

Sl. 6. RDRS DPD model [12].

DPD tehnika sa ultra malom brzinom odabiranja je predložena u [13], i sastoji se iz dva koraka. U prvom koraku se pomoću *high-rate* ulaznog signala i *low-rate* izlaznog signala iz *low-speed ADC* u povratnoj grani određuju koeficijenti modela. U drugom koraku se dobijeni model koristi za procenu *high-rate* izlaznog signala PA. Zatim se na osnovu *high-rate* ulaznog signala i procenjenog *high-rate* izlaznog signala određuju koeficijenti inverznog modela, koji se koristi za kompenzaciju nelinearnosti PA. Ovom tehnikom su značajno smanjeni zahtevi za brzinom ADC u povratnoj grani. Eksperimentalni rezultati na LTE signalu širine 40 MHz su pokazali da se predloženom tehnikom može postići smanjenje brzine ADC konvertora do čak 2.5 Msps, uz postizanje skoro iste linearizacije kao kod prethodno predloženih *band-limited* DPD tehnika, čime su značajno smanjeni zahtevi za širinom propusnog opsega u povratnoj grani.

Na slici 7 je prikazana blok šema DPD sistema sa malom brzinom odabiranja.

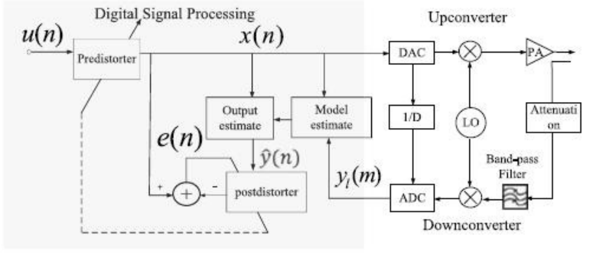

Sl. 7. DPD sistem sa malom brzinom odabiranja [13].

U cilju daljeg poboljšanja linearizacije PA za *mmWave* frekvencijski opseg, koji se nameće kao jedan od kandidata za 5G mobilne sisteme, autori u [3] su predložili DPD tehniku sa smanjenim zahtevima za širinu propusnog opsega za Tx, povratnu granu, ali i za osnovni opseg (Tx/FB/BB). Predložen DPD model koristi skup linearnih "*piecewise*" segmenata za opis nelinearnih karakteristika PA, zamenjujući operatore višeg reda sa nekoliko operatora nižeg reda. Na taj način se smanjuje zahtev za širinom propusnog opsega u osnovnom opsegu i omogućava se primena modela kod budućih ultra širokopojasnih sistema. Tehnika je eksperimentalno potvrđena na mmWave PA na 41 GHz (*in-housed designed mmWave PA module*). Testovi su vršeni sa LTE signalom širine 80 MHz sa 4 nosioca i PAPR=7.5 dB, i sa LTE signalom širine 320 MHz sa 4 nosioca i PAPR=7.5 dB.

Na slici 8 je prikazana blok šema DPD sistema za ultra-širokopojasne *mmWave* PA.

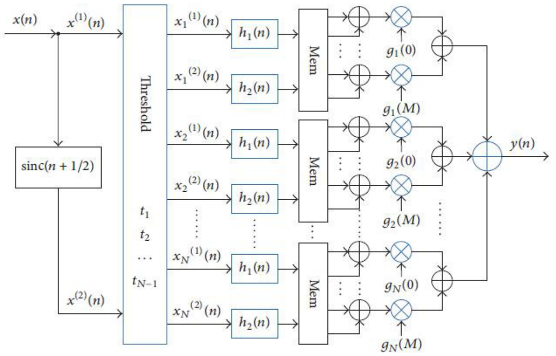

Sl. 8. DPD sistem za ultra-širokopojasne *mmWave* PA [3].

Za linearizaciju širokopojasnih RF PA u *concurrent dual-band* predajnicima u [14], predložen je BL 2-D (*band-limited two-dimensional*) DPD. Model je eksperimentalno potvrđen na *high-power* LDMOS Doherty PA na 2.14 GHz, sa izlaznom snagom od 37 dBm. *Dual-band* signal je generisan korišćenjem LTE signala širine 20 MHz i WCDMA signala širine 20 MHz sa 4 nosioca. Zbog ograničenja testnog modela, frekvencijski razmak je postavljen na 80 MHz. Maksimalna širina svakog opsega u povratnoj grani je postavljena na 80 MHz. Eksperimentalni rezultati pokazuju da predložen metod predstavlja moguće rešenje za efikasno smanjenje zahteva za širinom propusnog opsega za širokopojasne *concurrent dual-band* predajnike.

Blok šema predloženog modela prikazana je na slici 9.

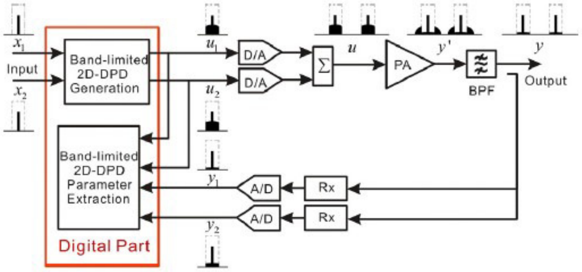

Sl. 9. *Band-limited* 2-D DPD sistem [14].

Kod klasičnog BL DPD modela, odbacivanjem signala van opsega PA dolazi do gubitka značajne količine informacija o nelinearnosti PA. Stoga su autori u [15] predložili BL DPD model sa *Band-switching* arhitekturom u povratnoj grani i ažuriranom procedurom linearizacije širokopojasnog 5G *mmWave* PA. U predloženom modelu se uzima u obzir i signal van opsega PA, korišćenjem *band-switching* arhitekture prikazane na slici 10, uz zadržavanje širine propusnog opsega ADC, kako bi se izbeglo povećanje troškova i potrošnje energije. Uveden je mehanizam za prebacivanje kojim se izdvaja ili signal unutar opsega PA ili signal van opsega PA, na osnovu unapred utvrđenog redosleda kroz odgovarajući filter. Za izdvajanje signala unutar opsega PA se koristi LPF (*low-pass* filter), dok se za izdvajanje signala van opsega PA koristi složeni BPF (*band-pass* filter), nakon što se izvrši frekvencijsko pomeranje odgovarajućim lokalnim oscilatorima. Tokom izdvajanja signala van opsega PA, levi i desni PA opsezi se frekvencijski pomeraju tako da se postavljaju jedan pored drugog kao što je prikazano na slici 10 (a) i (b) i kombinuju. Širina dobijenog signala je jednaka širini PA, čime se zadržava ista širina propusnog opsega ADC kao i u klasičnom BL DPD. Zatim se vrši analiza izdvojenih signala kako bi se ažurirali DPD koeficijenti. U prvih nekoliko iteracija, modelovanje DPD se vrši samo pomoću informacija unutar opsega PA. U narednim iteracijama, naizmenično se biraju signali unutar i van opsega PA, i zatim se vrši obrada u bloku *Error Restoration & Coefficient Estimator block*. Eksperimentalno je potvrđeno da se pomoću predloženog modela postiže ACLR od -43.6/-42 dBc i EVM<3% za *Watt-class* PA sa 256QAM modulisanim OFDM signalom širine 800 MHz u opsegu 26 GHz, pri čemu je mehanizam prebacivanja implementiran u MATLAB-u.

Blok šema predloženog DPD modela sa *Band-switching* arhitekturom prikazana je na slici 10.

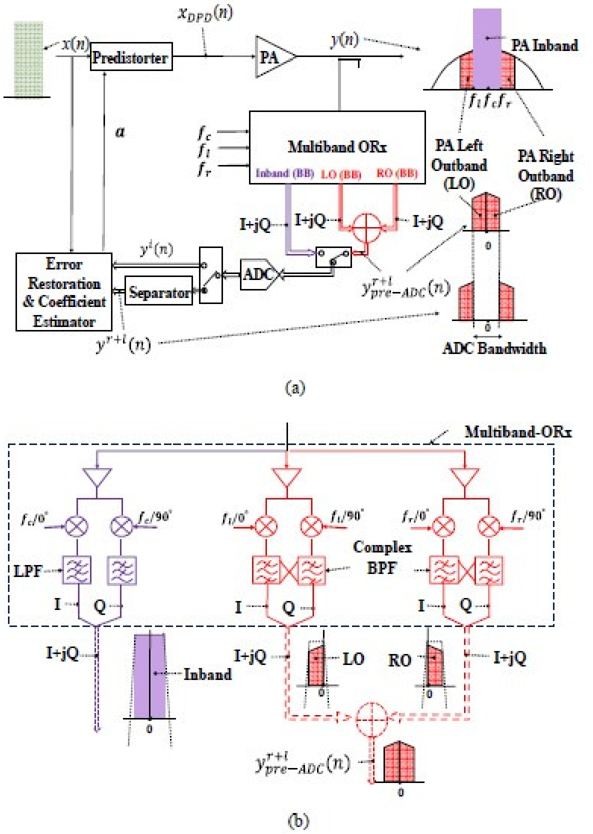

(a)

(b)

Sl. 10. BL DPD model sa *Band-switching* arhitekturom [15].

Primena BL DPD modela za hibridne MIMO predajnike analizirana je u [16]. Blok šema predloženog modela dobijena je uvođenjem *band-limiting* funkcije i predstavljena je na slici 11. Model je testiran na *parallel-Wiener* PA modelu, sa ulaznim LTE signalom širine 50 MHz i PAPR=7.6dB. Korišćen je MP DPD model čiji je red nelinearnosti 7, a dubina memorije 3. Za *band-limiting* funkciju je uzet kompleksni BPF propusnog opsega od 60 MHz. Pokazano je da predloženi model postiže performanse uporedive sa postojećim DPD metodama za hibridne MIMO predajnike, ali sa nižim brzinama ADC, čime se može značajno smanjiti cena hardvera uz zadržavanje dobrih performansi pri primeni kod *massive MIMO* (mMIMO).

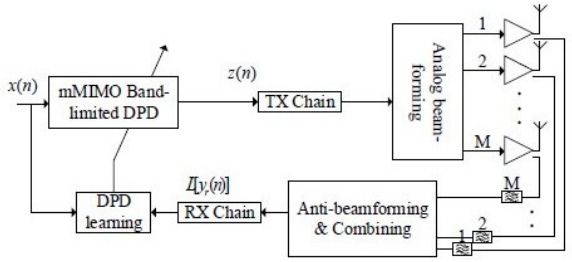

Sl. 11. mMIMO *band-limited* DPD model [16].

BL DPD model predložen u [17] vrši smanjenje propusnog opsega u osnovnom opsegu primenom linearne dekompozicije. Za razliku od modela predloženog u [13] gde se za interpolaciju koristi *sinc* funkcija koja uključuje dosta množenja, u LD (*Linear-Decomposition*) BL DPD modelu je znatno smanjena računarska kompleksnost uz zadržavanje male brzine odabiranja. Predložen model je eksperimentalno verifikovan na 5G NR test signalu u dva opsega, *sub*-6-GHz (64 QAM signal širine 100 MHz i PAPR=9.1 dB) i *mmWave* (64 QAM signal u 28 GHz, širine 400 MHz i 800 MHz i PAPR= 9dB).

Blok šema predloženog modela data je na slici 12.

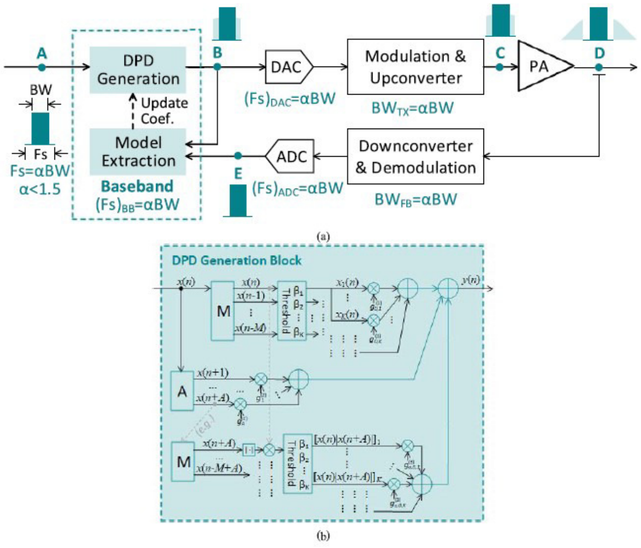

(a)

(b)

Sl. 12. LD BL DPD model [17].

III. POREĐENJE DPD MODELA SA OGRANIČENOM ŠIRINOM PROPUSNOG OPSEGA

Kompleksnost rada pri kojoj izloženi modeli dostižu izložene performanse se dosta razlikuje od modela do modela. Procena računarske kompleksnosti može se izvršiti na osnovu broja FLOP-ova (*floating point operations*). U tabeli 1 je prikazan potreban broj FLOP-ova za određene računarske operacije [18].

TABELA I
POTREBAN BROJ FLOP-OVA ZA RAČUNARSKE OPERACIJE

Operacija	***Broj FLOP-ova***
Konjugovanje	0
Kašnjenje	0
Sabiranje realnih brojeva	1
Množenje realnih brojeva	1
Sabiranje kompleksnih brojeva	2
Množenje kompleksnog i realnog broja	2
|·|^2	3
Množenje kompleksnih brojeva	6
Kvadratno korenovanje	7

Procena performansi DPD modela se može izvršiti na osnovu normalizovane srednje kvadratne greške NMSE (*Normalized Mean-Squared Error*), koja se računa po formuli:

$$NMSE = 10\log_{10}\left(\frac{\sum_{n=1}^{K}|y_{meas}(n) - y_{est}(n)|^2}{\sum_{n=1}^{K}|y_{meas}(n)|^2}\right) \quad (2)$$

gde su: y_{meas} i y_{est} - izmereni i procenjeni talasni oblici izlaznog signala, respektivno.

U tabeli 2 je dat uporedni prikaz eksperimentalno izmerenih performansi izloženih modela, kao i izračunata kompleksnost modela, pri čemu je P - red nelinearnosti, M - dubina memorije, K - dužina *band-limiting* funkcije modela, K_a i K_b - red nelinearnosti statičkog nelinearnog modela i MP modela, N - broj "*piecewise*" segmenata, N_s - broj odbiraka u svakoj sekvenci, A - dužina glavnih odbiraka.

IV. ZAKLJUČAK

Na osnovu izloženog, može se zaključiti da iako je sam koncept DPD prilično jednostavan, razvijanje jeftinog i efikasnog DPD modela za potrebe budućih širokopojasnih mobilnih sistema predstavlja veoma izazovan zadatak. Značaj ovog rada je u kompaktnom prikazu i analizi postojećih *band-limited* DPD tehnika. Budući rad ide u pravcu ispitivanja mogućnosti optimizacije i razvijanja efikasnijeg *band-limited* DPD modela.

TABELA II
POREĐENJE PARAMETARA BAND-LIMITED DPD MODELA

Referenca	***Signal***	***Širina signala [MHz]***	***PAPR [dB]***	***Širina propusnog opsega sistema [MHz]***	***ACPR [dBc]***	***NMSE [dB]***	***Kompleksnost modela***
[3]	LTE sa 4 nosioca	80	7.5	144	-47.64/-47.47	-34.63	$2\cdot(4\cdot N\cdot M+10\cdot N+1)$
	CA LTE sa 4 nosioca	320	7.5	576	-42.92/-45.04	-30.13	
[5]	WCDMA sa 4 nosioca	20	6.5	40	-60.44/-60.40	-45.83	$K\cdot\left((M+1)\cdot\frac{P+1}{2}-1\right)+3\cdot K\cdot\left(M\cdot\frac{P-1}{2}-1\right)+3$
	LTE-A sa 5 nosioca	100	7.8	140	-51.02/-52.22	-41.66	
	LTE-A sa 3 nosioca	60	7.7	140	-52.57/-53.44	-41.94	
	LTE-A + UMTS	100	9.2	140	-56.14/-57.04	-43.53	
[8]	WCDMA sa 2 razmaknuta nosioca	40	-	81.92	-59.60/-57.73	-	-
[9]	LTE-A sa 5 nosioca	100	-	100	-48	-	$2\mathrm{M}\cdot(13P-7)$
[10]	LTE-A sa 5 nosioca	100	-	140	-48	-	$4\cdot(3K_a+4M(K_b-1)-3)$
[12]	LTE	20	-	20	-52.61/-52.39	-45.77	-
[13]	LTE	40	7.0	20	-46.35/-45.59	-	-
[14]	*Dual-band* LTE i WCDMA sa 4 nosioca	20	-	40	-52.13/-51.54 – (*lower*) 51.15/-50.53 (upp*er*)	-44.46 (*lower*) -43.36 (upp*er*)	-
[15]	*256 QAM OFDM*	800	7.6	800	-43.6/-42	-	-
[16]	*LTE*	50	7.6	60	-65.16/ -64.82	-52.85	-
[17]	*5G NR sub-6GHz*	100	9.1	150	-	-35.26	$2\cdot(4\cdot N\cdot M+10\cdot N+1)$
	5G NR mmWave	400	9	600	-	-32.35	
	28GHz	800	9	1200	-	-29.52	

LITERATURA

[1] 5GPPP, "5G Vision: The 5G Infrastructure Public Private Partnership - The next generation of communication networks and services", February 2015

[2] F. M. Ghannouchi and O. Hammi, “Behavioral modeling and predistortion”, IEEE Microwave Magazine, vol. 10, no. 7, pp. 52–64, December 2009.

[3] C. Yu , Q. Lu, H. Sun, X. Wu and X.-W. Zhu, “ Digital Predistortion of Ultra-Broadband mmWave Power Amplifiers with Limited Tx/Feedback Loop/Baseband Bandwidth”, Wireless Communications and Mobile Computing, vol. 2018, March 2018.

[4] C. Yu, L. Guan and A. Zhu, “Band-Limited Volterra Series-Based Behavioral Modeling of RF Power Amplifiers”, IEEE MTT-S International Microwave Symposium, IMS ’12, pp. 1–3, Canada, June 2012.

[5] C. Yu, L. Guan, E. Zhu and A. Zhu, “Band-Limited Volterra Series-Based Digital Predistortion for Wideband RF Power Amplifiers”, IEEE Transactions on Microwave Theory and Techniques, vol. 60, no. 12, pp. 4198–4208, December 2012.

[6] L. Guan, C. Yu and A. Zhu, “Bandwidth-constrained Least Squares-based Model Extraction for Band-limited Digital Predistortion of RF Power Amplifiers” Conference Paper, in *Workshop INMMiC*, Dublin, Ireland, September 2012.

[7] G. Yang, F. Liu, C. Zhao, Z. Wang, L. Li and H. Wang, “Frequency Domain Data Based Model Extraction for Band-Limited Digital Predistortion of Wideband RF Power Amplifiers” International Journal of RF and Microwave Computer-Aided Engineering, pp. 412–420, August 2013.

[8] L. Ding, F. Mujica and Z. Yang, “Digital Predistortion using Direct Learning with Reduced Bandwidth Feedback,” in Proc. IEEE Int. Microw. Symp., pp. 1–3, Jun. 2013.

[9] Y. Liu, W. Pan, S. Shao and Y. Tang, “A New Digital Predistortion for Wideband Power Amplifiers With Constrained Feedback Bandwidth”, IEEE Microwave And Wireless Components Letters, vol. 23, no. 12, pp. 683–685, December 2013.

[10] Y. Liu, W. Pan, S. Shao, and Y. Tang, “A New Digital Predistortion Using Indirect Learning with Constrained Feedback Bandwidth for Wideband Power Amplifiers”, IEEEMTT-S Int. Microw. Symp. Dig., pp. 1–3, Jun. 2014.

[11] Y. Ma, Y. Yamao, Y. Akaiwa and K. Ishibashi, “Wideband Digital Predistortion Using Spectral Extrapolation of Band-Limited Feedback Signal” IEEE Transactions on Circuits and Systems, vol. 61, no. 7, pp. 2088–2097, 2014.

[12] W. Tao, H. Wang, C. Zhou, G. Li and F. Liu, “A Random Demodulation Based Reduced Sampling Rate Method for Wideband Digital Predistortion,” in Proceedings of the Asia-Pacific Microwave Conference, APMC ’15, China, December 2015.

[13] Z. Wang, W. Chen, G. Su, F. M. Ghannouchi, Z. Feng and Y. Liu, “Low Feedback Sampling Rate Digital Predistortion for Wideband Wireless Transmitters,” IEEE Transactions on Microwave Theory and Techniques, vol. 64, no. 11, pp. 3528–3539, November 2016.

[14] C. Yu, Y. Guo, and A. Zhu, “A Band-limited 2-D Digital Predistorter for Concurrent Dual-band RF Transmitters”, IEEE International Wireless Symposium (IWS), March 2014.

[15] S. Deb, M. Tanio, S. Hori, N. Tawa, Y. Wada, and K. Kunihiro, “Band-limited Digital Predistortion with Band-switching Feedback Architecture for 5G mmWave Power Amplifiers”, 48th European Microwave Conference (EuMC), September 2018.

[16] W. Qiao, G. Li, Y. Zhang, H. Li, and F. Liu, “A Band-limited Digital Predistortion Method for Hybrid MIMO Transmitters”, International Conference on Microwave and Millimeter Wave Technology (ICMMT), May 2019.

[17] C. Yu, Q. Lu, H. Yin, J. Cai, J. Chen, X.-W. Zhu, and W. Hong, “Linear-Decomposition Digital Predistortion of Power Amplifiers for 5G Ultrabroadband Applications”, IEEE Transactions on Microwave Theory and Techniques, vol. 68, no. 7, pp. 2833 - 2844, July 2020.

[18] A.S. Tehrani, C. Haiying, S. Afsardoost, T. Eriksson, M. Isaksson and C. Fager, “A comparative analysis of the complexity/accuracy tradeoff in power amplifier behavioral models,” IEEE Trans. Microw. Theory Tech., vol. 58, no. 6, pp. 1510-1520, June 2010.

ABSTRACT

New demands for faster and more reliable applications and services over mobile networks lead to the need of developing more sophisticated digital pre-distortion (DPD) techniques for power amplifiers (PA). Therefore, this paper provides an overview of existing band-limited DPD models. The proposed solutions for band-limited DPD are briefly described and their comparative analysis is given. An analysis of the complexity of the proposed models was also performed.

An overview of existing band-limited DPD models

Tamara Muškatirović-Zekić, Milan Čabarkapa, Nataša Nešković, Đurađ Budimir

Sistem za detekciju i klasifikaciju niskoletećih besposadnih platformi – dronova (SDKNBP)

Mohammed Mokhtari, Jovan Bajčetić i Boban Sazdić-Jotić

***Apstrakt*—Istraživanje predstavljeno u ovom radu prikazuje mogućnosti planiranog koncepta sistema za detekciju i klasifikaciju niskoletećih besposadnih platformi (dronova) zasnovanom na metodama dubokog učenja. Cilj projekta predstavlja razvoj upotrebljivog sistema koji će u realnom vremenu vršiti detekciju i klasifikaciju dronova na bazi karakteristika njihovih radio emisija. Metode detekcije i klasifikacije primenjene u ovom istraživanju zasnivaju se na konvolucionoj neuronskoj mreži istreniranoj upotrebom formirane baze snimaka radio emisija sa nekoliko vrsta komercijalno dostupnih dronova. U početnoj fazi istraživanja sistem pokazuje verovatnoću detekcije i klasifikacije od 100 % za ukupno četiri nezavisne klase – nema drona, dron 1, dron 2 i dron 3 što predstavlja osnovu za dalji razvoj sistema za detaljniju klasifikaciju.**

***Ključne reči*—Duboko učenje; Detekcija; Klasifikacija; Radio emisija; Dron.**

I. UVOD

JEDNA od najaktuelnijih oblasti tehnološkog i industrijskog razvoja današnjice je oblast razvoja i unapređenja besposadnih platformi. S obzirom na to da se autonomna vozila smatraju zamajcem četvrte industrijske revolucije, posebnu pažnju nauke, tehnologije i industrije privlače leteće besposadne platforme. One će, beskompromisno u skorijoj budućnosti zauzeti vrlo veliki i važan deo ljudske delatnosti primarno u oblasti transporta, ali i u okviru ostalih oblasti delovanja.

Terminologija označavanja niskoletećih besposadnih platformi je pretežno kod nas zastupljena na engleskom jeziku, tako da se u literaturi može naći više različitih terminoloških izraza, kao što su:

- UAS (Unmanned Aircraft System), [1];
- RPAS (Remotely Piloted Aircraft System), [2];
- UAV (Unmanned Aerial Vehicle).

U dokumentu koji koristi francuski direktorat za civilnu avijaciju [2], a taj izraz je široko prihvaćen u svetskoj naučnoj zajednici, leteća besposadna platforma je definisana kao dron, pa će se u tom kontekstu u daljem radu upravo tako i označavati.

U uslovima kada dronovi dobijaju sve više uloga – od snimanja terena, preko prenošenja male količine tereta (dostave), pa sve do mogućnosti prenosa eksplozivnih naprava, nameće se imperativ bolje kontrole ovih letelica koja se može sprovesti kroz kontrolu dela elektromagnetskog spektra u kojem dronovi vrše prenos informacije komandnim i kanalom za prenos slike. Do sada se išlo u više pravaca detekcije i klasifikacije dronova na bazi karakteristika radio emisija koje bi ih izdvojile iz velikog broja ostalih uređaja koji koriste isti frekvencijski opseg:

- Detekcija na bazi MAC (Media Access Control) adrese uređaja [3];
- Detekcija na bazi korišćenih komunikacionih protokola [4];
- Detekcija na bazi „otiska prsta“ radio emisije [5].

Svaka od navedenih metoda primenjena u anti-dron sistemu (ADRO) usled svojih ograničenja i zahteva ima prednosti i nedostatke, pa bi mogućnost implementacije više prikazanih različitih pristupa omogućilo da se dronovi u realnom vremenu detektuju, klasifikuju, lokalizuju i eventualno sprovedu protivmere ukoliko za time postoji potreba. Ovakav pristup zahteva kompromis između pravovremene detekcije, veličine prostornog okvira detekcije, verovatnoće detekcije, kao i kvaliteta i preciznosti upotrebljenih senzora. Do sada se vrlo daleko otišlo u pravcu detekcije i klasifikacije dronova na osnovu karakteristika radio signala u komunikaciji između drona i upravljačke konzole korišćenjem specifičnosti obeležja kompletnog radio saobraćaja, kao jedne u pogledu optimizacije resursa najisplativije metode. U tom pogledu postoji mnogo različitih rešenja korišćenjem metoda dubokog učenja (Deep Learning – DL) koja upotrebljavaju raznovrsne algoritme u zavisnosti od toga za koji problem detekcije i klasifikacije se traži optimalno rešenje – klasifikacija slika [6], 3D objekata [7,8], radio emisija [9, 10, 11], radarskih ciljeva [12], govora i rečenica [13, 14], gasova [15], predviđanje vrednosti akcija [16], itd.

S obzirom na činjenicu da je obučena neuronska mreža utoliko efikasnija u klasifikaciji više različitih radio emisija ukoliko je veća baza podataka pomoću koje se obučava [17], metoda na bazi dubokog učenja oslonjena na snimanjima emisija koji su praktično sprovedeni će biti predstavljena u ovom radu. Da bi se realizovalo istraživanje i razvoj sistema na bazi detekcije i klasifikacije, upotrebljavajući metode dubokog učenja, bilo je potrebno imati na raspolaganju bazu snimaka radio emisija upotrebom kojih bi se izvršio kvalitetan trening i provera (validacija) razvijenog modela koji bi kasnije bio sposoban da sa vrlo visokom verovatnoćom detektuje i klasifikuje dronove na bazi njihove radio emisije.

Mohammed Mokhtari – Vojna Akademija, Univerzitet odbrane u Beogradu, Veljka Lukića Kurjaka 33, 11042 Beograd, Srbija (e-mail: mokhtari.med91@gmail.com).

Jovan Bajčetić – Vojna Akademija, Univerzitet odbrane u Beogradu, Veljka Lukića Kurjaka 33, 11042 Beograd, Srbija (e-mail: bajce05@gmail.com).

Boban Sazdić-Jotić – Vojna Akademija, Univerzitet odbrane u Beogradu, Veljka Lukića Kurjaka 33, 11042 Beograd, Srbija (e-mail: boban.sazdic.jotic@vs.rs).

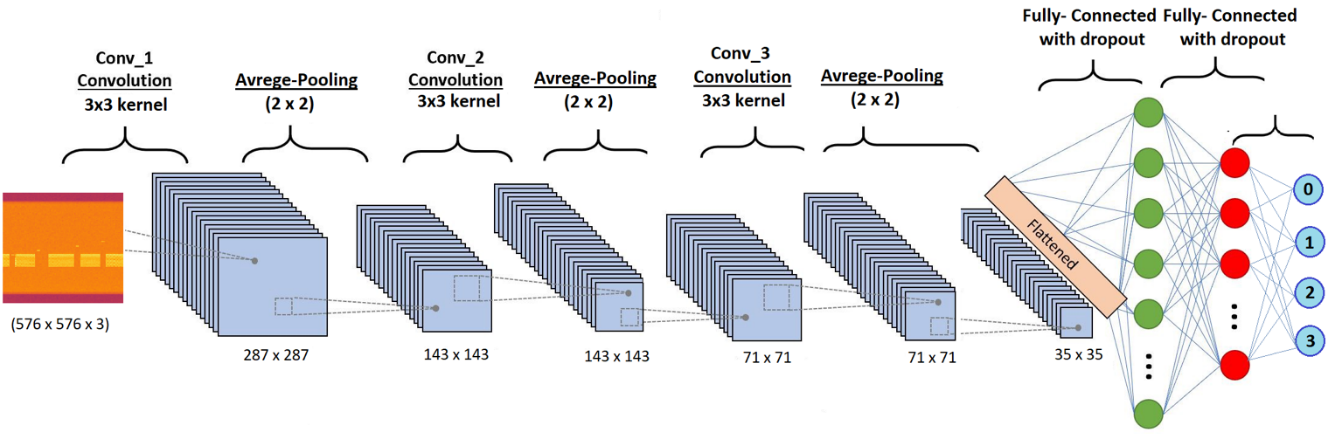

Sl. 1. Neuronska mreža upotrebljena za detekciju i klasifikaciju dronova (Prva konfiguracija)

Baza snimaka koja je korišćena u ovu svrhu [18] javno je dostupna i sadrži snimke radio emisija dronova u različitim operativnim stanjima, frekvencijskim opsezima (2,4 i 5,8 GHz), kao i snimke radio emisija kada dva i više dronova zajednički deluju na istom prostoru i u istom frekvencijskom opsegu što je čini za sada jedinom te vrste javno dostupnom.

Prikaz istraživanja u ovom radu će se sastojati iz opisa razvijenog modela na bazi dubokog učenja (poglavlje II), prikaza mogućnosti razvijenog modela (poglavlje III), opisa informacionog sistema (poglavlje IV), a na kraju, u okviru zaključka (poglavlje V) će biti rezimirane najbitnije tačke istraživanja i date smernice za buduće istraživanje.

II. OPIS MODELA ZA DETEKCIJU I KLASIFIKACIJU

Model za detekciju i klasifikaciju koji je razvijen u okviru istraživanja za početni cilj je imao da obezbedi mogućnost jednostavne detekcije i klasifikacije u okviru četiri klase događaja – nema drona, dron 1, dron 2 i dron 3. S obzirom na uslov nadograđivanja sistema za mogućnost složenije klasifikacije, polazna neuronska mreža je projektovana da bude složenija od toga da zadovolji kriterijum prvog definisanog cilja. Iz tog razloga, razvijeni model sadrži neuronsku mrežu od pet slojeva (Sl. 1.) koja je bila testirana po kriterijumu tačnosti treninga (training accuracy), gubitaka u toku treninga (training loss), provere tačnosti (validation accuracy) i gubitaka u toku provere tačnosti (validation loss) za različite slučajeve kompleksnosti ulaznih podataka. Neuronska mreža korišćena u istraživanju pripada tipu konvolucione neuronske mreže (Convolutional Neural Network – CNN), kao ulazne podatke koristi 2D slike spektrograma i predstavlja adaptaciju funkcionalne mreže sa strukturom za klasifikaciju audio signala [19]. Optimizacija mreže za slučaj klasifikacije koji je naveden svodio se na pronalaženje optimalnog odnosa između kompleksnosti i veličine ulaznih podataka (slika), verovatnoće detekcije i klasifikacije i vremena potrebnog za treniranje modela neuronske mreže. Shodno tome, vršena je optimizacija na osnovu broja odbiraka sirovog snimka i na taj način vršen uticaj na rezoluciju spektograma i dimenzije njegove slike. Uticaj rezolucije slike na performanse CNN je proučavan u literaturi [20], kao i arhitektura jednodimenzionalne konvolucione neuronske mreže (1DCNN) za detekciju i klasifikaciju UAV [21].

Formirana mreža je prilagođavana formatu ulaznih podataka (adaptirani su slojevi posledično veličini podataka koji se koriste) čije su vrednosti dobijane segmentacijom sirovih podataka iz navedene baze snimljenih radio emisija sa dronova, a vrednosti dobijene nakon segmentacije su prikazane u Tabeli I. Za svaku od četiri moguće konfiguracije je biran adekvatan broj odbiraka po segmentu čime je definisano trajanje svakog segmenta, kao i ukupan broj segmenata proistekao iz sirovog snimka. Raspodela ukupnog broja segmenata po klasama (Nema drona, Dron 1, Dron 2 i Dron 3) je predstavljena u donjem delu Tabele I. Eksperiment se svodio na četiri različita slučaja (konfiguracije), a dronovi 1, 2 i 3 su bili, respektabilno DJI Phantom IV, DJI Mavic 2 Zoom i DJI Mavic 2 Enterprise.

TABELA I
ULAZNI PODACI – SEGMENTACIJA

Konfiguracija	Broj odbiraka po segmentu	Trajanje segmenta (ms)	Ukupan broj segmenata
Prva	2796128	18.64	360
Druga	1398064	9.32	720
Treća	699032	4.66	1440
Četvrta	200319	1.34	5025
Nema drona	Dron 1	Dron 2	Dron 3
72	96	96	96
144	192	192	192
288	384	384	384
1005	1340	1340	1340

Od dobijenih segmentiranih podataka su nakon izračunavanja Furijeove transformacije (Hanning tip prozora, 2048 tačaka za FFT, 128 tačaka preklapanja, amplituda predstavljena u dB) kreirane slike spektrograma u .png formatu (Sl. 2.) prilagođene za ulaz u svaku od konfiguracija neuronske mreže (Tabela II).

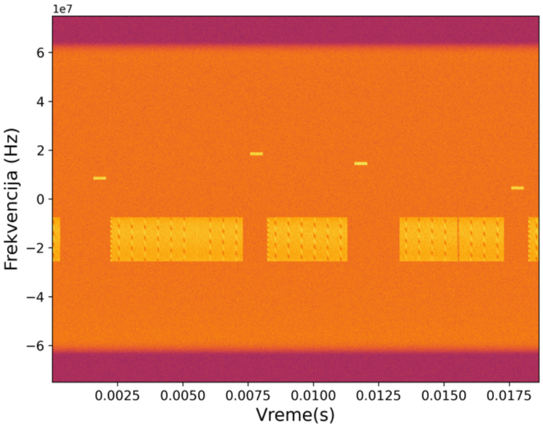

Sl. 2. Primer izgleda spektrograma

TABELA II
KARAKTERISTIKE SLIKA SPEKTROGRAMA

Konfiguracija	Rezultujuća matrica spektrograma	Rezultujuća slika (pixels)
Prva	2048 x 1456	576 x 576
Druga	2048 x 727	406 x 406
Treća	2048 x 364	288 x 288
Četvrta	2048 x 104	154 x 154

Od ukupnog broja segmentiranih podataka, 70 % je iskorišćeno za treniranje modela, a 30 % za proveru. Raspodela broja slika po skupovima, za svaku konfiguraciju je predstavljena u Tabelama III i IV. Tabela III predstavlja raspodelu slika po četiri definisane klase (Nema drona, Dron 1, Dron 2, Dron 3) za sve četiri trenirane konfiguracije. Tabela IV prikazuje raspodelu broja slika za iste četiri klase, ali za proveru tačnosti istreniranih modela za sve četiri konfiguracije.

TABELA III
PARAMETRI ZA TRENIRANJE MODELA

Konfiguracija	Ukupno slika	Nema drona	Dron 1	Dron 2	Dron 3
Prva	251	50	67	67	67
Druga	502	100	134	134	134
Treća	1005	201	268	268	268
Četvrta	3514	703	937	937	937

TABELA IV
PARAMETRI ZA PROVERU MODELA

Konfiguracija	Ukupno slika	Nema drona	Dron 1	Dron 2	Dron 3
Prva	109	22	29	29	29
Druga	218	44	58	58	58
Treća	435	87	116	116	116
Četvrta	1511	302	403	403	403

III. MOGUĆNOSTI MODELA ZA DETEKCIJU I KLASIFIKACIJU

Treniranje modela dubokog učenja izvršeno je po već navedenim podacima u ukupno 30 epoha za svaku od konfiguracija. Rezultati neimenovane jedinice tačnosti treninga (training accuracy) čija vrednost može biti od 0 do 1, a koji predstavlja odnos između broja tačnih predikcija i ukupnog broja predikcija u funkciji od broja epoha, za sve četiri konfiguracije dati su na Sl. 3. Neimenovana jedinica gubitaka u toku treninga (training loss) u funkciji od broja epoha čija vrednost može pripadati skupu $[0,\infty)$, a čija manja vrednost implicira bolju predikciju predstavljeni su na Sl. 4.

Krajnja tačnost treninga, kao i gubitaka u toku treninga za svaku od konfiguracija su predstavljeni u Tabeli V.

TABELA V
VREDNOSTI TRENIRANJA ZA SVAKU KONFIGURACIJU

Konf.	Broj epoha	Tačnost treninga	Gubici u toku treninga	Provera tačnosti	Gubici u toku provere tačnosti
Prva	30	1.00	$2.64\cdot10^{-6}$	1.00	$1.01\cdot10^{-5}$
Druga	30	1.00	$6.23\cdot10^{-4}$	0.99	0.01
Treća	30	1.00	$2.65\cdot10^{-6}$	1.00	$2.23\cdot10^{-6}$
Četvrta	30	0.97	0.11	0.97	0.12

Na osnovu prikazanog se može zaključiti:

1. Uzimajući u obzir kriterijum tačnosti treninga, prve tri konfiguracije omogućavaju klasifikaciju sa najvišom mogućom verovatnoćom, kao i sa vrlo malim gubicima u toku treninga (reda veličine 10^{-5}) što se može videti u Tabeli V;
2. U pogledu provere tačnosti, kao i u pogledu gubitaka u toku provere tačnosti, prva i treća konfiguracija daju dobre i približno slične rezultate.
3. Četvrta konfiguracija je po pitanju sva četiri kriterijuma lošija od prve tri, sa krajnjom tačnošću treninga i provere tačnosti od 0,97.
4. Model (konfiguracija) koji bi predstavljao kompromis između brzine treniranja, tačnosti i kompleksnosti (veličine) ulaznih podataka i na taj način bio optimalan za korišćenje u informacionom sistemu koji bi funkcionisao u realnom vremenu bi bio Treći model.

Matrice konfuzije na osnovu kojih se mogu ustanoviti kompletne performanse sve četiri konfiguracije, predstavljene su na Sl. 5. Ove matrice predstavljaju grafički prikaz klasifikacije po broju slika i njihovom procentualnom udelu u ukupnom broju slika koje su svrstane u određenu kategoriju (klasu). Ova klasifikacija može biti pozitivna (tačna) ili negativna (netačna), pa se na osnovu toga može zaključiti da je konfiguracija 4 najviše grešaka napravila prilikom klasifikacije emisije Dron 1 koju je svrstala u kategoriju Dron 3.

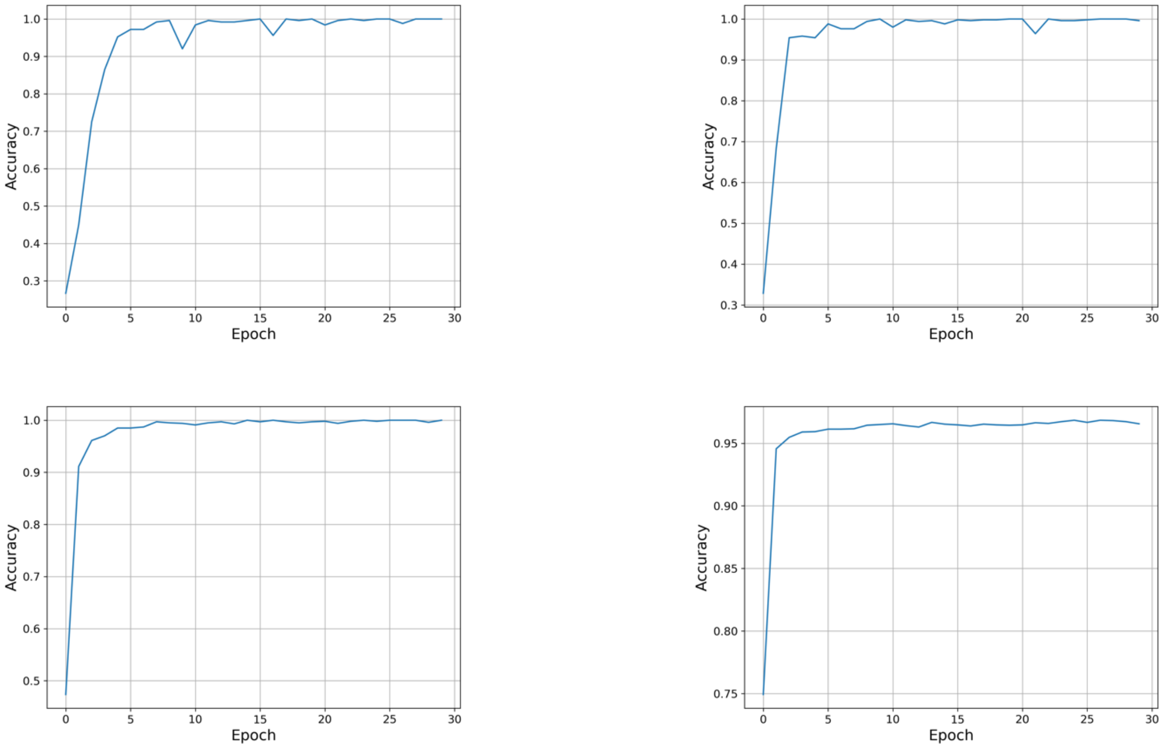

Sl. 3. Tačnost treninga (training accurracy) za konfiguracije: 1 (gore levo), 2 (gore desno), 3 (dole levo) i 4 (dole desno)

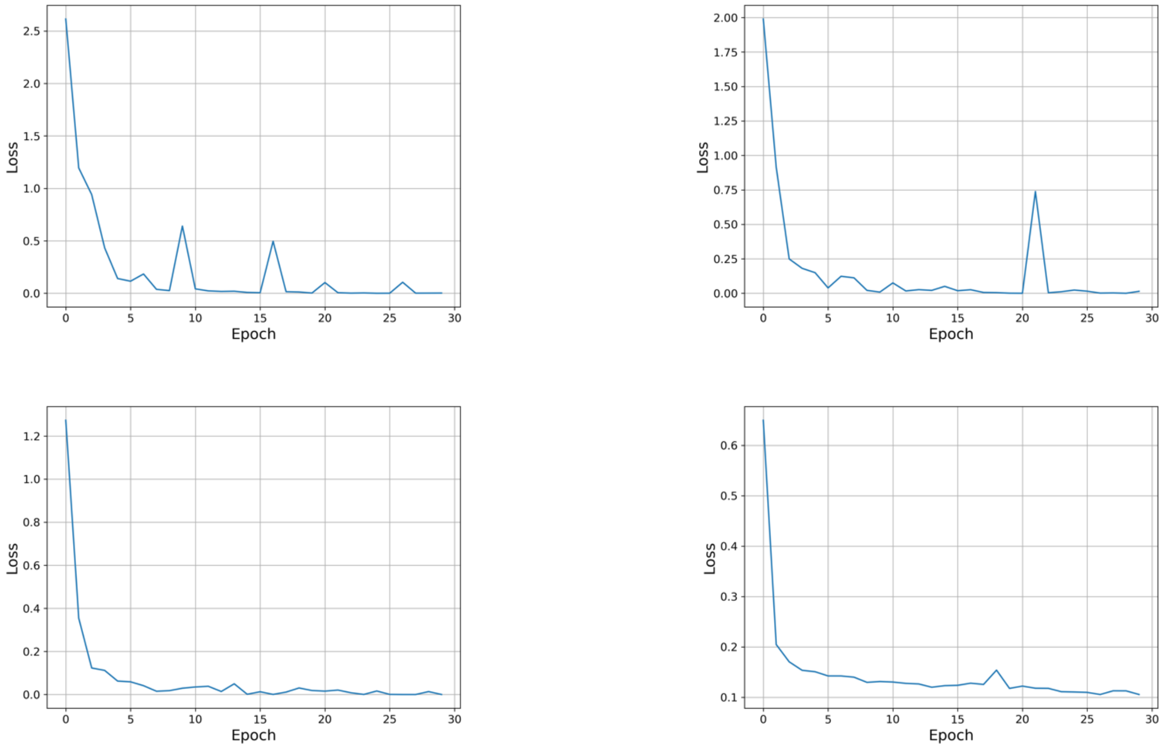

Sl. 4. Gubici u toku treninga (training loss) za konfiguracije: 1 (gore levo), 2 (gore desno), 3 (dole levo) i 4 (dole desno)

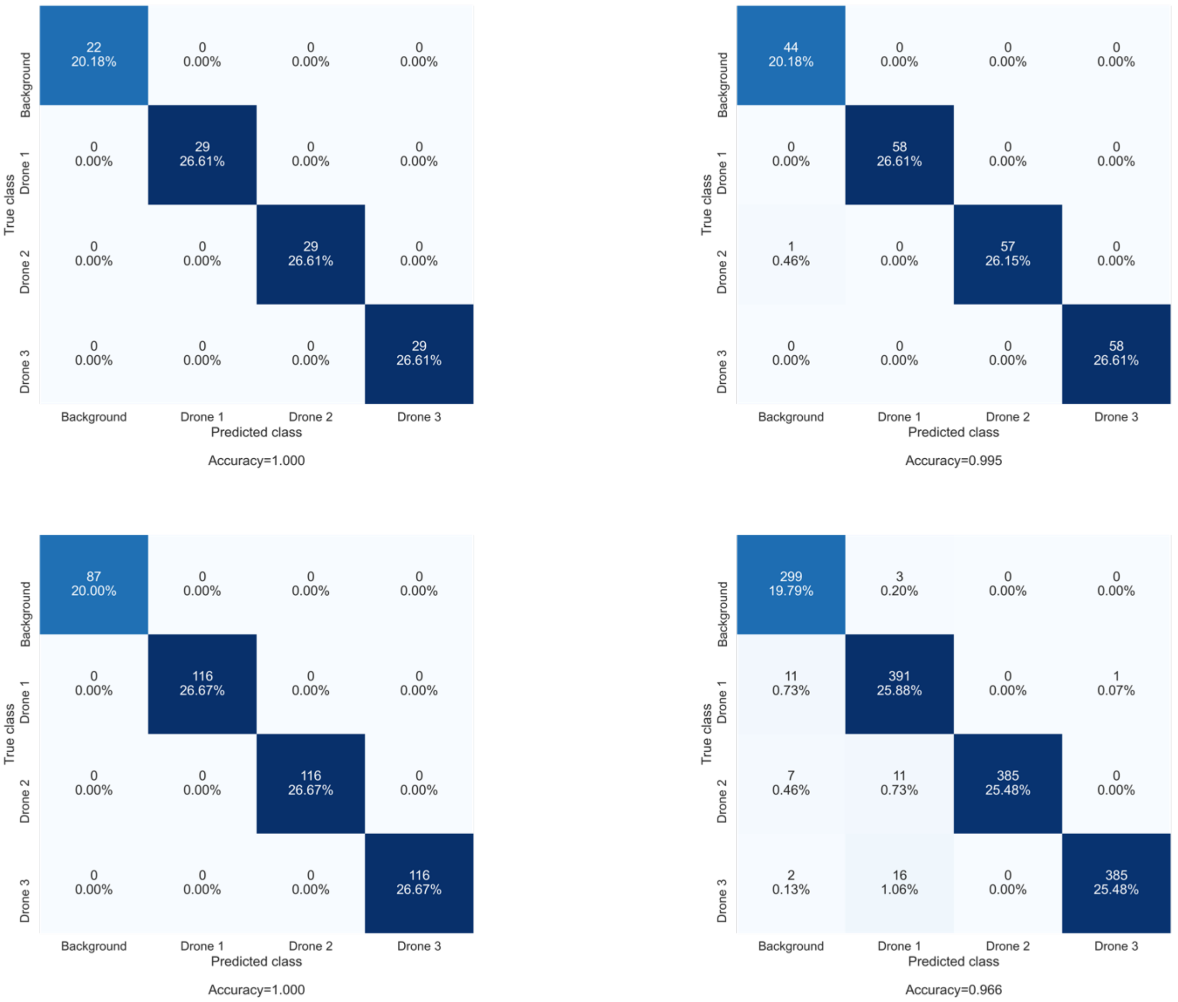

True class \ Predicted class	Background	Drone 1	Drone 2	Drone 3
Background	22 20.18%	0 0.00%	0 0.00%	0 0.00%
Drone 1	0 0.00%	29 26.61%	0 0.00%	0 0.00%
Drone 2	0 0.00%	0 0.00%	29 26.61%	0 0.00%
Drone 3	0 0.00%	0 0.00%	0 0.00%	29 26.61%

Accuracy=1.000

True class \ Predicted class	Background	Drone 1	Drone 2	Drone 3
Background	44 20.18%	0 0.00%	0 0.00%	0 0.00%
Drone 1	0 0.00%	58 26.61%	0 0.00%	0 0.00%
Drone 2	1 0.46%	0 0.00%	57 26.15%	0 0.00%
Drone 3	0 0.00%	0 0.00%	0 0.00%	58 26.61%

Accuracy=0.995

True class \ Predicted class	Background	Drone 1	Drone 2	Drone 3
Background	87 20.00%	0 0.00%	0 0.00%	0 0.00%
Drone 1	0 0.00%	116 26.67%	0 0.00%	0 0.00%
Drone 2	0 0.00%	0 0.00%	116 26.67%	0 0.00%
Drone 3	0 0.00%	0 0.00%	0 0.00%	116 26.67%

Accuracy=1.000

True class \ Predicted class	Background	Drone 1	Drone 2	Drone 3
Background	299 19.79%	3 0.20%	0 0.00%	0 0.00%
Drone 1	11 0.73%	391 25.88%	0 0.00%	1 0.07%
Drone 2	7 0.46%	11 0.73%	385 25.48%	0 0.00%
Drone 3	2 0.13%	16 1.06%	0 0.00%	385 25.48%

Accuracy=0.966

Sl. 5. Matrice konfuzije (confusion matrix) za konfiguracije: 1 (gore levo), 2 (gore desno), 3 (dole levo) i 4 (dole desno)

IV. INFORMACIONI SISTEM ZA DETEKCIJU I KLASIFIKACIJU

Produkt predstavljenog istraživanja je operativni informacioni sistem koji omogućava detekciju i klasifikaciju dronova u realnom vremenu. Ovaj jednostavni sistem je razvijen u Python programskom okruženju, proširiv je i nadogradiv za buduću upotrebu i uvezivanje sa ostalim komponentama, u skladu sa potrebama. Blok šema informacionog sistema predstavljena je na Sl. 6.

Akvizicija podataka u realnom vremenu realizuje se analizatorom spektra Tektronix RSA306B USB, a pomoću programa koji priprema i segmentuje podatke za upotrebu u Procesu 2 aplikacije – Obrada. Proces obrade koristi istreniran DL model konfiguracije 3 i u toku rada, paralelno sa prikazom detekcije u GUI (Graphic User Interface) procesu, vrši upis detekcija u MySQL bazu radi evidencije i kasnije analize.

Ovaj sistem predstavlja osnovu za razvoj kompleksnijeg informacionog sistema koji će u skladu sa klasom detekcije, vršiti određene protivmere radi zaštite ili efikasnije upotrebe dostupnog elektromagnetskog spektra u slučaju koegzistencije više besposadnih niskoletećih platformi na istom području.

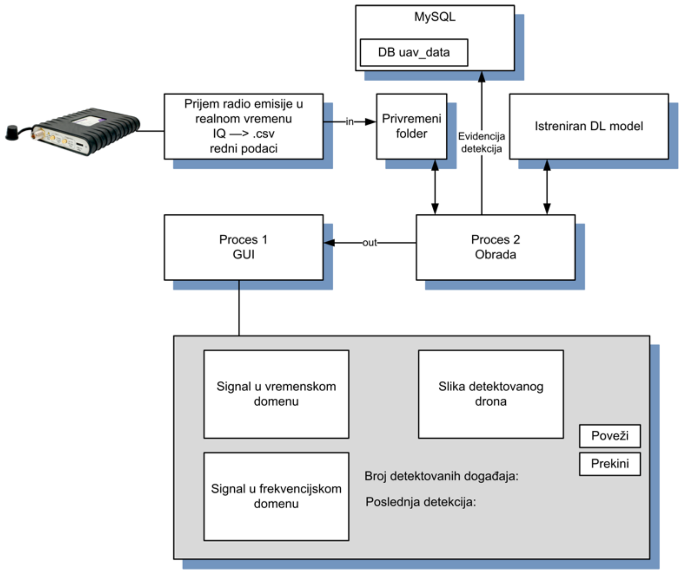

Sl. 6. Blok šema informacionog sistema za detekciju i klasifikaciju niskoletećih besposadnih platformi (SDKNBP)

V. ZAKLJUČAK

Istraživanjem predstavljenom u ovom radu došlo se do formiranja optimalnog modela dubokog učenja sposobnog da sa maksimalnom mogućom verovatnoćom klasifikuje detekcije emisija sa dronova u četiri moguće klase. Optimizacijom ulaznih parametara po strukturi i veličini, omogućena je detekcija i klasifikacija u realnom vremenu upotrebom „Real-Time“ analizatora spektra. Informacioni sistem koji je razvijen na bazi optimalnog DL modela ima mogućnost prikaza i zapisa detektovanih događaja, kao i mogućnost nadgradnje radi daljeg razvoja u željenom smeru.

Predstavljene konfiguracije predstavljaju adaptacije neuronske mreže od pet slojeva koja će u budućem istraživanju biti proširena i primenjena u razvijenom informacionom sistemu za mogućnost klasifikacije tri vrste drona u pet različitih scenarija upotrebe – nema drona (pozadinski šum), dron je povezan sa konzolom za upravljanje, dron lebdi, dron leti, dron leti i prenosi sliku.

ZAHVALNICA

Ovo istraživanje je izvedeno u okviru projekta VA-TT/3/20-22 koje finansira Univerzitet odbrane u Beogradu.

LITERATURA

[1] E. Mitka and S. G. Mouroutsos, “Classification of Drones,” *Am. J. Enginnering Res.*, vol. 6, no. 7, pp. 36–41, 2017.

[2] Altigator, “Drone, UAV, UAS, RPA or RPAS.” [Online]. Available: https://altigator.com/drone-uav-uas-rpa-or-rpas/. [Accessed: 25-Jun-2021].

[3] Peacock, M., & Johnstone, M. N. (2013). Towards detection and control of civilian Unmanned Aerial Vehicles. *Australian Information Warfare and Security Conference, June*, 1–8. https://doi.org/10.4225/75/57a847dbefb5

[4] D-Fend. (2021). *D-Fend Solutions A.D. Ltd.* https://www.d-fendsolutions.com/

[5] Nguyen, P., Ravindranatha, M., Nguyen, A., Han, R., & Vu, T. (2016). Investigating cost-effective RF-based detection of drones. *Proceedings of the 2nd Workshop on Micro Aerial Vehicle Networks, Systems, and Applications for Civilian Use, October 2018*, 17–22. https://doi.org/10.1145/2935620.2935632

[6] Krizhevsky, A., Sutskever, I., & Hinton, G. E. (2017). ImageNet classification with deep convolutional neural networks. *Communications of the ACM*, *60*(6), 84–90. https://doi.org/10.1145/3065386

[7] Nair, V., & Hinton, G. E. (2009). 3D Object Recognition with Deep Belief Nets. *Advances in Neural Information Processing Systems 22 - Proceedings of the 2009 Conference*, *22*, 1339–1347. https://proceedings.neurips.cc/paper/2009/file/6e7b33fdea3adc80ebd648fffb665bb8-Paper.pdf

[8] Pathak, A. R., Pandey, M., & Rautaray, S. (2018). Application of Deep Learning for object detection. *Procedia Computer Science*, *132*, 1706–1717. https://doi.org/10.1016/j.procs.2018.05.144

[9] Peng, S., Jiang, H., Wang, H., Alwageed, H., Zhou, Y., Sebdani, M. M., & Yao, Y.-D. (2019). Modulation classification based on signal constellation diagrams and Deep Learning. *IEEE Transactions on Neural Networks and Learning Systems*, *30*(3), 718–727. https://doi.org/10.1109/TNNLS.2018.2850703

[10] Zha, X., Peng, H., Qin, X., Li, G., & Yang, S. (2019). A Deep Learning framework for signal detection and modulation classification. *Sensors*, *19*(18), 4042. https://doi.org/10.3390/s19184042

[11] Zhou, S., Yin, Z., Wu, Z., Chen, Y., Zhao, N., & Yang, Z. (2019). A robust modulation classification method using convolutional neural networks. *EURASIP Journal on Advances in Signal Processing*, *2019*(1), 21. https://doi.org/10.1186/s13634-019-0616-6

[12] Alhadhrami, E., Al-Mufti, M., Taha, B., & Werghi, N. (2019). Learned micro-Doppler representations for targets classification based on spectrogram images. *IEEE Access*, *7*, 139377–139387. https://doi.org/10.1109/ACCESS.2019.2943567

[13] Karita, S., Watanabe, S., Iwata, T., Ogawa, A., & Delcroix, M. (2018). Semi-Supervised End-to-End Speech Recognition. *Interspeech 2018*, 2–6. https://doi.org/10.21437/Interspeech.2018-1746

[14] Kim, Y. (2014). Convolutional Neural Networks for Sentence Classification. *Proceedings of the 2014 Conference on Empirical Methods in Natural Language Processing (EMNLP)*, 1746–1751. https://doi.org/10.3115/v1/D14-1181

[15] Narkhede, P., Walambe, R., Mandaokar, S., Chandel, P., Kotecha, K., & Ghinea, G. (2021). Gas detection and identification using multimodal artificial intelligence based sensor fusion. *Applied System Innovation*, *4*(1), 1–14. https://doi.org/10.3390/asi4010003

[16] Patel, J., Shah, S., Thakkar, P., & Kotecha, K. (2015). Predicting stock and stock price index movement using Trend Deterministic Data Preparation and machine learning techniques. *Expert Systems with Applications*, *42*(1), 259–268. https://doi.org/10.1016/j.eswa.2014.07.040

[17] Mohammad F. Al-Sa’d, Abdulla Al-Ali, Amr Mohamed, Tamer Khattab, Aiman Erbad, (2019). RF-based drone detection and identification using deep learning approaches: An initiative towards a large open source drone database, *Future Generation Computer Systems*, 100, 86-97, ISSN 0167-739X, https://doi.org/10.1016/j.future.2019.05.007

[18] Sazdić-Jotić, B. M., Pokrajac, I., Bajčetić, J., Bondžulić, B. P., Joksimović, V., Šević, T., & Obradović, D. (2020). *VTI_DroneSET_FFT*. Mendeley Data. https://doi.org/10.17632/s6tgnnp5n2.1

[19] https://github.com/nageshsinghc4/Audio-Data-Analysis-Using-Deep-Learning

[20] Kannojia, S.P., & Jaiswal, G. (2018). Effects of Varying Resolution on Performance of CNN based Image Classification An Experimental Study, *International Journal of Computer Sciences and Engineering,* 6 (9), 451-456, E-ISSN 2347-2693, https://doi.org/10.26438/ijcse/v6i9.451456

[21] Al-Emadi, S., Al-Senaid, F. (2020). Drone Detection Approach Based on Radio-Frequency Using Convolutional Neural Network, *2020 IEEE International Conference on Informatics, IoT, and Enabling Technologies (ICIoT)*, 29-34, https://doi.org/10.1109/ICIoT48696.2020.9089489

ABSTRACT

The research which is described in this paper presents the potentials of the Drone Detection and Classification System (DDCS) proposed concept which is based on Deep Learning (DL) methods. The aim of the project is the development of the operational system which would be capable of real time drone detection and classification based on their radio emission characteristics. Detection and classification methods used in this research are built with developed convolutional neural network which is trained using the formed radio emission database consisted of recordings originated from several commercially available drones. The initial testing of the research results shows 100 % detection and classification probability for four independent classes – no drone, drone 1, drone 2 and drone 3 which is a good basis for a future more detailed classification development.

Drone Detection and Classification System (DDCS)

Mohammed Mokhtari, Jovan Bajcetic and Boban Sazdic-Jotic

Evaluacija dometa LoRa IoT primopredajnika u urbanom i ruralnom okruženju

Dejan N. Milić, *Member, IEEE*, Slavimir Stošović, Dejan Stevanović i
Jelena Anastasov, *Student Member, IEEE*

***Apstrakt*—U ovom radu su prikazani praktični rezultati merenja nivoa signala prilikom prenosa podataka korišćenjem platforme tipa LoRa. Iako je ciljna primena ovakvih platformi na prvom mestu internet inteligentnih objekata u urbanim okruženjima, u radu je razmotrena i mogućnost njihove primene u ruralnim okruženjima. Jedna od ideja za primenu tehnologije jeste praćenje živog sveta u okruženjima koja se nalaze van naseljenih oblasti. Domet radio veze u ovakvom okruženju može biti znatno veći nego u urbanoj sredini, zavisno od uslova optičke vidljivosti i prepreka koje se nalaze na liniji između predajnika i prijemnika. Dobijeni rezultati pokazuju da se pri povoljnim uslovima zadovoljavajući rezultati prenosa mogu dobiti i na udaljenostima većim od 10 km.**

***Ključne reči*—prostiranje RF signala; LoRa; IoT, feding; efekat senke.**

I. UVOD

INTERNET inteligentnih objekata (*Internet of Things* - IoT) predstavlja koncept mreže za prenos podataka unutar koje su objekti opremljeni senzorima, softverom i uopšte – neophodnom tehnologijom u cilju razmene podataka između uređaja i sistema, preko interneta [1], [2]. Ovakav koncept je ponikao iz konvergencije više različitih tehnologija, pri čemu je ključna sposobnost komunikacija između objekata unutar mreže, kao i objekata i infrastrukture. Ove sposobnosti mogu uspešno omogućiti različite tehnologije bežičnih komunikacija [3], od kojih najvažnije spadaju u tri kategorije prema svom dometu: tehnologije kratkog, srednjeg i većeg dometa. U tehnologije kratkog dometa se ubrajaju Bluetooth, NFC, RFID, Wi-Fi, ZigBee i slične tehnologije koje imaju domet prenosa do desetak metara udaljenosti. U kategoriju tehnologija srednjeg dometa spadaju npr. LTE ili 5G, obzirom da omogućavaju pristup u okviru nekoliko stotina metara, odnosno do najbliže bazne stanice. Sa druge strane, tehnologije većeg dometa mogu biti npr. LoRa, [4], NB-IoT i slične, koje mogu omogućiti domet u krugu od nekoliko kilometara.

U ovom radu smo eksperimentalno testirali prenos LoRa modula namenjenih za IoT sisteme većih dometa. Cilj testiranja jeste okvirna procena dometa ovakvih uređaja, uzimajući u obzir karakteristike prenosnog kanala [5]-[7], u dva scenarija korišćenja:

- u urbanim uslovima, odnosno uslovima koji podrazumevaju prostiranje u urbanim sredinama i zatvorenom prostoru, i
- u ruralnim uslovima, odnosno uslovima koji se odnose na otvoreni prostor i optičku vidljivost u širokom opsegu pokrivanja.

Ove informacije su neophodne kako bi se za odgovarajuću konkretnu primenu odabrala neophodna tehnologija bežičnog pristupa i sagledala izvodljivost zacrtanih ciljeva.

Struktura ovog rada je seledeća: nakon uvoda, sledi odeljak II u kome su opisani relevantni delovi korišćenog hardvera. U odeljku III predstavljena su merenja koja se odnose na evaluaciju antene, dok su odeljci IV i V posvećeni rezultatima dobijenim u urbanoj i ruralnoj sredini, respektivno. Zaključak rada sažeto je dat u poslednjem odeljku VI, nakon koga sledi zahvalnica i spisak korišćene literature.

II. HARDVER

Hardver koji je korišćen kao test platforma je osnova projekta CANANDI, čiji je cilj realizacija komercijalnog sistema namenjenog praćenju lovačkih pasa u ruralnoj sredini. Canandi sistem se sastoji od ogrlice koju nosi pas, prijemnika koji se nalazi kod vlasnika psa i mobilne aplikacije. Komunikacija između ogrlice psa i prijemnika koji se nalazi kod vlasnika zasnovana je na tehnologiji koja podržava LoRa standard. Canandi pomaže vlasnicima da u svakom trenutku znaju lokaciju njihovih pasa, pri čemu predstavlja inovativno rešenje na tržištu jer sadrži nekoliko jedinstvenih odlika:

- Dvostruki način prenosa signala (LoRa, GSM) za povećanje pouzdanosti sistema
- IoT komunikaciona mreža između lovaca na terenu koja omogućava deljenje i korišćenje podataka za zajedničko praćenje izgubljenog psa
- Mašinsko učenje u analizi prikupljenih podataka i davanje korisnih saveta lovcima za unapređenje obuke pasa.

Primopredajnik je u osnovi komercijalno dostupan pod oznakom RFM95W, a prototip koji je korišćen u testu je realizovan sa pomenutim modulom primopredajnika. Predajni modul sadrži izlazni pojačavač snage koji je projektovan po kriterijumu optimalne efikasnosti, pri čemu tipično može da obezbedi snagu od 25 mW, odnosno +14 dBm na izlazu, kada je izlazno opterećenje realna otpornost od 50 Ω. Pored

---

Dejan N. Milić – Elektronski fakultet, Univerzitet u Nišu, Aleksandra Medvedeva 14, 18000 Niš, Srbija (e-mail: dejan.milic@ elfak.ni.ac.rs).

Slavimir Stošović – Akademija tehničko-vaspitačkih strukovnih studija Niš, 1800 Niš, Srbija (e-mail: slavimir.stosovic@akademijanis.edu.rs).

Dejan Stevanović, Elektronski fakultet, Univerzitet u Nišu, Aleksandra Medvedeva 14, 18000 Niš, Srbija (e-mail: stevanovic_dejan@yahoo.com).

Jelena Anastasov – Elektronski fakultet, Univerzitet u Nišu, Aleksandra Medvedeva 14, 18000 Niš, Srbija (e-mail: jelena.anastasov@ elfak.ni.ac.rs).

standardnih formata modulacije zasnovanih na digitalnoj amplitudskoj i frekvencijskoj modulaciji - OOK, FSK, GFSK i GMSK, koji obezbeđuju kompatibilnost sa postojećim standardima - IEEE802.15.4g i bežičnim MBUS standardom, modul ima i podršku za LoRa modulaciju/demodulaciju. Modulacija koju koristi LoRa se zasniva na prenosu signala sa proširenim spektrom, pri čemu LoRa predstavlja derivativ tehnike proširenog spektra sa frekvencijskim čirpom (CSS). Prednosti koju ovakva vrsta modulacija ima nad standardnim digitalnim modulacijama se ogledaju u boljoj osetljivosti prijemnika, koja može biti i ispod nivoa šuma ulaznog stepena, zatim u boljoj selektivnosti i smanjenju kanalne interferencije, kao i u boljim karakteristikama u pogledu efekta fedinga.

III. ANTENA

Antena predstavlja osnovu gotovo svakog IoT projekta koji koristi bežične komunikacije. Sistem bežičnog radio prenosa suštinski zavisi od antene kao interfejsa koji je nepohodan kako bi se radio talasi efikasno emitovali u prostor izvan predajnika. Uobičajeno je da se sistem prenosa, uključujući antenu, projektuje na početku, a da se nakon toga dodaju ostali elementi sistema.

U konkretnom slučaju realizovanog prototipa antena je zamišljena kao eksterni element, a štampana ploča je realizovana tako da linija koja vodi od izlaznog stepena do konektora antene bude veoma kratka. S obzirom da u samom početku nije obavljen izbor konkretne antene, već je ostavljena sposobnost testiranja različitih mogućnosti, izlazni port antene je zamišljen kao U/FL konektor na koji je moguće priključiti različite antene radi daljeg testiranja. Sa druge strane, konkretna namena uređaja ima određena ograničenja u pogledu dimenzija, tako da je prototip korišćen prilikom testiranja umesto direktnog montiranja antene imao opciju napojnog voda koji sa jedne strane ima U/FL konektor, a sa druge strane SMA konektor koji se montira na plastično kućište uređaja.

Antena koja je korišćena u ovom testu je monopol antena niske nabavne cene, sa ravnim SMA konektorom, prikazana na slici 1.

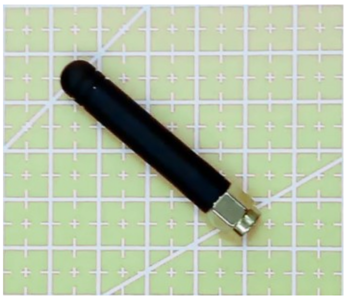

Sl. 1. Eksterna antena uređaja.

Obzirom da monopol antena zahteva ravan uzemljenja koja u ovom prototipu nije predviđena, intuitivno se može pretpostaviti da njene karakteristike nisu optimalne. Zbog toga smo najpre obavili merenje impedanse ove antene u konfiguraciji sa koaksijalnim napajanjem, bez postojanja ravni uzemljenja. Dobijeni rezultati su prikazani na slici 2. Sa slike se vidi da na frekvenciji 868 MHz impedansa antene iznosi oko 250 Ω. Impedansa je primarno realna, dok imaginarni deo impedanse iznosi oko -100 Ωi.

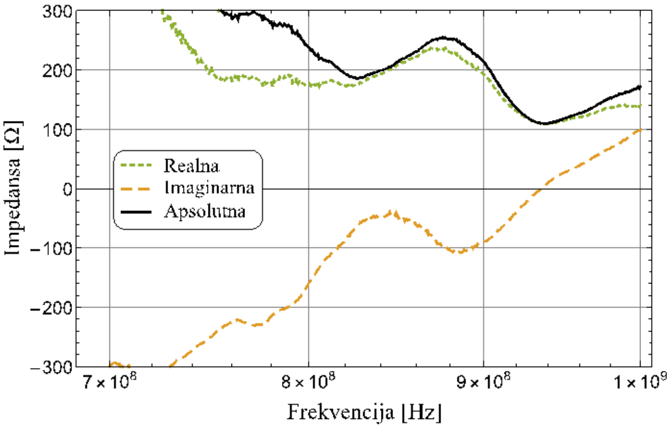

Sl. 2. Realni i imaginarni deo imedanse antene, izmereni u odsustvu ravni uzemljenja.

Kako u realizaciji projekta još uvek nije donesena odluka o korišćenju konkretne antene, dalji koraci ka prilagođenju antene nisu preduzimani i testiranje prototipa je nastavljeno bez implementacije kola za prilagođenje. Jedan od faktora koji doprinosi ovakvoj odluci jeste i koaksijano napajanje antene

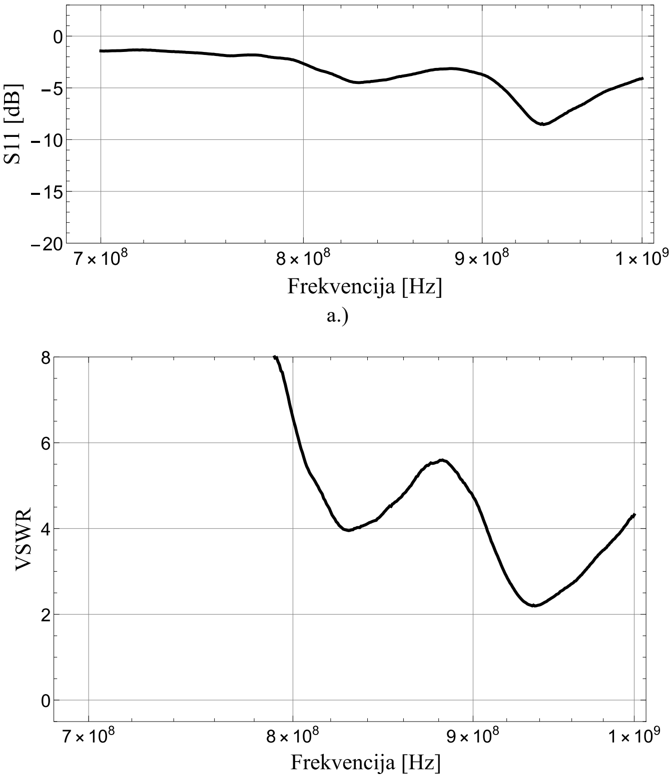

a.)

b.)

Sl. 3. a) Koeficijent refleksije i b) naponski koeficijent stojećih talasa.

putem RG174 kabla čija dužina nije precizno kontrolisana, tako da bi prilagođenje moralo da se posebno projektuje za svaki od uređaja na osnovu izmerenih vrednosti impedanse. Imajući ove činjenice u vidu, izmerene su karakteristike refleksije za konkretni slučaj i rezultati su prikazani na slici 3.

Slika 3. pokazuje da koeficijent refleksije, S_{11}, gledano od strane SMA konektora iznosi oko -3 dB, što odgovara naponskom koeficijentu stojećih talasa od 5.5. Iako ove vrednosti nisu blizu optimalnih, iz pomenutih razloga kolo za prilagođenje nije dalje razmatrano, već su performanse testirane sa datim prototipom uz komentar da će njihovo poboljšanje definitivno biti moguće u daljoj realizacjii projekta.

IV. TEST U URBANOJ SREDINI

Iako su IoT uređaji koji sadrže LoRa module obično deklarisani kao uređaji dugog dometa, u urbanim sredinama ovakvu tvrdnju treba prihvatiti sa izvesnom rezervom. Pri prostiranju u urbanoj sredini, radio signal podleže različitim propagacionim efektima od kojih su dominantni [8], [9]:

- efekat fedinga, i
- efekat senke

Feding nastaje kao posledica interfenecije više talasa koji se prostiru različitim mogućim putanjama između predajnika i prijemnika. Obzirom da u urbanim sredinama postoji veći broj ravnih/neravnih površina koje mogu biti reflektivne ili predstavljati centre rasejanja radio talasa, na mestu prijema će doći do suštinskog kombinovanja velikog broja komponenti signala, koje imaju različite amplitude i faze. Kombinovanje može biti konstuktivno ili destruktivno, zavisno od konkretne raspodele faza i kašnjenja signala [8]. U vezi sa različitim raspodelama komponenti signala, mogu se formulisati različiti modeli fedinga koji na statistički način tretiraju ove propagacione efekte [10].

U testu koji se odnosi na urbanu sredinu, odlučili smo da predajnik i prijemnik udaljimo do te mere da signali na prijemu budu iznad nivoa šuma, kako bismo mogli da ih detektujemo sa relativno velikom verovatnoćom, odnosno tako da verovatnoća otkaza prenosa bude niska. Ovakvu situaciju smo postigli postavljanjem predajnika u laboratoriju 304 na Elektronskom fakultetu, dok je prijemnik bio smešten u suprotnom delu zgrade, u prostorije M2M laboratorije koja je trenutno u procesu osnivanja. Šematski prikaz pozicija predajnika i prijemnika, kao i fotografija iz vazduha na kojoj su označene ove pozicije, predstavljene su na slici 4.

Udaljenost predajnika i prijemnika je oko 70 m, pri čemu je ukupno slabljenje na ovoj deonici oko 140 dBm. Obzirom da se slabljenje u slobodnom prostoru može proceniti na 68 dB pod pretpostavkom izotropne antene, ostatak slabljenja se mora pripisati slabljenju na zidovima na putu prostiranja, što iznosi oko 72 dB. Sa slike 4.a se vidi da se na putu prostiranja nalazi 5 horizontalnih zidova i jedna podna površina, pa se može proceniti da je slabljenje na individualnom betonskom zidu/podu oko 12 dB.

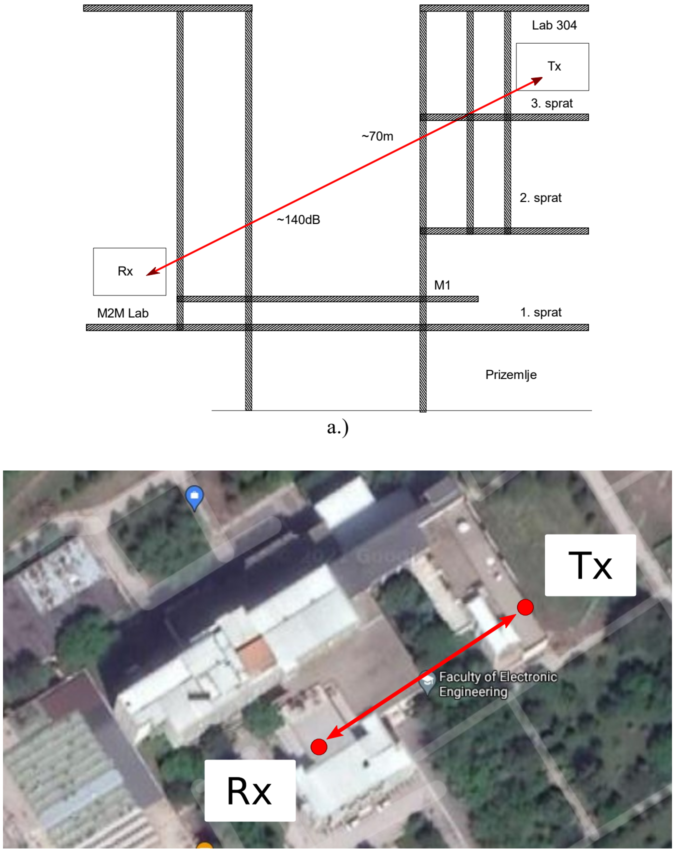

a.)

b.)

Sl. 4. Šematski prikaz lokacija predajnika i prijemnika unutar zgrade Elektronskog fakulteta prilikom procene propagacionih efekata za slučaj urbane sredine.

Konkretna realizacija efekta fedinga je proučena za ovaj slučaj korišćenjem mehanizma za precizno pozicioniranje predajnika u laboratoriji 304. Prilikom pomeranja predajnika duž linijske putanje sa korakom od 1 mm, na prijemu je svaki put zabeležen nivo primljenog signala. Procena primljenog nivoa se oslanja na informaciju dobijenu od samog prijemnika, a ova informacija se beleži u obliku indikatora jačine primljenog signala (RSSI), koji približno odgovara primljenoj snazi u jedinicama dBm. Na slici 5. je prikazan skup prikupljenih podataka dobijenih skeniranem putanje predajnika u dužini od 2.1 m, koji sadrži ukupno 2100 tačaka. Potrebno je pomenuti da ispod indikatora -129 nije primljen ni jedan paket, odnosno svi primljeni paketi su iznad ovog nivoa.

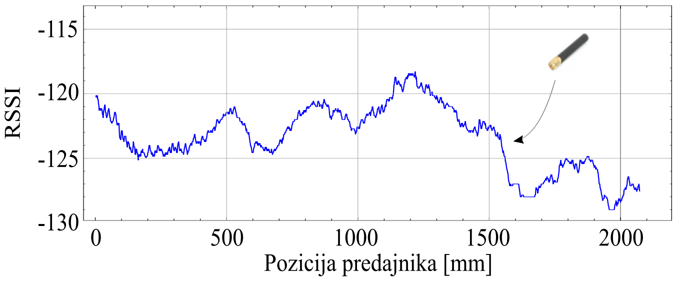

Sl. 5. Indikator jačine signala na prijemu u zavisnosti od precizne pozicije predajnika, za slučaj prostiranja u urbanoj sredini.

Ovde treba navesti da su parametri komunikacije podešeni na sledeći način: propusni opseg – 62,5 kHz, faktor proširenja spektra – 10, kodni faktor – 4/5, što odgovara bitskoj brzini od 488 b/s. Naravno, niska bitska brzina odgovara IoT namenama koje prenose malu količinu podataka, zauzimajući zadati kanal u toku veoma kratkog vremenskog intervala i sa relativno velikom pauzom između sukcesivnih transmisija.

Svakako, treba imati u vidu i prirodu modulacije sa proširenim spektrom, koja obezbeđuje izvesni nivo imunosti na efekat fedinga u odnosu na uskopojasne signale. Obzirom da je ukupna varijacija signala usled efekta fedinga iznosila oko +/-5 dB, očigledno je da u urbanim uslovima, kada ne postoji linija direktne optičke vidljivosti između predajnika i prijemnika, osnovni problem sistema predstavlja efekat senke oličen u slabljenju na fizičkim preprekama.

V. TEST NA OTVORENOM PROSTORU

Kada se razmatraju performanse IoT sistema zasnovanog na LoRa primopredajnicima u ruralnim uslovima, treba uočiti da su tada propagacioni efekti značajno različiti od uslova u urbanim sredinama. Snaga signala na prijemu se usled prostiranja u slobodnom prostoru može proceniti shodno ilustraciji na slici 6. i poznatim parametrima koji se odnose na izotropnu antenu, kao [6]:

$$[P_{Rx}]_{dB} = [P_{Tx}]_{dB} + 2\left(10\log_{10}\frac{c}{4\pi f_0} - 10\log_{10} r\right) \qquad (1)$$

Analizom ove jednačine može se utvrditi da slabljenje koje odgovara nivou osetljivosti prijemnika zahteva ekstremno velike udaljenosti. Ova činjenica ima i praktičnu potvrdu u merenjima koja su pokazala da je u povoljnim uslovima pri kojima postoji linija optičke vidljivosti, prijem LoRa signala moguć i na udaljenostima većim od 700 km. U pomenutom slučaju je optička vidljivost obezbeđena time što je predajnik podignut na visinu od 38 km uz pomoć meteorološkog balona.

Jedna od osnovnih pretpostavki je da u ruralnim uslovima može postojati optička vidljivost između predajnika i prijemnika. Ipak, ovu pretpostavku treba uzeti sa rezervom jer je upadljivo zavisna od konfiguracije terena. Čak i kada pretpostavimo da na površini Zemlje ne postoje uzvišenja i udubljenja, odnosno kada Zemljinu površinu posmatramo kao savršenu sferu, jednostavnim geometrijskim razmatranjem možemo doći do formule koja opisuje maksimalnu daljinu optičke vidljivosti u zavisnosti od visine na kojoj je postavljena antena. Ova formula se može aproksimirati izrazom:

$$d_{[km]} \approx 3.57\sqrt{h_{[m]}}\,, \qquad (2)$$

u kome je domet *d* izražen u kilometrima, a visina na kojoj je postavljena predajna antena - *h*, u metrima. U tabeli I je prikazana udaljenost horizonta za različite visine postavljanja antene.

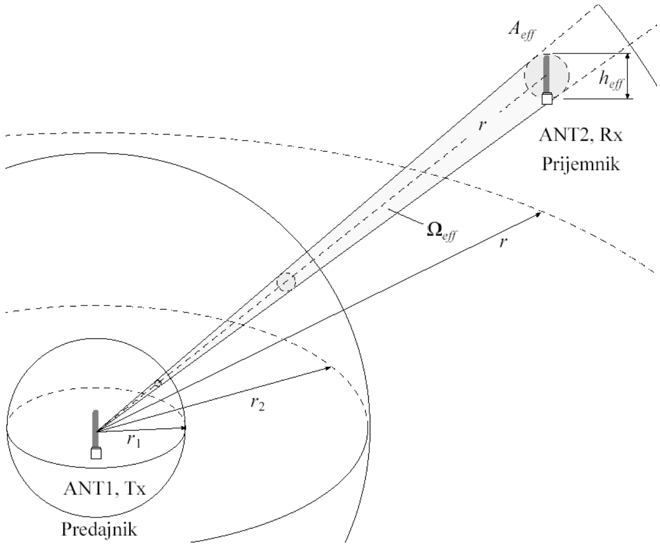

Sl. 6. Ilustracija slabljenja u slobodnom prostoru.

TABELA I
TEORIJSKI RADIO-HORIZONT KADA JE ANTENA POSTAVLJENA NA RAZLIČITIM VISINAMA IZNAD POVRŠINE ZEMLJE

Pozicija antene iznad nivoa zemlje [cm]	Domet [km]
10	1.13
30	1.95
60	2.77
100	3.57
200	5.05

U konkretnom eksperimentu koji smo izveli na otvorenom prostoru, pouzdana i uspešna veza je ostvarena između predajnika na brdu Čegar i prijemnika na lokaciji iznad Niške Banje, na rastojanju od oko 10 km, uz uslov da između njih postoji optička vidljivost (Slika 7). RSSI vrednost je tom prilikom iznosila oko -125.

Sl. 7. Deonica uspešnog prenosa na daljini većoj od 10 km kada postoji optička vidljivost.

VI. ZAKLJUČAK

U radu su predstavljeni rezultati eksperimentalne procene dometa LoRa primopredajnika za IoT u urbanom i ruralnom okruženju. Dobijeni rezultati za urbanu sredinu pokazuju da je efekat senke dominantan uticaj u ukupnom slabljenju signala kada ne postoji optička vidljivost između predajnika i prijemnika, dok je uticaj fedinga tada znatno manji. U zatvorenom prostoru se usled ovoga veoma brzo smanjuje nivo signala sa povećanjem udaljenosti i broja prepreka, pa se može očekivati da će domet biti za nekoliko redova veličine manji od specifikacija za otvoreni prostor. Zbog toga je u zatvorenom prostoru pogodnije koristiti neke od tehnologija kratkog dometa, pri čemu treba obezbediti da predajnik i prijemnik budu fizički u međusobnoj poziciji kojom je omogućen uspešan prenos. Sa druge strane, u otvorenom prostoru se dobri rezultati u pogledu dometa mogu očekivati kada između predajnika i prijemnika postoji linija direktne optičke vidljivosti. U ovakvim slučajevima domet može biti i veći od 10 km, što je eksperimentalno potvrđeno na terenu. U slučaju da ne postoji optička vidljivost, ili da na liniji optičke vidljivosti postoje prepreke, domet će biti znatno manji, zavisno od specifičnosti određene situacije.

ZAHVALNICA

Projekat CANANDI finansira Fond za inovacionu delatnost iz budžeta Republike Srbije sa razdela Ministarstva prosvete, nauke i tehnološkog razvoja, a kroz Projekat za unapređenje konkurentnosti i zapošljavanja (sporazum o zajmu sa Svetskom bankom).

LITERATURA

[1] L. Farhan, R. Kharel “Internet of Things: Vision, Future Directions and Opportunities,” In: Mukhopadhyay S., Jayasundera K., Postolache O. (eds) *Modern Sensing Technologies. Smart Sensors, Measurement and Instrumentation*, vol 29. Springer, Cham., 2019.

[2] E. Sisinni, A. Saifullah, S. Han, U. Jennehag and M. Gidlund, “Industrial Internet of Things: Challenges, Opportunities, and Directions,” *IEEE Trans. Ind. Informat.*, vol. 14, no. 11, pp. 4724-4734, Nov. 2018.

[3] M. Sauter, *From GSM to LTE-Advanced Pro and 5G: An Introduction to Mobile Networks and Mobile Broadband*; Wiley: Hoboken, NJ, USA, 2017.

[4] A. Augustin, J. Yi, T.Clausen, W.M. Townsley, “A study of LoRa: Long range & Low Power Networks for the Internet of Things,” *Sensors,* 16, 1466., 2016.

[5] I. Ahmed, S. Orfali, T. Khattab and A. Mohamed, “Characterization of the indoor-outdoor radio propagation channel at 2.4 GHz,” *2011 IEEE GCC Conference and Exhibition (GCC)*, pp. 605-608, 2011.

[6] E. N. Sharma and G. C. Lall, “Enhancement and Character-ization of Indoor Propagation Models,” *International Journal of Scientific & Engineering Research*, vol. 2, no. 11, pp. 1–7, Nov. 2011.

[7] E. Suikkanen, A. Tölli and M. Latva-aho, “Characterization of propagation in an outdoor-to-indoor scenario at 780 MHz,” 21st *Annual IEEE International Symposium on Personal, Indoor and Mobile Radio Communications*, pp. 70-74., 2010.

[8] P. M. Shankar, *Fading and Shadowing in Wireless Systems*, NewYork, NY, USA: Springer Science Business Media, 2012.

[9] B. Liu, B.P. Otis, S. Challa, P. Axon, C. Chou and S.K. Jha “The impact of fading and shadowing on the network performance of wireless sensor networks,” *International Journal of Sensor Networks*, vol. 3, no. 4 pp. 211-223, 2008.

[10] S. Popa, N. Draghiciu and R. Reiz: “Fading Types in Wireless Communications Systems”, *Journal of Electrical and Electronics Engineering*, vol. 1, pp. 232-237, 2008.

ABSTRACT

In this paper we report practical results of signal level measurements during data transmission using a LoRa-based platform. Although the target applications for these platforms are primarily Internet of Things in urban environments, the paper also considers their use in rural surrounding. One of the ideas for an application is monitoring animals in environments that are located outside inhabited areas. Range of radio links in these environments can be significantly larger than in urban environments, depending on conditions of optical line-of-sight and obstacles located between the transmitter and the receiver. Practical results indicate that under favorable conditions acceptable transmission results can be achieved even at ranges beyond 10 km.

Range evaluation of LoRa IoT transceivers in urban and rural environment

Dejan N. Milić, Slavimir Stošović, Dejan Stevanović,
Jelena Anastasov

On the impact of network load on CQI reporting and Link Adaptation in LTE systems

Igor A. Tomić, Milutin S. Davidović, Dejan D. Drajić, and Predrag Ivaniš

Abstract—**Data payload in mobile networks is persistently increasing, which puts a lot of pressure to Mobile Operators to seek for solutions that will deliver cheaper bit per second. Network performance modelling is important discipline in process of technology strategy definition, evaluation of different solutions/scenarios and finally design and planning of Long Term Evolution (LTE) systems. One of the key prerequisites for successful performance modelling process and prediction of user experience with growing network load is to understand impact of traffic increase on link adaptation. In this paper correlation between network load, measured as *Physical Resource Block* (PRB) utilization, and Link adaptation, measured with reported *Channel Quality Indicator* (CQI) is analyzed. Analysis is done based on performance measurements from mature commercial LTE network with several frequency layers deployed. Impact of network load increase on link adaptation performance was assessed. Performance of different frequency bands were observed separately, analysis was conducted for low band (bellow 1 GHz) and mid band (in range between 1 GHz and 6 GHz). Furthermore, analysis was segmented for different topologies in terms of network density – from urban to rural. Finally, impact of user mobility and spatial distribution of terminals, variations during working days and weekends were investigated.**

Index Terms—**LTE, Performance modelling, CQI, Network load, PRB utilization, Link adaptation, Spectral efficiency.**

I. INTRODUCTION

IN the last few years mobile operators were facing increase of data payload and growing network load as a major challenge in a mission to secure required user experience, that is mainly defined and measured as target downlink throughput or latency [1]. Fourth and fifth generation (4G and 5G) of mobile communication systems are based on *Orthogonal Frequency Division Multiple Access* (OFDMA) technique which enables flexible radio resource allocation [2], [3]. The most common answer from mobile operators has been the investment in spectrum expansions and deployment of additional frequency layers in carrier aggregation scenario.

However, as spectrum assets are limited and scarce resources, price per Hz was increasing even dramatically on spectral auctions over last ten years, mainly due to growing demand which is lately present on all meridians around the globe [4]. In such circumstances, spectral efficiency is important more than ever [5], [6] and mobile operators are looking for spectral efficiency improvements to the largest possible extent.

The main driver for spectral efficiency is link adaptation, and its performance in OFDMA based systems is mainly driven by interference which is reflected in reported CQI based on *User Equipment* (UE) channel quality estimation and related measurements. With growing traffic, mainly for data services, but also speech and IoT [6], and higher network utilization observed, increase of intra-system interference is logically expected.

This paper investigates impact of growing network load on CQI reporting. In chapter II, theoretical considerations will be elaborated, while in chapter III impact of network load and correlation with CQI degradation will be investigated. Chapter IV will further analyze correlations for different network density, followed by deep dive to network performance signatures during working days and weekends in chapter V. Finally, paper will be concluded with overview of findings, proposal for future work and list of references.

II. THEORETICAL BACKGROUND

Link adaptation is the ability of radio communication systems to adapt the modulation scheme and the coding rate of the error correction according to the conditions that user expects and quality of the radio link. Algorithm will secure that a high-level efficient modulation scheme and a small amount of error correction is used when conditions of the radio link are good. Link adaptation happens in a downlink scheduler located in base station, which needs to know radio channel for each UE. The estimation of radio channel state and selection of optimal transmission scheme may be achieved through closed loop measurements, presented at Fig. 1, performed by UE on channels transmitted by base stations (*Cell reference Signal* – CRS in LTE) or reciprocity based on measurements conducted by base stations on signal transmitted by UE (*Sounding Reference Signal* – SRS), which is mainly applicable for Time Division Duplex (TDD) systems with good uplink-downlink channel reciprocity. In Frequency Division Duplex (FDD) systems closed loop channel estimation is used, where 3GPP standard requests each UE to perform *Channel State Information* (CSI) reporting that carries necessary information on a radio signal [8].

CSI reporting may be periodic and aperiodic. Periodic reporting is carried either by *Physical Uplink Control Channel* (PUCCH) or *Physical Uplink Shared Channel*

Igor A. Tomić, University of Belgrade-School of Electrical Engineering, Bulevar kralja Aleksandra 73, 11000 Belgrade and Aspire Technology Unlimited – Belgrade Branch Office, Vladimira Popovića 6, Unit B10, 11070 Belgrade, Serbia (e-mail: igor.tomic@aspiretechnology.com).

Milutin S. Davidović, University of Belgrade-School of Electrical Engineering, Bulevar kralja Aleksandra 73, 11000 Belgrade and Aspire Technology Unlimited – Belgrade Branch Office, Vladimira Popovića 6, Unit B10, 11070 Belgrade, Serbia (e-mail: milutin.davidovic@aspiretechnology.com).

Dejan D. Drajić, University of Belgrade- School of Electrical Engineering, Bulevar kralja Aleksandra 73, 11000 Belgrade, Serbia (e-mail: ddrajic@etf.bg.ac.rs).

Predrag N. Ivaniš, University of Belgrade - School of Electrical Engineering,, Bulevar kralja Aleksandra 73, 11000 Belgrade, Serbia (e-mail: predrag.ivanis@etf.bg.ac.rs).

(PUSCH) when user data on *Dedicated Control Channel* (DCCH) and *Dedicated Traffic Channel* (DTCH) needs to be transmitted at the same time with L1/L2 control signaling. Periodicity is configured by a higher *Radio Resource Control* (RRC) layer. Aperiodic reporting is used mostly for *Random Access Channel* (RACH) procedure, where handovers or losses of synchronization are common reasons. Aperiodic reporting also happens when eNodeB schedules specific *Physical Downlink Control Channel* (PDCCH) *Downlink Control Indicator* (DCI) format 0 together with CQI request field set to 1, demanding uplink grant for UE data together with an aperiodic CQI report.

CSI consists of three major components: *Channel Quality Indicator* (CQI), *Precoding Matrix Index* (PMI) and *Rank Indicator* (RI). The focus of this paper is behavior of CQI, which implicitly indicates a suitable link adaptation and downlink transmission data rate, i.e. the highest *Modulation and Coding Scheme* (MCS) value at which the UE will be able to properly demodulate and decode the downlink data at target *Block Error Rate* (BLER) of 10%.

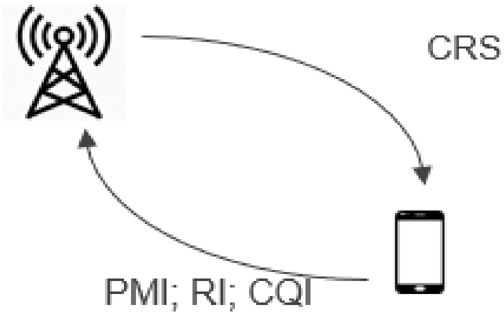

Fig. 1. Channel estimation based on Closed loop measurements, typical for LTE FDD systems

TABLE I
4-BIT CQI TABLE UP TO 64QAM MODULATION

CQI Index	Modulation	Code rate ×1024	efficiency
0	*Out of order*		
1	QPSK	78	0.1523
2	QPSK	120	0.2344
3	QPSK	193	0.3770
4	QPSK	308	0.6016
5	QPSK	449	0.8770
6	QPSK	602	1.1758
7	16QAM	378	1.4766
8	16QAM	490	1.9141
9	16QAM	616	2.4063
10	64QAM	466	2.7305
11	64QAM	567	3.3223
12	64QAM	666	3.9023
13	64QAM	772	4.5234
14	64QAM	873	5.1152
15	64QAM	948	5.5547

CQI calculation is not precisely defined by 3GPP standard and UE or chipset manufacturers have freedom to design algorithm and do implementation that will maximize accuracy and performance of link adaptation. However, calculations are typically based on measurements of *Signal-to-Interference plus Noise Ratio* (SINR), which are mapped to 16 discrete CQI values between 0 and 15, where index 15 indicates the best channel quality and index 1 indicates the poorest channel quality. Expected link adaptation - the mapping between CQI and modulation scheme and transport block size is defined by 3GPP [8], with two mapping tables defined for different UE capability. Table 1 is used for UEs supporting modulation up to 64QAM, while Table 2 is used for UEs supporting modulation up to 256QAM.

TABLE 2
4-BIT CQI TABLE UP TO 256QAM MODULATION

CQI Index	Modulation	Code rate ×1024	efficiency
0	*Out of order*		
1	QPSK	78	0.1523
2	QPSK	193	0.3770
3	QPSK	449	0.8770
4	16QAM	378	1.4766
5	16QAM	490	1.9141
6	16QAM	616	2.4063
7	64QAM	466	2.7305
8	64QAM	567	3.3223
9	64QAM	666	3.9023
10	64QAM	772	4.5234
11	64QAM	873	5.1152
12	256QAM	711	5.5547
13	256QAM	797	6.2266
14	256QAM	885	6.9141
15	256QAM	948	7.4063

CQI indicator is one of the main drivers for performance of LTE system, as it will determine link adaptation in terms of selected modulation, transmitted bits per symbol, coding and efficiency. Furthermore, there is a strong correlation observed between CQI and probability to have Rank higher than 1 and use more layers in *Multiple Input Multiple Output* (MIMO) system, which is often referred to as MIMO utilization [1]. Hence, lower CQI reported will cause additional negative impact on spectral efficiency, through worse spatial multiplexing performance.

III. CQI REPORTING AND NETWORK LOAD

Performance management data, including relevant counters and performance indicators, have been collected from commercial network that operates in two frequency bands: Band 12 - 700 MHz (operating DL frequency: 729 – 746 MHz) and Band 2 – PCS 1900 MHz (operating DL frequency: 1930–1990 MHz). Analysis is focused on average reported CQI and network load measured as average PRB utilization. Data was collected for period of ten days with cell resolution, where aggregation and averaging were performed afterwards on hourly level.

Fig. 2 presents correlation between average reported CQI and PRB utilization for two operating frequency bands, where first observation is a very good level of correlation between average CQI and network load, for both frequency bands, with correlation coefficient of 0.8173 for Band 2 and 0.9357 for Band 12. Network load is not evenly distributed, where for Band 12, average PRB utilization spans up to 45% during busy hour, while maximum measured PRB utilization for Band 2 is 20%.

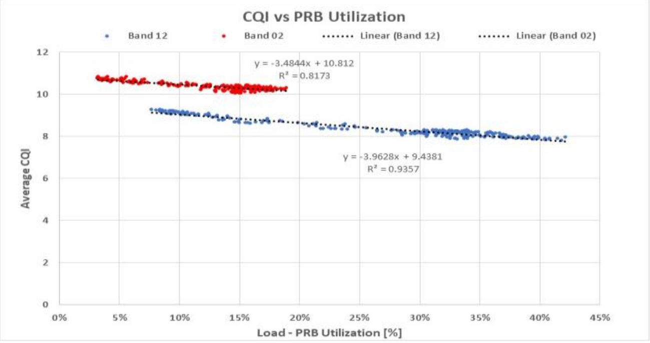

Fig. 2. Average reported CQI vs PRB utilization, LTE Bands 2 and 12

.

Some final remarks are that average CQI for same level of network load is higher on Band 2. This can be explained with lower operating frequency of Band 12(700 MHz vs 1900 MHz), which means that radio waves have better propagation in Band 12 and system is more sensitive on inter-cell interference. The difference between two curves in average reported CQI for same level of network load is quite significant – approximately 1.5.

From observation discussed in this chapter, it can be concluded that CQI reporting process in LTE network is driven mainly by inter-cell interference, with strong correlation with network load, and greater sensitivity for lower frequency bands.

IV. CQI REPORTING AND NETWORK DENSITY

Logical next step in analysis is to evaluate impact of network density in terms of number of deployed base stations and average Inter-Site Distance (ISD).

Network topology was analyzed with deep dive to geographical position of base stations, where sites were segmented to high and low network density area with following criteria:

- High network density area: if criteria more than three neighboring sites within radius of 1.2 km is met
- Low network density area: if criteria less than two neighboring sites within radius of 1.2 km is met

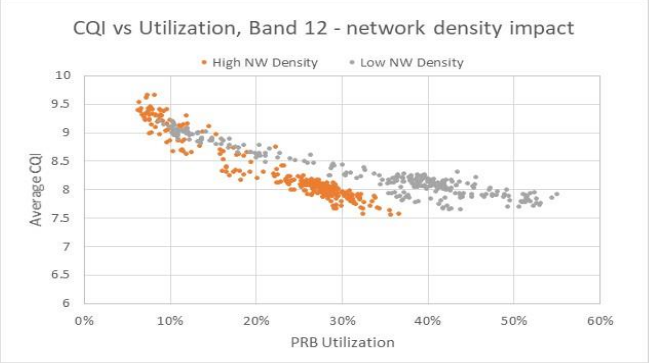

Fig. 3. CQI vs PRB Utilization, Network density impact, Band 12

Fig. 3 presents correlation between average CQI and PRB utilization, for two group of sites – belonging to high and low network density area, with operating frequency in Band 12. Similar analysis is done for Band 2, and results are presented on Fig. 4.

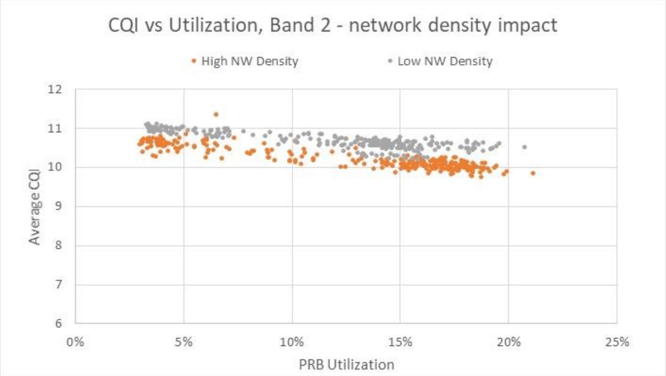

Fig. 4. CQI vs PRB Utilization, Network density impact, Band 2

The first observation is that base stations in high density areas are more affected with growing load, and lower reported CQI may be expected for same level of PRB utilization. Also, it is interesting to notice that impact of network density on correlation of interest is different for two observed frequency bands. While for Band 2 (Fig. 4) two curves are parallel, only shifted by approximately 0.5, in case of Band 12 (Fig. 3) steeper curve and higher relative drop may be expected in high density areas. For PRB utilization increase from 10% to 30%, in high density area average CQI reported value will drop from 9 to 8, while in low density area drop will be less severe, from 9 to 8.5.

V. CQI REPORTING AND USER DISTRIBUTION

After network load impact analysis, operating frequency band and network density on CQI reporting, another interesting aspect to consider is behavior of users in terms of their mobility and spatial distribution. One way to assess impact of mobility is to segment data for workdays – Monday to Friday, and weekends – Saturday to Sunday, as mobility patterns are clearly different.

As already noted in the Chapter I, good correlation is present in both Band 12 and Band 2 and it remained similar after the segmentation of the data sample to workdays and weekends.

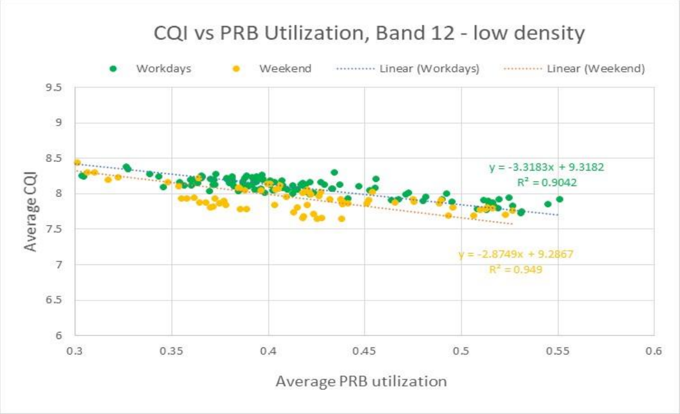

Fig. 5. CQI vs PRB Utilization, User Distribution Impact, Low density area, Band 12

However, there is a trend of having slightly lower CQI as well as the bigger deviation of reported CQI during the weekend.

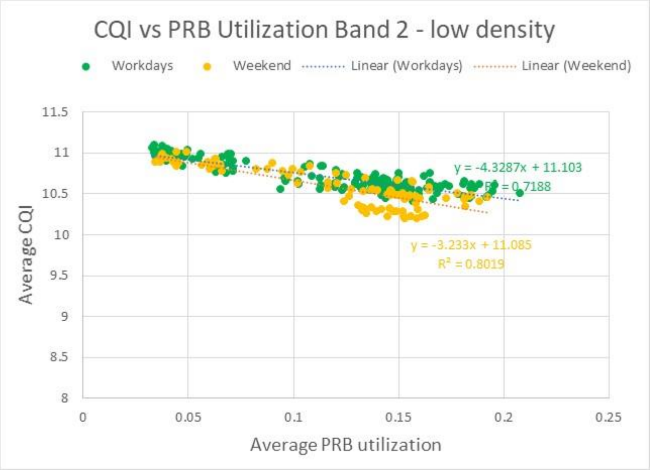

Fig. 6. CQI vs PRB Utilization, User Distribution Impact, Low density area, Band 2

This phenomenon is more noticeable in the low-density areas, especially in the range of higher PRB utilization in the observed sample (Fig. 5 and Fig. 6). The drop of 0.1-0.2 in average reported CQI during the weekend could be observed. In this case, another interesting phenomenon of having larger spam/deviation or even two trends of reported CQI for the same load circumstances could be observed. This could be due to different activity patterns of the users in some hours during the weekend in these areas, but further investigation (i.e. machine learning based) need to be conducted to drive some more specific conclusions.

On the other hand, looking at the high-density areas (Fig. 7 and Fig. 8), the impact of the day of the week on the CQI vs PRB utilization correlation is neglectable, most probably due to the reason that there is not much difference in user mobility and spatial distribution patterns in more dense areas of the network.

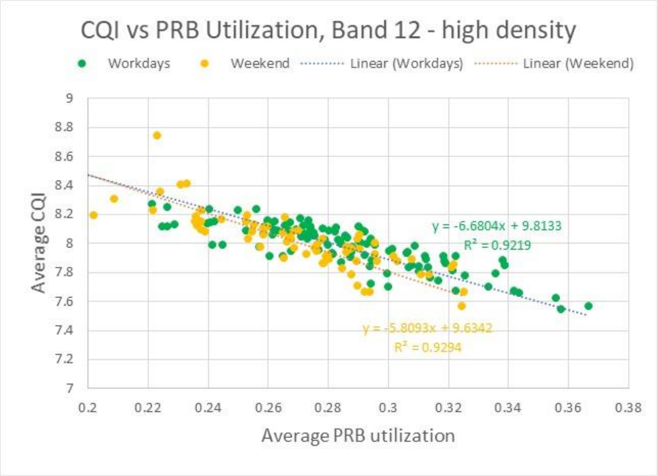

Fig. 7. CQI vs PRB Utilization, User Distribution Impact, High density area, Band 12

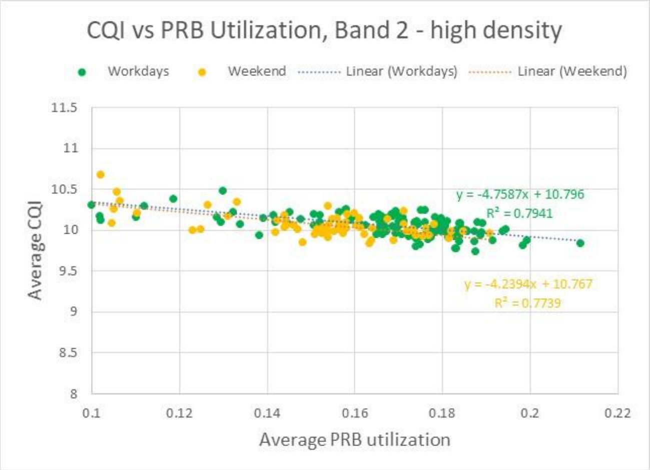

Fig. 8. CQI vs PRB Utilization, User Distribution Impact, High density area, Band 2

VI. CONCLUSION

Link adaptation is one of the main drivers for performance of OFDMA based mobile communication systems, such as LTE and NR. In this paper, the impact of network load on CQI reporting was analyzed and strong level of correlation was observed. Greater sensitivity for lower frequency bands was proven, which was in line with expectations, having in mind better propagation at lower frequencies causing more inter-cell interference. Furthermore, the areas with higher network density showed to be more affected with growing load and CQI degradation drop with steeper trend. Finally, impact of user mobility and traffic distribution is also evident, where different patterns were recognized during workdays and weekends.

Future work concerns deeper analysis of particular patterns through implementation of artificial intelligence and machine learning (AI/ML) techniques, and further correlation with spatial multiplexing performance in MIMO.

REFERENCES

[1] I.Tomić, Đ.Lukić, M. Davidović, D. Drajić, and P. Ivaniš, “Statistical analysis of CQI reporting and MIMO utilization for downlink scheduling in live LTE mobile network”, *Telfor Journal 2020,* vol. 12, iss. 1, pp. 8-12

[2] C. Cox, *An Introduction to LTE, 2nd edition*, John Wiley & The Sons Ltd, Chichester 2014.

[3] N. Gospić, I. Tomić, D. Popović and D. Bogojević, *“Razvoj mobilnih telekomunikacija, od GSM do LTE,”* Univerzitet u Beogradu, Saobraćajni fakultet, Beograd 2010.

[4] Spectrum Navigator, Q1 2021 New insights and trends to watch, GSMA, May 2021, https://www.gsma.com/spectrum/wp-content/uploads/2021/03/Spectrum-Navigator-Q1-2021.pdf

[5] M.Davidović, S.Bjekovic and I.Tomic, “On the impact of network load on LTE network downlink performance”, *IcETRAN conference 2015*, Srebrno Jezero 2015.

[6] I.A.Tomić, M.S.Davidović and S.M.Bjeković, “On the downlink capacity of LTE cell,” *23rd Telecommunications Forum TELFOR 2015*, pp. 181-185, Belgrade 2015.

[7] M. Davidović, I. Tomić, D. Drajić, and Z. Čiča, “On the Impact of NB-IoT on LTE MBB Downlink Performance,” *TELFOR Journal*, Vol.11, No.1, pp. 20-24, Belgrade 2019.

[8] “*Evolved Universal Terrestrial Radio Access (E-UTRA); Physical Layer Procedures,” 3GPP TS 36.213 15.7.0*, September 2019.

Design Problems in Implementation and Control of Malicious Drone Missions Jammers

Jovan Radivojević, Aleksandar Vujić, Mladen Mileusnić, Predrag Petrović, Aleksandar Lebl

Abstract— **Three important problems related to the malicious drone missions jamming are analyzed in this paper. These problems are: 1) selection of drone signals which are going to be jammed and corresponding signal frequencies, 2) selection of optimum jamming strategies and definition of signal characteristics, and 3) design of reliable and user friendly system control mechanisms. The implemented solution allows jamming of a significant number of signals important for drone operation: video, telemetry and navigation signals. Classic sweeping is modified to multisweep jamming with continuous and discrete sub-bands to increase jamming efficiency. Device control is possible from the PC application software by the application of user friendly menus or from a specially designed module for remote control. The implemented jamming system is presented as well as the characteristics of the generated jamming signals.**

Index Terms**—Malicious drone missions jamming; jamming scenario; remote control; user interface.**

I. INTRODUCTION

DRONES or unmanned aerial vehicle (UAV) are every day becoming more often implemented devices in replacing humans in dangerous and time wasting missions. As they come to the place of accident by air flight, sometimes they may save people and material resources just because they are faster than other technologies. But, drones are also used in various malicious missions. They may carry explosive to cause numerous victims and damages of many important objects and places such as airports, stadiums, residential areas, governmental facilities, commercial and industrial facilities, and so on. They may be applied for spy missions, smuggling illicit materials over borders or into and out of the prisons [1], [2]. Well prepared drone mission at one place may cause enormous economy loss and problems for the whole world [3] when just one concentrated attack disabled for a pretty long time 5% of world crude oil production. When considering data from Civil Aviation Directorate of the Republic of Serbia [4], more than 95% of drones in Serbia in 2017. were used illegally. All these illegal drones may be the reason of intentionally or unintentionally caused problem. Only these last two data from national and international literature and the short survey of places suitable for drone illegal activities are sufficient to approve the importance of drone effective jamming when their flight is not regularly registered.

II. THE PROBLEMS TO BE SOLVED

The problems which have to be solved to prevent illicit drone mission may be divided to three groups: 1) what drone signals have to be jammed; 2) what jamming strategies and jamming signal levels are the most effective for successful drone disabling; 3) what control scenario should be implemented to allow easy and reliable user handling the drone jammer.

There is a variety of drones available on the world market. All of them in principle operate using three main signal types: 1) communication signals interchange between the drone and its operator; 2) video and telemetry signals transmission to the operator; 3) satellite navigation signals reception (GPS or GLONASS). The frequencies for the third signal type are standardized, but the frequencies for the first two signal groups depend on the applied drone model. The more detailed analysis has shown that frequencies used for video and telemetry links at the greatest majority of drone types are 433 MHz, 868 MHz, 915 MHz, 1.2 GHz, 2.4 GHz and 5.8 GHz [2], [5] - [7]. The standardized frequencies for GPS and GLONASS systems are 1176 MHz, 1227 MHz and 1.57-1.62 GHz. It is hard to find that any drone jammer may effectively disrupt transmission of signals at each of the emphasized frequencies. Nearly all these frequencies are jammed in [6]; in other cases the dominant goal is to jam frequencies of navigation systems [7] or navigation system plus links on 2.4 GHz and 5.8 GHz [8]. The objective of the presented solution is to realize jamming of all emphasized frequencies for video and telemetry signals transmission in modern solutions and the frequencies for navigation. Such solution has the maximum flexibility and the highest possibilities.

Various jamming strategies are defined and developed for remote control improvised explosive devices (RCIED) activation jamming and also for radio and mobile systems surveillance and jamming. Two basic groups of jamming strategies are active and reactive jamming. The first of them supposes that jamming signal is continually generated. In the second case jamming signal is generated only when drone presence is detected. When considering signal characteristics, sweep and barrage jamming are most widely used as well as their variants and combinations. IRITEL has the great experience in both jamming development and implementation and theoretical analysis for all mentioned applications and

Jovan Radivojević is with the Institute IRITEL, Batajnički put 23, 11080 Belgrade, Serbia (e-mail: jovan.radivojevic@iritel.com).

Aleksandar Vujić is with the Institute IRITEL, Batajnički put 23, 11080 Belgrade, Serbia (e-mail: aleksandar.vujic@iritel.com).

Mladen Mileusnić is with the Institute IRITEL, Batajnički put 23, 11080 Belgrade, Serbia (e-mail: mladenmi@iritel.com).

Predrag Petrović is with the Institute IRITEL, Batajnički put 23, 11080 Belgrade, Serbia (e-mail: presa@iritel.com).

Aleksandar Lebl is with the Institute IRITEL, Batajnički put 23, 11080 Belgrade, Serbia (e-mail: lebl@iritel.com).

signal generation strategies. References [9] - [18] represent the small part of IRITEL previous solutions relating to the topic of this paper. The goal of our analysis is to select a set of optimum jamming strategies and signal characteristics for effective jamming.

In the field of jammer control, the aim is to provide flexibility of operator handling. It means that the scenario of the first choice is to allow the parameters of the jamming signal to be easily and instantaneously changeable according to operator plans. In the more rigid situations only a set of jamming signal characteristics is defined and operator should make a decision between a priori specified options. This is the second device control procedure. The additional objective which results from these two scenarios is that reliability of control function practical implementation is significantly improved.

III. DESIGN CONSIDERATIONS

The frequencies which are jammed cover a wide frequency range 433-5800 MHz. It is important to notice that in the range 1620-2400 MHz there are no important frequencies to be jammed. Sweep and barrage jamming as two dominant jamming strategies have specific problems when jamming is applied to the wide bandwidth. When considering sweep jamming, the problem is to achieve very high sweep rate to reliably disrupt very short messages [13], [14]. In the case of pure barrage jamming implementation, the problem is necessity to have too high emission power which is split to the whole applied frequency band even where this is not necessary [15]. These two limiting factors are the reason to split the whole bandwidth into several sub-bands using separate jammer modules which may operate in parallel. We have decided to have five independent modules. Among these modules, the third module in the range 1164-1620 MHz covers the greatest number of frequencies of interest: all frequencies for navigation and one frequency for video and telemetry link. Only this module is sufficient to achieve performances comparable to the majority drone jammer solutions in the world.

Frequencies of the signals which have to be jammed are a priori mainly known. In such a case efficiency of sweep jamming may be improved. For example, it is not necessary to generate sweep signal in the whole third band 1164-1610 MHz, but only in some its parts where the frequencies of interest are located. It is possible to implement two sweep jamming strategies which decrease necessary sweep rate: 1) multisweep with continuous sub-bands (continuously sweeping over some parts of the total frequency band) and 2) multisweep with discrete sub-bands (sweeping only over discrete frequencies within frequency sub-bands). The second of these two variants is innovative in IRITEL jamming systems and not implemented in other solutions according to the authors' knowledge.

Flexibility of operator's jammer handling is achieved both by hardware and software methods. Hardware solutions allow variable gain adjust, precise jamming signal frequencies definition, more discrete frequencies selection for jamming, several (four) different jamming strategies implementation, precise definition of jamming and non-jamming time intervals and selection of one jamming scenario between several (eight) predefined programmed procedures when system is controlled by special developed remote controller. Dealing with software, user interface is intuitive, easily understandable and clear when control is devoted to a PC to support all wide hardware possibilities.

IV. THE JAMMER IMPLEMENTATION

IRITEL previous jammer solutions related to drones are presented in [19], [20]. In [19] it is explained how drones are used in friendly missions to improve RCIED activation jamming efficiency: if drone is carrying jamming device, the jamming signal may reach larger distance in comparison to the ground jamming. On the other hand, the main principles of malicious drone jamming system and the frequency spectrum of all implemented jamming strategies are presented in [20].

The block-scheme of the realized jamming system is now presented in the Fig. 1. The system includes the jamming device and separate module for remote control as also the application software for control and management at the distant PC computer.

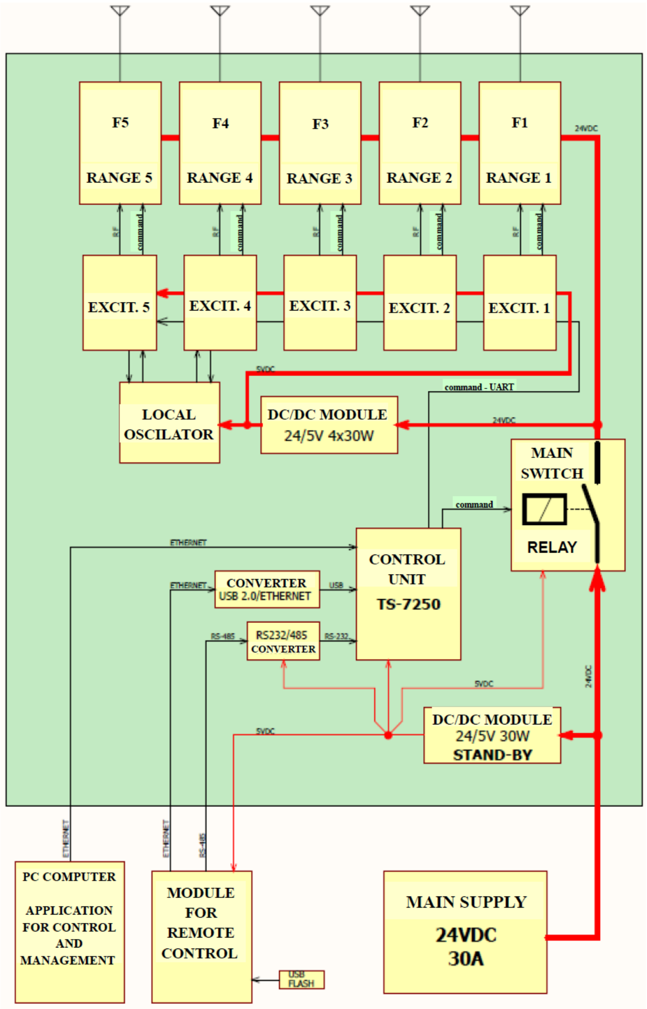

Fig. 1. Block-scheme of the malicious drone jamming system

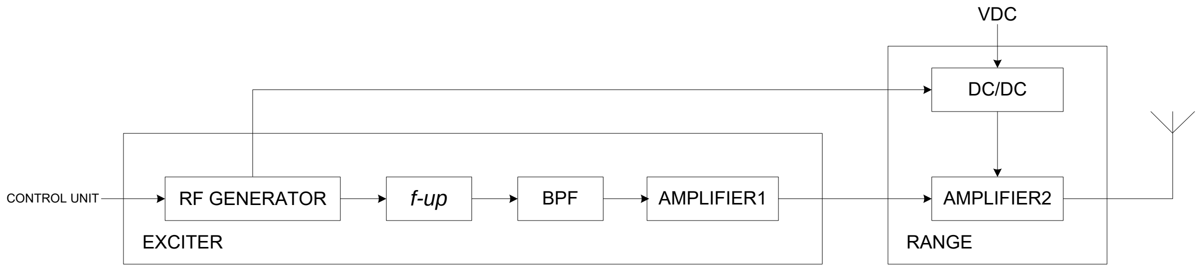

Fig. 2. Block-scheme of the EXCITER module and the output module RANGE

The jammer control and management is based on the implementation of processor board TS-7250. This module defines the functional characteristics of the EXCITER blocks for each of the five frequency bands. EXCITER blocks are based on the function of direct digital synthesis (DDS). After jamming signal generation and shaping in the exciter, the output signal level is achieved in the blocks designated by RANGE and further sent towards emission antennas. The signal frequencies in the last two ranges are too high for DDS realization and the function of these two segments is based on the lower frequency signal generation in the local oscillator. The signal in the local oscillator is used to shift the signal generated in DDS modules 4 and 5 to the desired frequency band by the implementation of mixers.

The control unit in the jammer exchanges information with the application software in distant PC and with the module for remote control using Ethernet and RS485 interface. Communication with the module for the remote control is realized over two converters: USB2.0/Ethernet and RS232/RS485.

The simplified, general block-scheme of the modules EXCITER and RANGE is presented in the Fig. 2. After generation of the jamming signal in RF GENERATOR, the signal frequency is up-converted (for the modules 4 and 5). Band pass filter (BPF) is used to finally achieve the desired jamming signal frequency. The obtained signal is then amplified by two amplifier stages, one in the block EXCITER and the other in the block RANGE to achieve the desired jamming signal level.

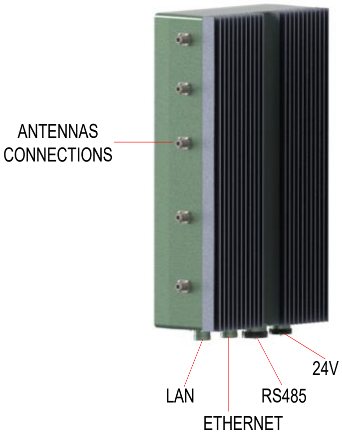

Fig. 3. Jammer device and its connections

The appearance of the jammer device is presented in the Fig. 3. Its dimensions are 640 mm x 320 mm x 155 mm. The jammer main connectors are designated in the figure as the connectors for five antennas, Ethernet and RS485 port for the connection to the remote control module and the LAN port to connect the remote PC. The last connector is for power supply 24 V. The measured device power supply current is 28.75 A from 24 V, thus obtaining total power consumption of 690 W when generating all five jamming signals. The system operating temperature range is from -20°C till +55°C. The time interval between the device switch-on till the start of jamming signal generation is 15s, while the time between the jamming signal characteristics definition change in a device menu till the moment of such signal generation start is 2s. Precision of jamming frequency definition is ±2kHz.

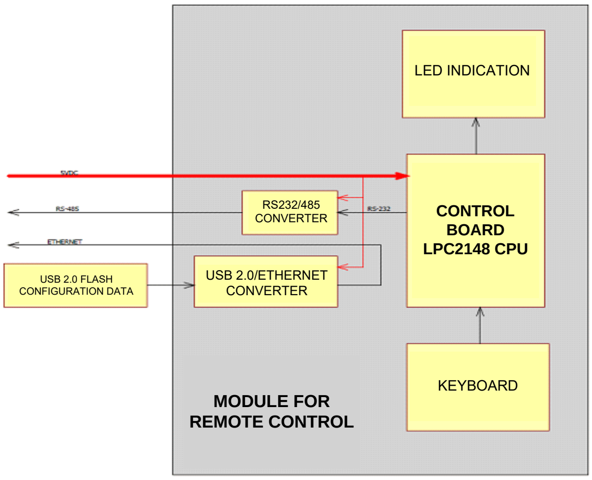

Fig. 4. Block-scheme of the module for remote control

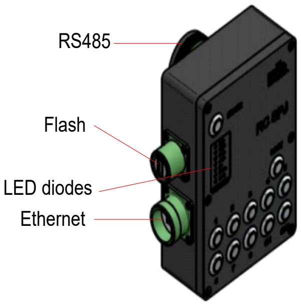

Fig. 5. Module for the remote control and its interfaces

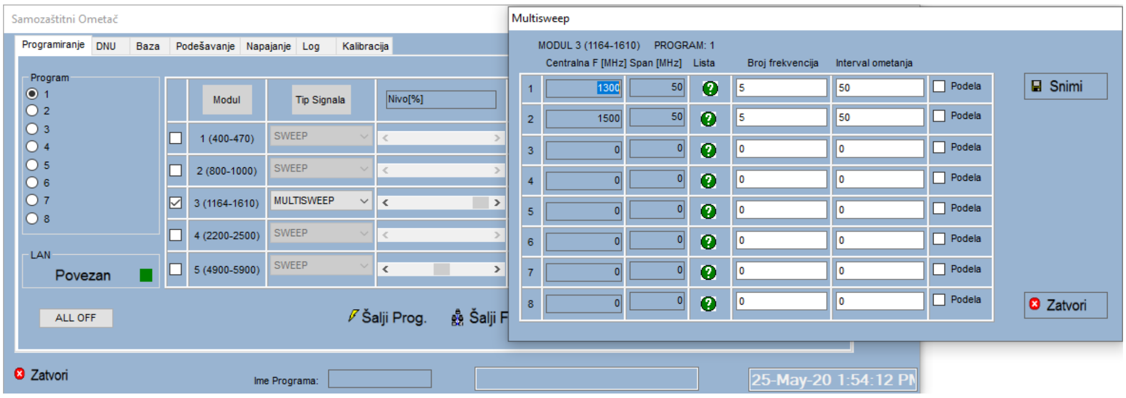

Program: ● 1 ○ 2 ○ 3 ○ 4 ○ 5 ○ 6 ○ 7 ○ 8

LAN: Povezan 🟩

	Modul	Tip Signala
☐	1 (400-470)	SWEEP
☐	2 (800-1000)	SWEEP
☑	3 (1164-1610)	MULTISWEEP
☐	4 (2200-2500)	SWEEP
☐	5 (4900-5900)	SWEEP

Ime Programa:

25-May-20 1:54:12 PM

MODUL 3 (1164-1610) PROGRAM: 1

	Centralna F [MHz]	Span [MHz]	Lista	Broj frekvencija	Interval ometanja	
1	1300	50	?	5	50	☐ Podela
2	1500	50	?	5	50	☐ Podela
3	0	0	?	0	0	☐ Podela
4	0	0	?	0	0	☐ Podela
5	0	0	?	0	0	☐ Podela
6	0	0	?	0	0	☐ Podela
7	0	0	?	0	0	☐ Podela
8	0	0	?	0	0	☐ Podela

Fig. 6. User interface for jammer control when multisweep signal with discrete sub-bands is generated

The block-scheme of the module for the remote control is presented in the Fig. 4. The control board on the base of processor LPC2148 performs information transmission between the remote module and the device over RS485 and Ethernet interface. Dimensions of this module are 170 mm x 120 mm x 55 mm and its appearance is presented in the Fig. 5 with the designated main module parts.

The module for remote jammer control replaces control from the PC. Eight press buttons with the designation 1...8 for activating one of eight predefined scenarios are obvious at the nearer lateral side of this module. Ethernet and RS485 connector for connecting the remote control module and the jammer are the lower connector at the front side and the connector at the distant lateral side, respectively. The upper connector on the front side is intended for flash placement to read predefined jamming scenarios.

Fig. 6 presents user interface (menu) in the PC to generate multisweep signal with discrete sub-bands. In the presented example the signal is generated in the third band. The parameters of the signal may be very flexibly defined. There are two sub-bands (about 1300 MHz and about 1500 MHz and five frequencies in each sub-band). The span between two discrete frequencies is 50 MHz. Jamming for other frequency bands as well as for other jamming scenarios is also applicable.

V. MEASUREMENT RESULTS

The measurement results for the third frequency band where there is a majority of jammed frequencies are presented in the Table I and in the Fig. 7. Table I presents the achieved maximum jamming signal power for all four jamming strategies. It is possible to define lower and even significantly lower emission signal level. This is especially important when considering GPS and GLONASS signal jamming. Navigation signals have very low level and it is enough to apply lower jamming signal levels. Too high jamming signal levels in this case could disrupt navigation signals at undesirably high distance outside the protected area [19], [21], where it is not necessary.

The Table II presents the maximum power of generated jamming signal for five signal sub-bands (F1 till F5) when sweep jamming strategy is applied. The similar results are obtained also for other three jamming strategies. F1 is the lowest frequency sub-band and F5 is the highest frequency sub-band. F3 covers the majority of applied frequencies for links of different type drones and these five sub-bands cover all drone frequencies mentioned in this paper.

TABLE I
THE POWER OF GENERATED JAMMING SIGNAL FOR VARIOUS JAMMING SCENARIOS

Jamming strategy	Generated signal power (dBm)	Generated signal power (W)
Sweep	46.4	43.7
Multisweep, continual sub-bands	46.4	43.7
Multisweep, discrete sub-bands	46.4	43.7
Barrage	46.2	41.7

TABLE II
THE MAXIMUM POWER OF GENERATED JAMMING SWEEP SIGNAL FOR VARIOUS FREQUENCY BANDS

Frequency band	Generated signal power (dBm)	Generated signal power (W)
F1	47.4	54.9
F2	46.2	41.7
F3	46.4	43.7
F4	44.6	28.8
F5	43	20

It is hardly possible to give exact presentation of jamming successfulness rate as a function of emitted jamming signal power, because it highly depends on the distance between the jammer and the drone. As a consequence, it is difficult to compare the jamming successfulness for various jammers from different suppliers. Two important factors which have great influence on the jamming successfulness, besides generated signal power in a jammer, are signal attenuation coefficient γ and existence/nonexistence of obstacles between the jammer and the drone. The influence of these two factors is even significantly higher than the influence of jamming power. For example, the signal power at a distance d from a jammer may be expressed as

$$P(d) = a \cdot d^{-\gamma} \qquad (1)$$

where a is the constant for adjusting values and dimensions of variables and γ has typical values between 2 and 5 [22]. It means that influence of propagation environment may cause signal attenuation in the ratio of even 8:1. Further, navigation signals should not be jammed by a too high level signal because navigation signals are also disrupted on other systems and devices where it is not desirable. As a brief illustration, according to [21] signal of the power 20mW (13dBm) is enough to block navigation signals in the range of 2km and this is significantly lower than the signal which our system may generate (Tables I and II). The jammer in [8] may cause successful jamming at 2km distance for directional jamming or 500m for omni-directional jamming. It means that our system may be effective at higher distance than solution [8].

Comparison in this case may be made when considering just signal levels at the place of signal reception. There is a number of papers whose authors include the authors of this paper where successful jamming rate (or bit error rate - BER) is determined as the level ratio RCIED activation signal/jamming signal [13]-[15], [18], [23]-[25]. Although the analysis in these papers is performed for RCIED jamming, the results may be also applied for drone jamming as the principles are the same. The results from these references prove that jamming successfulness depends on the applied jamming strategy (we have analysed the jamming strategies sweep, multisweep with continual sweeping and barrage in the mentioned papers) as well as on the jammed signal modulation type.

The frequency spectrum of the generated jamming signal is presented in the Fig. 7. for all four implemented jamming scenarios: sweep signal, multisweep signal with continuous and discrete sub-bands and barrage jamming. The signal spectrum is also related to the third frequency sub-band.

The applied jamming strategy mainly depends on the fact what data we have about the malicious drone and what drone signals we want to jam. In the case when a drone jammer is applied as a sole device, there is even no data whether a drone is present or not. It is necessary to jam a wide frequency spectrum in such a situation, perhaps by the jamming activation in all five sub-bands. The advantage of barrage jamming over sweep jamming when jamming is performed without any knowledge of drone presence is that all frequencies are jammed in the same time, but the necessary emitted power is higher than for sweep jamming [13], [14]. It means that, if jamming signal power is enough, jamming successful probability is 1 for barrage jamming and the sweep speed for sweep jamming must be determined in such a way that the probability of successful jamming is higher than some value, usually 0.95 [13], [14]. When the jammer is applied together with some system for drone detection and identification, we obtain some data about the malicious drone before jamming. Then it is possible to jam just on the frequencies where video, telemetry and drone communication signals are detected. It is possible to select to jam only one or two of these three signal groups, or only navigation signals. Thus emitted jamming signal power is significantly reduced.

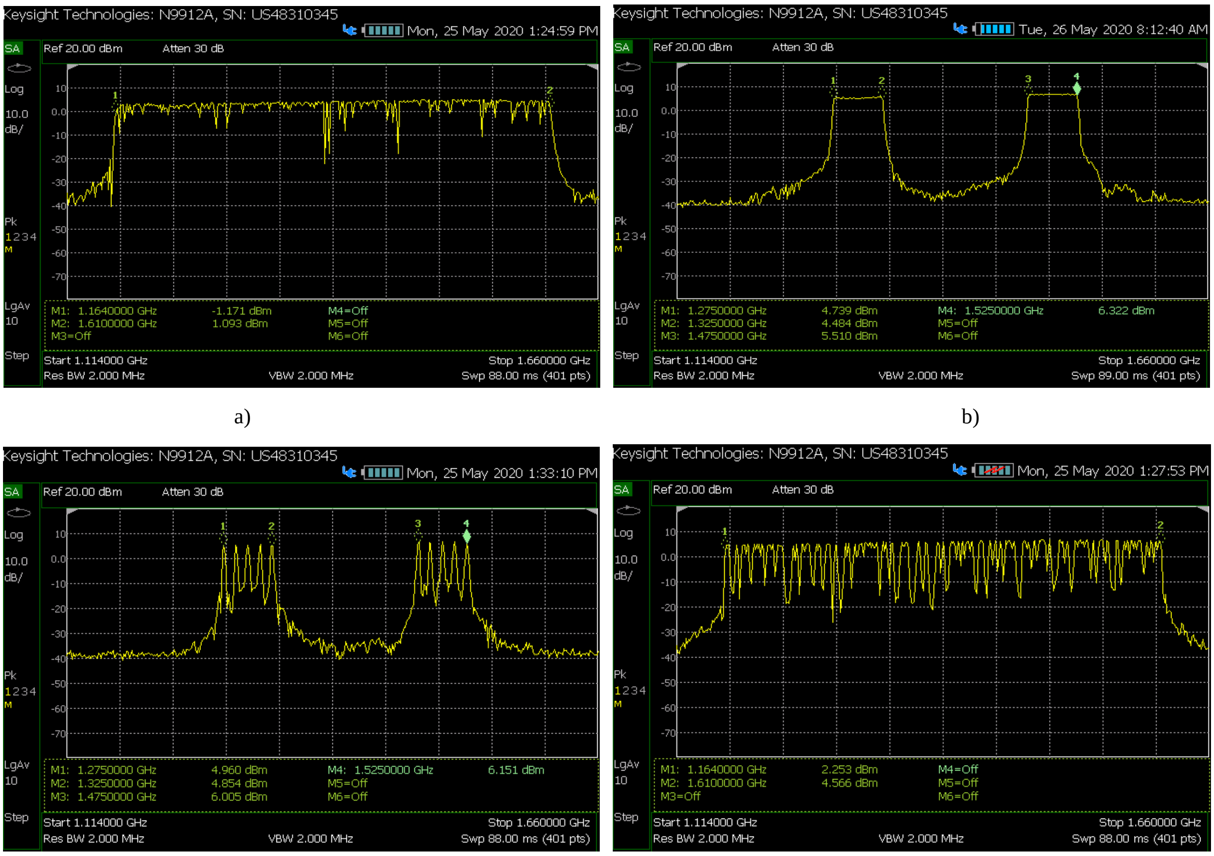

a) b)

c) d)

Fig. 7. Jamming signals in the frequency range 1164-1610MHz: a) sweep; b) multisweep with continual sweeping; c) multisweep with (five) discrete sweep steps; d) barrage

VI. CONCLUSION

The malicious drone missions jamming system presented in this paper completes IRITEL’s palette of various implementation jammers [9] - [18]. With its wide flexibility in jamming strategies definition, different implementable jamming scenarios and suggestive handling menus, the presented jammer has comparable or even better characteristics than other internationally available solutions [7], [8], [26] - [30]. In the future the realized jamming system will be supplemented by the system for drones detection, identification, classification and localization to construct one comprehensive solution for the fight against malicious drones.

REFERENCES

[1] N. Eriksson, “Conceptual study of a future drone detection system Countering a threat posed by a disruptive technology,” Master thesis in Product Development, Chalmers University of Technology, Goethenburg, Sweden, 2018.

[2] X. Shi, C. Yang, C. Liang, Z. Shi, and J. Chen, “Anti-Drone System with Multiple Surveillance Technologies: Architecture, Implementation, and Challenges,” *IEEE Communications Magazine*, Vol. 56, Issue 4, April 2018., pp. 68-74., DOI: 10.1109/MCOM.2018.1700430.

[3] N. Razzouk, J. Blas, J. Thornhill, “Speed of Saudi Oil Recovery in Focus After Record Supply Loss,” Bloomberg, 15. September 2019., https://www.bloomberg.com/news/articles/2019-09-15/saudis-race-to-restore-oil-output-after-crippling-aramco-attack.

[4] S. Milošević, “Nad Srbijom 4000 dronova, oni ilegalni biće obarani,” („Over Serbia 4000 drones, the illegal ones will be destroyed“), *Novosti*, 15. October 2017., https://www.novosti.rs/vesti/naslovna/drustvo/aktuelno.290.html:690699-Nad-Srbijom-4000-dronova-oni-ilegalni-bice-obarani, in Serbian.

[5] A. L. Drozd, “Spectrum-secure Communications for Autonomous UAS/UAV Platforms,” MILCOM 2015 - IEEE Military Communications Conference, Tampa, Florida, 26-28. October 2015.

[6] Drone Killer 6 – powerful UAV (GPS WIFI5GHz) Jammer – 120W, https://www.jammer-store.com/drone-killer-6.html.

[7] I. Pokrajac, N. Kozić, A. Čančarević, and R. Brusin, “Jamming of GNSS Signals,” *Scientific Technical Review*, Vol. 68, No. 3, UDK: 621.396.96(047)=861, pp. 18-24, September 2018.

[8] Optix Anti-drone System, Product Information, Specification & Scope of Supply, Company Confidential.

[9] P. Petrović, N. Remenski, P. Jovanović, V. Tadić, B. Pavić, M. Mileusnić, B. Mišković, “WRJ 2004 wideband radio jammer against RCIEDs,” tehničko rešenje – novi proizvod na projektu tehnološkog razvoja TR32051 pod nazivom “Razvoj i realizacija naredne generacije sistema, uređaja i softvera na bazi softverskog radija za radio i radarske mreže“, 2011., http://www.iritel.com/images/pdf/wrj2004-e.pdf.

[10] “IRITEL High Frequency (HF) radio surveillance and jamming system,” in the book M. Streetly, “*Jane’s Radar And Electronic Warfare Systems*,” IHS Global Limited, 2011.

[11] “IRITEL Very/Ultra High Frequency (V/UHF) radio surveillance and jamming system,” in the book M. Streetly, “*Jane’s Radar And Electronic Warfare Systems*,” IHS Global Limited, 2011.

[12] M. Mileusnić, B. Pavić, V. Marinković-Nedelicki, P. Petrović, A. Lebl, “Development, realization and testing the variant of the device for VIP persons protection in the extended frequency range (20MHz-6GHz) with the reduced total power (300W),” tehničko rešenje – novi proizvod na projektu tehnološkog razvoja TR32051 “Razvoj i realizacija naredne generacije sistema, uređaja i softvera na bazi softverskog radija za radio i radarske mreže“, 2017.

[13] M. Mileusnić, B. Pavić, V. Marinković-Nedelicki, P. Petrović, D. Mitić, A. Lebl, “Analysis of jamming successfulness against RCIED activation,” 5th International Conference IcETRAN 2018, Palić, June 11-14, 2018., Proceedings of Papers, pp. 1206-1211, ISBN 978-86-7466-752-1, the best paper award in the Section of telecommunications.

[14] M. Mileusnić, B. Pavić, V. Marinković-Nedelicki, P. Petrović, D. Mitić, A. Lebl, “Analysis of Jamming Successfulness against RCIED Activation with the Emphasis on Sweep Jamming,” *Facta Universitatis, Series: Electronics and Energetics*, Vol. 32, No. 2, June 2019., pp. 211-229., https://doi.org/10.2298/FUEE1902211M, extended and improved version of the paper awarded at 5th International Conference IcETRAN 2018, Palić, June 11-14. 2018.

[15] A. Lebl, M. Mileusnić, B. Pavić, V. Marinković-Nedelicki, P. Petrović, “Programmable Generator of Pseudo-White Noise for Jamming Applications,” 27th Telecommunications Forum (TELFOR), Belgrade, November 26-27, 2019., Proceedings of Papers, pp. 1-4, ISBN 978-1-7281-4790-1, DOI: 10.1109/TELFOR48224.2019.8971203.

[16] M. Mileusnić, P. Petrović, A. Lebl, B. Pavić, “Comparison of RCIED Activation Responsive and Active Jamming Reliability,” 6th International Conference IcETRAN 2019, Srebrno Jezero, June 3-5. 2019., Proceedings of Papers, pp. 988-993, ISBN 978-86-7466-785-9, the best paper in the Section of telecommunications.

[17] M. Mileusnić, P. Petrović, V. Kosjer, A. Lebl, B. Pavić, “Reliability Analysis of Different RCIED Activation Signal Responsive Jamming Techniques and Their Comparison to Active Jamming,” *Facta Universitatis, Series: Electronics and Energetics*, Vol. 33, No. 3, September 2020., pp. 459-476., DOI: https://doi.org/10.2298/FUEE2003459M, extended and improved version of the paper awarded at 6th International Conference IcETRAN 2019, Srebrno jezero, June 3-5. 2019.

[18] A. Lebl, V. Kosjer, J. Radivojević, M. Mileusnić, “Performances of RCIED Activation Signal Multisweep Jamming,” 7th International Conference IcETRAN 2020, Niš, September 28-29. 2020., Proceedings of Papers, pp. 740-745, ISBN 978-86-7466-852-8.

[19] V. Matić, V. Kosjer, A. Lebl, B. Pavić, J. Radivojević, “Methods for Drone Detection and Jamming,” 10th International Conference on Information Society and Technology (ICIST), Kopaonik, March 8-11, 2020, In: Zdravković, M., Konjović, Z., Trajanović, M. (Eds.) ICIST 2020 Proceedings Vol.1, pp.16-21, 2020.

[20] J. Radivojević, A. Lebl, M. Mileusnić, A. Vujić, T. Šević, V. Joksimović, “Multichannel Radio-jammer Development Considerations for prevention of Illicit Drone Missions,” 9th International Scientific Conference on Defensive Technologies OTEH 2020., Belgrade, October 15-16. 2020., pp. 270-275, ISBN 978-86-81123-83-6.

[21] D. A. M. da Silva, “GPS Jamming and Spoofing using Software Defined Radio,” A Dissertation for the Degree of Master in Telecommunications and Computer Engineering, University Institute of Lisbon, 2017.

[22] J. Ebersprächer, H.–J. Vögel, C. Bettstetter, “GSM, Switching, Services and Protocols,” (section 5), John Wiley & Sons, 1999.

[23] A. Lebl, B. Pavić, J. Radivojević, M. Mileusnić, P. Petrović, “Sweep Jamming Successfulness of DMPSK Modulated RCIED Activation Message,“ 28th Telecommunications Forum (TELFOR), Belgrade, November 24-25, 2020., Proceedings of Papers, pp. 21-24, ISBN 978-0-7381-4242-5, DOI: 10.1109/TELFOR51502.2020.9306587.

[24] M. Mileusnić, P. Petrović, B. Pavić, V. Marinković-Nedelicki, V. Matić, A. Lebl, “Jamming of MPSK Modulated Messages for RCIED Activation,“ 8th International Scientific Conference on Defensive Technologies OTEH 2018., Belgrade, October 11-12. 2018., pp. 380-385, ISBN 978-8681123-88-1.

[25] V. Marinković-Nedelicki, A. Lebl, M. Mileusnić, P. Petrović, B. Pavić, “BER Calculation for Sweep Jamming of MPSK Modulated RCIED Activation Message Signals,“ 18th International Symposium „INFOTEH Jahorina 2019“, Jahorina, 20-22. March 2019., ISBN: 978-1-5386-7073-6, pp. 1-6, DOI: 10.1109/INFOTEH.2019.8717747.

[26] Optix: “Anti-Drone System Compact“.

[27] https://www.perfectjammer.com/drone-signal-jammers.html.

[28] http://jammers4u.com/drones-jammer.

[29] https://www.thesignaljammer.com/blog/everything-you-need-to-know-about-drone-jammers/.

[30] Drone Killer 6 – powerful UAV (GPS WIFI5GHz) Jammer – 120W, https://www.jammer-store.com/drone-killer-6.html.

Performance Degradation of Coherent Direct Wideband Localization Due to Uncertainty in Receive Antenna Positions

Nenad Vukmirović, Miloš Janjić, and Miljko Erić

***Abstract*—In the context of passive coherent direct localization by a distributed receiving antenna array, we analyze how much the localization error increases due to non-ideal knowledge of receive antenna positions. We perform Monte-Carlo simulations with a wideband localization algorithm for a large distributed antenna array that surrounds the area were the transmitters are, and for an array of two pairs of antennas facing the area from a side. The former exhibits a very low increase in localization error, whereas the latter increases the error significantly, compared to the effect of the noise. We also derive approximate confidence intervals to confirm the validity of the drawn conclusions.**

***Index Terms*—Receive antenna position uncertainty; confidence intervals; coherent direct wideband position estimation; distributed antenna array; massive MIMO**

I. INTRODUCTION

IN this paper, we analyze a system that performs passive coherent direct wideband localization of a radio source (Tx) transmitting an arbitrarily wideband signal. The paper [1] explained the importance of wideband modeling, especially in newer generations of wireless systems. The (receive) antennas of the system are distributed in the area where the localization is performed. Therefore, we cannot assume planar wavefronts, but treat them as spherical, [2]. Each receive antenna is connected to an appropriate front-end, thus forming a single receive channel. Coherent localization requires that spatial coherence exists in the propagation medium and that the receive channels are time, frequency and phase synchronized, as described in [3], [4]. We assume that these conditions are satisfied. Even though the antennas are distributed, their front-ends could be held at the same place (collocated), such as in the example architecture in Fig. 1, which makes it easier to synchronize them. There are multiple sources of localization error in this scenario, such as the noise, interference, multipath propagation, synchronization errors and the uncertainty in the placement of the receive (Rx) antennas of the system, to mention a few.

The paper [3] showed that an error of about one thousandth of the carrier wavelength was achievable with coherent localization. A similar TDoA (Time Difference of Arrival) error (when converted to a length) was shown to be achievable in [5]. However, these results were obtained when the receive antenna positions were known exactly. The problem of accurate receive antenna placement is an important theoretical as well as practical problem, which the authors have encountered in a hardware implementation of a system for coherent localization, based on the methods in [3].

The impact of array element errors, either as (correlated) array shape distortions, independent errors of elements, or both, on the main beam direction, width, gain, as well as the sidelobe level was analyzed in [6]–[12]. The impact on direction of arrival estimation was analyzed in [13] and the impact on localization in [14]. Since the antennas in our paper are distributed, we model the element position errors as mutually independent and random. Also, since we are interested in localization of Txs inside the array aperture or close to it, the measure we use to quantify the impact of these errors is the localization accuracy.

In this paper, we are interested in the effects of the uncertainty in the Rx antenna positions on the accuracy of the mentioned type of localization. The authors of [15] proposed a method to estimate

---

N. V., M. J., and M. E. are with the University of Belgrade, School of Electrical Engineering, Serbia

N. V. and M. J. are also with the Innovation Center of School of Electrical Engineering, University of Belgrade, Serbia

M. E. is also with Vlatacom Institute, Belgrade, Serbia

This paper is a result of the research supported by the Serbian Ministry of Education, Science and Technological Development.

the position of a sensor in the array performing localization. The accuracy with which the antennas (the sensors) in the array are placed has to be greater in coherent radio localization, which this paper deals with, because, generally, the antennas have to be placed more accurately than the expected accuracy of the localization they are used for. Besides providing user location information for location-based services, the main purpose of coherent localization is to improve link performance in wireless systems, [16]. One such application of localization is in distributed beamforming. Distributed beamforming is robust with respect to the ambiguity problem, which exists in coherent localization (as explained on page 12 in [3]), so we do not focus on it in this paper. Many of the papers dealing with localization usually assume perfectly known Rx antenna positions, so it is important to analyze the effects of imperfect knowledge of Rx antenna positions. The results of this paper are important for selecting methods for measuring the geometrical relations (such as distances) between the antennas of the localization system, as well as for any applications that rely on accurate location estimation (with subwavelength accuracy) of radio transmitters.

II. PROBLEM FORMULATION

Specifically, we want to quantify the increase in localization error due to the Rx antenna placement error compared to the noise-only scenario. To that end, we will use a signal model similar to that in [3], given by

$$u_m(t) = a_m \exp\left(-\mathrm{j}\omega_\mathrm{c}\left(t_0+\tau_m\right)\right) s\left(t-t_0-\tau_m\right)+\eta_m(t), \tag{1}$$

where $u_m(t)$ is the signal in Rx channel m, $m \in \{1, 2, \ldots, M\}$, M is the number of the Rx antennas, a_m is a real-valued attenuation coefficient, $\omega_\mathrm{c} = 2\pi f_\mathrm{c}$ is the carrier frequency, t_0 is the unknown shift between the Tx and Rx time axis, $\tau_m = d_m/c$ is the propagation delay from the Tx, at an unknown position $\vec{r}$, to Rx antenna m, at $\vec{r}_m$, c is the speed of propagation, $d_m = \|\vec{r} - \vec{r}_m\|$, and $\eta_m(t)$ is the complex additive white Gaussian noise, AWGN. Figure 1 shows the system model and geometrical relations between the antennas. Note that, in coherent localization, the phase term contains the carrier phase only, and is modeled (by the exponential term) separately from the amplitude a_m. The term $s\left(t-t_0-\tau_m\right)$ models the envelope time delay of the transmitted signal/sequence $s(t)$ (wideband modeling). The signal-to-noise ratio, SNR, in channel m is $\mathrm{SNR}_m = \mathrm{SNR}_0 d_0^2/d_m^2$, where SNR_0 is used as a reference SNR at a distance of $d_0 = 1$ m. For convenience, let the unit of time be one sampling interval. This does *not* mean that the time variables/parameters are integers.

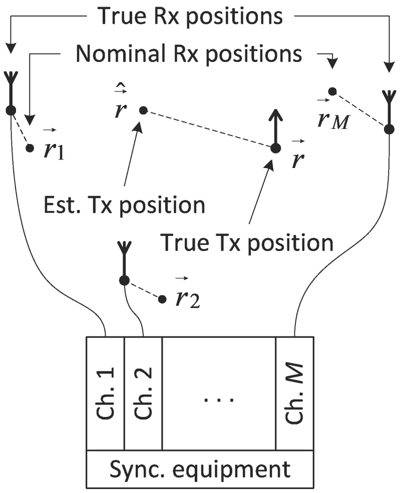

Fig. 1. The system model.

In each channel m, the samples available to a localization algorithm are $u_m(t)$, for $t \in \{0, 1, \ldots, N-1\}$. The algorithm computes an estimate of the Tx position, $\widehat{\vec{r}}$, with an error $\Delta r = \|\widehat{\vec{r}} - \vec{r}\|$. The root-mean-squared localization error is

$$\mathrm{RMSE} = \sqrt{\mathrm{MSE}} = \sqrt{\mathrm{E}\,\Delta r^2}. \tag{2}$$

Since the Rx antenna positions, $\vec{r}_m$, are random variables, we can define the receive antenna RMSE, the RxRMSE, similarly. Since different methods can be used to position the Rx antennas, we use a generic model for the position errors. Let us assume that the error of each $\vec{r}_m$ along each of the axes (x and y; if antennas are distributed in 3D, then also z) is an independent 0-mean Gaussian random variable with the same variance σ_ax^2. Therefore RxRMSE is either $\sigma_\mathrm{ax}\sqrt{2}$ for 2D or $\sigma_\mathrm{ax}\sqrt{3}$ for 3D localization. The goal is to analyze how much the RMSE increases with RxRMSE.

III. LOCALIZATION WITH ANTENNA POSITION UNCERTAINTY: ERROR ANALYSIS

We estimated the RMSE (which contained the effects of both the noise and the Rx antenna position uncertainty) through Monte-Carlo simulations for segments of random Gaussian transmitted sequences that were $N = 256$ samples long. The carrier frequency was 60 GHz and the bandwidth was 100 MHz. We used the SCM-MUSIC from [3] as a representative of coherent localization methods for unknown transmitted sequences. For a given set of Rx antenna positions, i.e. the array geometry, the true positions were randomly generated for each simulation run according to the given RxRMSE.

A. Approximate Confidence Intervals

We will characterize the quality of an estimate of the localization RMSE by an approximate confidence interval. To that end, we first note the distribution of the estimator $\widehat{\text{MSE}}$. We have that $\widehat{\text{MSE}}$ is the mean of the values Δr_k^2, $k \in \{1, 2, \ldots, K\}$, where K is the number of Monte-Carlo runs and Δr_k is the Euclidean distance between the estimated and the true location of the transmitter (i.e. the location error). The values Δr_k^2 are i.i.d. random variables, so, according to the Central limit theorem, the distribution of $\left(\widehat{\text{MSE}} - \mu\right)/\sigma$ is $\mathcal{N}(0, 1)$, where μ and σ^2 are the mean and variance of $\widehat{\text{MSE}}$, respectively. Further, we have $\mu = \operatorname{E} \Delta r_k^2 = \text{MSE}$ (the true value) and $\sigma^2 = \operatorname{Var} \Delta r_k^2 / K$.

For a given level of confidence, p, define ε as $\mathcal{P}(|\xi| \le \varepsilon) = p$, where $\xi \sim \mathcal{N}(0, 1)$. Therefore,

$$\varepsilon = \sqrt{2}\, \operatorname{erfc}^{-1}(1 - p)\,. \tag{3}$$

Next, recall that

$$\Delta r_k^2 = \Delta x_k^2 + \Delta y_k^2 + \Delta z_k^2, \tag{4}$$

where Δx_k, Δy_k, and Δz_k are the individual errors along the coordinate system axes (for 2D localization $\Delta z_k = 0$). We assume that they are 0-mean Gaussian random variables with an unknown level of correlation. Thus, Δr_k^2 is expected to have a chi-square distribution with n degrees of freedom, $\chi^2(n)$, where we expect $n = 2$ in the case when the Tx is inside the aperture of the array for 2D localization, $n = 3$ inside the aperture for 3D localization, and $n = 1$ when the individual errors are highly correlated or when one of them is dominant over the other two (when the Tx is outside the array aperture). For a random variable $W_n \sim \chi^2(n)$, we rely on

$$\operatorname{Var} W_n = \frac{2}{n} \left(\operatorname{E} W_n\right)^2, \tag{5}$$

as a property of the chi-square distribution. Combining the previous properties, we obtain

$$\mathcal{P}\left(\left|\widehat{\text{MSE}} - \text{MSE}\right| \le d\right) = p, \tag{6}$$

where

$$d = \varepsilon \sqrt{\frac{\operatorname{Var} \Delta r_k^2}{K}} = \text{MSE} \cdot \varepsilon \sqrt{\frac{2}{nK}}. \tag{7}$$

To approximate this, we use $n = 1$ as the worst case (the one that produces the widest confidence interval) and, since MSE is unknown, we use $\widehat{\text{MSE}}$ instead:

$$\widehat{d} = \widehat{\text{MSE}} \cdot \varepsilon \sqrt{\frac{2}{K}}. \tag{8}$$

Instead of using an absolute confidence interval $\left[\widehat{\text{MSE}} - \widehat{d}, \widehat{\text{MSE}} + \widehat{d}\right]$, we can use a relative one, $\left[\widehat{\text{MSE}}/\delta^2, \widehat{\text{MSE}} \cdot \delta^2\right]$, by defining δ as $\widehat{\text{MSE}}/\delta^2 = \widehat{\text{MSE}} - \widehat{d}$. This produces an approximate confidence interval for the $\widehat{\text{RMSE}} = \sqrt{\widehat{\text{MSE}}}$,

$$\left[\widehat{\text{RMSE}}/\delta, \widehat{\text{RMSE}} \cdot \delta\right], \tag{9}$$

where

$$\begin{aligned}\delta &= \sqrt{\frac{1}{1 - \varepsilon\sqrt{\frac{2}{K}}}} = \\ &= \left(1 - \frac{2}{\sqrt{K}} \operatorname{erfc}^{-1}(1 - p)\right)^{-1/2}.\end{aligned} \tag{10}$$

Note that one convenient property of δ is that it does not depend on either the geometry, or the value of the MSE. It only depends on the number of simulation runs, K, and the chosen level of confidence, p. This formula is also useful for determining the number of simulation runs needed for a confidence interval of a given width.

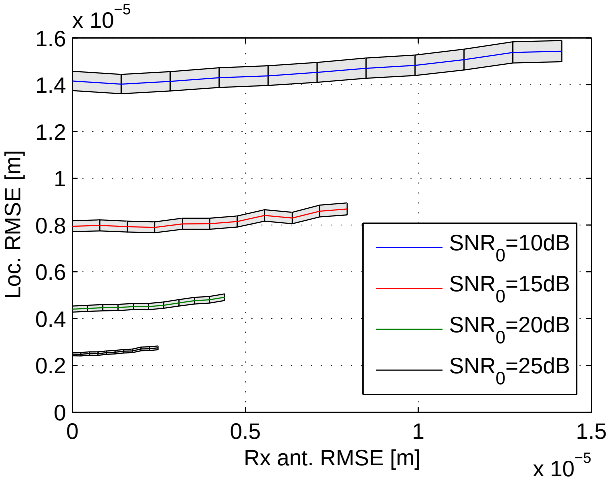

Fig. 2. The localization RMSE vs RxRMSE for different values of SNR_0 for the array geometry G_{18}.

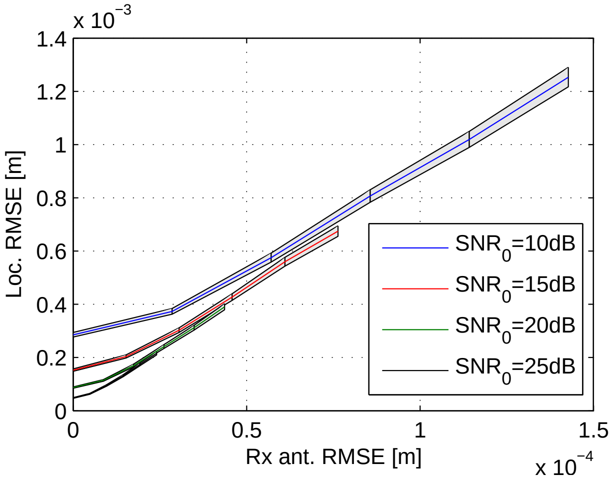

Fig. 3. The localization RMSE vs RxRMSE for different values of SNR_0 for the array geometry G_4.

B. Simulation Results

The results for different SNRs were generated for $K = 4096$ runs. The width of the confidence intervals (9), for $p = 0.99$, was then determined by $\delta = 1.03$, (10).

Figure 2 shows the results for a geometry G_{18}, used in [3], and based on [17], for localization in the horizontal plane 1.2 m below the array. The Tx was roughly below the center of G_{18}. The SNRs in the channels were grouped around the value 6 dB below SNR_0. The figure shows four curves for SNR_0 values of 10, 15, 20, and 25 dB. Note that they were evaluated only for RxRMSE below the RMSE of localization when there is no Rx antenna uncertainty, because it only makes sense that the accuracy of Rx antenna placement is greater than the accuracy of the localization method for the Tx. The curves show a very low increase in localization RMSE with an increase of RxRMSE. This can be explained by the fact that the number of Rx antennas is relatively large, they surround the area where the Tx is expected to be, and the placement errors are independent, so that all antennas would not move the main lobe of the localization algorithm in the same direction. Instead, those errors tend to partially cancel each other out, so the dispersion of the maximum of the main lobe is increased only slightly.

On the other hand, if some of the Rx antennas are close to each other (the antennas are grouped into subarrays), the number of antennas is small, or they do not surround the area where the Tx is, a much larger increase in RMSE is expected. Figure 3 confirms this and shows the results for a geometry G_4 with two subarrays of two antennas each, with their broadsides facing the area in front of the array. The (x, y) coordinates in [m] of the Rx antenna positions were $(0.0884, -0.0884)$, $(-0.0884, 0.0884)$, $(2.5316, -0.0884)$, and $(2.7084, 0.0884)$. The Tx was placed in front of the array at $(1.3, 1.5)$ in [m] and the distance to the Rx antennas was around 2 m. This means that the actual SNRs were 6 dB below SNR_0. To make the comparison fair, the curves were then evaluated for the same values of SNR_0 as for the G_{18} case. The increase in RMSE for the maximum mentioned RxRMSE was very large (around 9 times) so the curves are only shown for values below one half of that.

It would also be worthwhile to explore how the localization RMSE scales with the number of Rx antennas, m. However, to make the comparison for different values of m fair, for each m the array geometry should be optimized in some way. If the geometries were deterministic, it is unlikely that the geometry for m can be generated form the geometry for $m - 1$ by adding a single antenna without changing the positions of the others. If the geometries were random, the RMSE values should be averaged over different realizations of these geometries for all considered m. A uniform circular array could be considered for a fair comparison, but there are practical limitations that need to be considered as well, e.g., the antennas would probably be placed on walls or possibly on the ceiling of a room (in which the localization occurs), so this constrains the positions of the antennas to a rectangle/cuboid. However, since strict optimization of the Rx array geometry is outside the scope of the paper, this remains as an interesting topic for future research.

IV. CONCLUSION

We analyzed the impact of receive antenna position uncertainty on the accuracy of coherent direct wideband localization by a distributed receiving antenna array. Independent Gaussian errors in receive antenna positions were assumed. According to the simulation results, the impact of this uncertainty is small compared to the effect of the noise for G_{18}, which has a large number of antennas that encompass the area where the transmitters are. On the other hand, for arrays which have a small number of antennas, or have closely packed subarrays of antennas, especially when the transmitter is outside the aperture, such as G_4, the degradation of localization accuracy is rather large. The confidence intervals show that these effects are due to the Rx antenna positions uncertainty, and not merely due to the randomness in the simulations.

REFERENCES

[1] B. Wang, F. Gao, S. Jin, H. Lin, G. Y. Li, S. Sun, and T. S. Rappaport, “Spatial-wideband effect in massive MIMO with application in mmWave systems,” *IEEE Communications Magazine*, vol. 56, no. 12, pp. 134–141, 2018.

[2] K. Han, Y. Liu, Z. Deng, L. Yin, and L. Shi, “Direct positioning method of mixed far-field and near-field based on 5G massive MIMO system,” *IEEE Access*, vol. 7, pp. 72 170–72 181, 2019.

[3] N. Vukmirović, M. Erić, M. Janjić, and P. M. Djurić, “Direct wideband coherent localization by distributed antenna arrays,” *Sensors*, vol. 19, no. 20, p. 4582, 2019.

[4] N. Vukmirović, M. Janjić, P. M. Djurić, and M. Erić, “Position estimation with a millimeter-wave massive MIMO system based on distributed steerable phased antenna arrays,” *EURASIP Journal on Advances in Signal Processing*, vol. 2018, no. 1, p. 33, 2018.

[5] M. Janjić, N. Vukmirović, and M. Erić, “TDOA, frequency and phase offsets estimation taking into account carrier phase of arrival,” *Radioengineering*, vol. 26, no. 4, pp. 1143–1150, 2017.

[6] X. T. Ye, W. T. Li, and W. H. Du, “An equivalent method of position error caused by the array antenna deformation,” *Progress In Electromagnetics Research Letters*, vol. 74, pp. 53–60, 2018.

[7] M. Mowlér, B. Lindmark, E. G. Larsson, and B. Ottersten, “Joint estimation of mutual coupling, element factor, and phase center in antenna arrays,” *EURASIP Journal on Wireless Communications and Networking*, vol. 2007, no. 1, p. 30684, 2007.

[8] P. Marron, “Gain of phased array antennas under small random errors in element placement,” *M.D. thesis, Drexel University*, June 2014.

[9] T. Lindgren and J. Borg, “A measurement system for the position and phase errors of the elements in an antenna array subject to mutual coupling,” *International Journal of Antennas and Propagation*, vol. 2012, pp. 1–8, 2012.

[10] C. Wang, Y. Wang, X. Yang, W. Gao, C. Jiang, L. Wang, Y. Zhang, and M. Wang, “Effect of randomness in element position on performance of communication array antennas in internet of things,” *Wireless Communications and Mobile Computing*, vol. 2018, no. 2, pp. 1–8, 2018.

[11] M. Lanne, “Design aspects and pattern prediction for phased arrays with subarray position errors,” in *2010 IEEE International Symposium on Phased Array Systems and Technology*, 2010, pp. 440–446.

[12] H. S. C. Wang, “Performance of phased-array antennas with mechanical errors,” *IEEE Transactions on Aerospace and Electronic Systems*, vol. 28, no. 2, pp. 535–545, 1992.

[13] R. Pöhlmann, E. Staudinger, S. Zhang, S. Caizzone, A. Dammann, and P. A. Hoeher, “In-field calibration of a multi-mode antenna for DoA estimation,” in *2021 15th European Conference on Antennas and Propagation (EuCAP)*, 2021, pp. 1–5.

[14] J. M. Fresno, G. Robles, B. G. Stewart, and J. M. Martínez-Tarifa, “The influence of antenna positioning errors on the radio-frequency localization of partial discharge sources,” in *3rd International Electronic Conference on Sensors and Applications*, 2016, pp. 1–7.

[15] J. C. Chen, R. E. Hudson, and K. Yao, “Maximum-likelihood source localization and unknown sensor location estimation for wideband signals in the near-field,” *IEEE Transactions on Signal Processing*, vol. 50, no. 8, pp. 1843–1854, 2002.

[16] R. Di Taranto, S. Muppirisetty, R. Raulefs, D. Slock, T. Svensson, and H. Wymeersch, “Location-aware communications for 5G networks: How location information can improve scalability, latency, and robustness of 5G,” *IEEE Signal Processing Magazine*, vol. 31, no. 6, pp. 102–112, 2014.

[17] “BK connect acoustic camera consisting of acoustic camera type 9712-W-FEN and BK connect array analysis type 8430,” https://www.bksv.com/-/media/literature/Product-Data/bp2534.ashx.

Coherent Method for Radio-Frequency Measurement of Distance between Antennas

Nenad Vukmirović, Miloš Janjić, Nikola Basta, and Miljko Erić

Abstract—**The paper proposes a coherent method for radio-frequency measurement of the effective distance between two antennas. A transmitter sends a known waveform to a receiver, which processes the received signal to estimate its delay. The two transceivers are mutually synchronized, but different sources of delays/phase shifts still remain. A calibration step enables the system to estimate the total delay including the delays in the antennas. Differential measurements with three antennas enable us to estimate the delays in the antennas, which can be used as correction factors in measurements of the effective distance without the nuisance delays. The results of experiments performed on a prototype system, built of off-the-shelf equipment, show the consistency and the variance of the estimates. This method could be used to measure the geometry of a distributed array during its deployment, for the purposes of localization.**

Index Terms—**Precise antenna positioning; coherent delay estimation; Universal Software Radio Peripheral; calibration; differential measurement**

I. INTRODUCTION

THIS paper proposes a radio-wave-based method for measuring the distance between two antennas and provides the results of experimental verification.

An approach for precise positioning of antennas in an ultra-wideband (UWB) system for indoor self-localization was discussed in [1]. It was found that a major source of localization error were the errors in the positions of the system's antennas. If the distance for each pair of antennas were measured accurately, the geometry of the distributed antenna array could be inferred and used for accurate localization. However, one should carefully consider which point of an antenna is the one that correctly represents it (the referent point). The best point is the one from which the radio wave propagates directly outward at the radio frequency which the antenna will be used for. This point is the antenna phase center. This complicates physical-distance measurements because the phase center may well be inside the body of the antenna (inaccessible for fine mechanical measurements) and it generally depends on the frequency as explained in [2], [3], [4]. These papers discuss measurement methods of the coordinates of an antenna's phase center and the complications that arise.

We propose a method based on RF (Radio Frequency) transmission and signal processing, which estimates the inter-antenna distance. This distance naturally corresponds to the phase centers and we call it the *effective distance*. Additionally, this allows us to circumvent the measurement of phase center positions and the complications associated with fine mechanical measurements of the distance between them. This represents an extension of the work in [5], which proposed a method for effective distance estimation based on group-delay and provided simulation results for different antenna orientations.

The paper [6] presented a method for coherent measurement of the distance between antennas (and the clock drift of their front-ends) up to an additive constant. We build on this idea by proposing a method that is also coherent, but is able to measure the absolute distance, thanks to a special calibration step and additional differential measurements that allow us to compensate for unwanted delays in the hardware, while having less stringent requirements on the synchronization of the front-ends. We use off-the-shelf equipment, including USRP (Universal Software Radio Peripheral) devices.

Coherent delay estimation, although potentially a lot more accurate than non-coherent methods, has an inherent ambiguity problem. Namely, the estimation error is a sum of an integral and fractional

---

N. V., M. J., N. B., and M. E. are with the University of Belgrade, School of Electrical Engineering, Serbia

N. V. and M. J. are also with the Innovation Center of School of Electrical Engineering, University of Belgrade, Serbia

M. E. is also with Vlatacom Institute, Belgrade, Serbia

This paper is a result of the research supported by the Serbian Ministry of Education, Science and Technological Development.

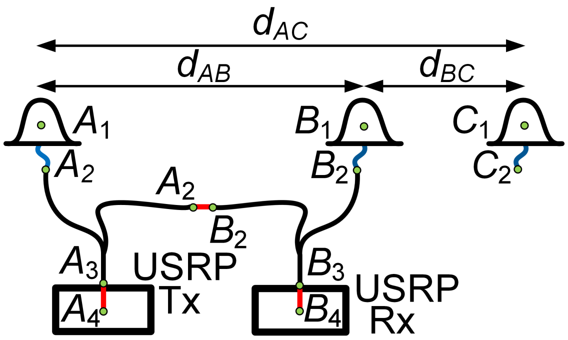

Fig. 1. The measurement setup with two USRP devices (Tx and Rx).

multiple of the carrier wavelength, the integral part representing the ambiguity. Even though the fractional error can be very small, applications that rely on accurate total distance measurements require the ambiguity to be resolved. The paper [7], although for a completely different setup (optical measurement), also has a method with the same error structure (see Sec. 2.3) and proposes a sophisticated method for resolving the ambiguity. In our paper we use a very coarse (and, therefore, simple) mechanical measurement of distance to resolve the ambiguity.

The most important application of the proposed method is measuring the (arbitrary) geometry of a distributed antenna system, for use in coherent localization [8], [9], which in turn can be used to improve the link performance of wireless systems, [10], by means of distributed beamforming or spatial multiplexing, to name a few.

II. PROBLEM FORMULATION

One USRP (Tx) transmits a predefined periodic waveform and another (Rx) receives the signal, which is then processed (see Fig. 1). One period of the waveform is determined by a vector of samples (a sequence), denoted by $\mathbf{s} = [s_0, s_1, \ldots, s_{N-1}]^\top$. Sequence $\mathbf{s}$ is a priori known at the Rx side and the processor estimates its delay with respect to the local Rx time axis.

The estimate is coherent, which means that the information is extracted not only from the signal envelope, but also from the carrier phase. This relies on the fact that when the delay of a signal in the RF domain increases by some $\Delta\tau$, the envelope is time-shifted by $-\Delta\tau$ and the carrier phase by $-\omega_\text{c}\Delta\tau$ (their shifts are coupled), where $\omega_\text{c} = 2\pi f_\text{c}$ is the carrier frequency.

Due to the restrictions of the off-the-shelf equipment used in the measurements, we have to consider different kinds of sources of error. A coherent algorithm requires the USRPs to be frequency synchronized. However, phase errors remain due to discrepancies in the lengths of the paths for the frequency reference (from a common source) in the two front-ends and the phase-locked loops (PLLs). There are also delays in the front-ends to (or from) the referent points in the chassis RF connectors (A_4A_3 and B_3B_4 in Fig. 1), in the signal cables between these connectors and the antenna connectors (A_3A_2 and B_2B_3), and between these and the referent points in the antennas (A_2A_1 and B_1B_2). Points A_1 and B_1 are not necessarily the phase centers of the antennas (in many antennas phase centers are not uniquely defined), but are chosen as geometrical reference points of antennas A and B. The algorithm considers that an RF wave propagates in free space between these points.

There is also a mismatch between the Tx and Rx local time axes, denoted by t_0. We wish to estimate the effective distance between antennas A and B, denoted by $d_{AB} = d\,(A_1B_1)$. We convert between delays and effective distances as $d_{AB} = c\tau_{AB}$, where c is the *free-space* propagation velocity of an RF wave at the given carrier frequency (by convention).

A phase drift exists, but its mean value is 0 and its variance is negligible because the propagation distances in the experiment are relatively short. There is also the clock drift, $\tau_\text{clk}(t)$, which can accumulate over time (its mean is not 0) because of independent clock generators in USRPs, but it only impacts the signal envelope. There can also be frequency-selective attenuation (e.g. due to anti-aliasing filters, coaxial cables, A/D or D/A converters...), which we separate into two factors – a delay (phase and time delay) and a waveform distortion factor (modeled by an unknown impulse response $h(t)$). Accounting for all these effects, we can write the model of the received signal, $u(t)$, as

$$\begin{aligned} u(t) =& s_\text{r}(t) + \eta(t) \\ s_\text{r}(t) =& a\mathrm{e}^{-\mathrm{j}(\omega_\text{c}\tau_\text{a}+\varphi)}\left(h * s\right)\left(t - \tau_\text{a} - \tau_\text{clk}(t)\right), \end{aligned} \quad (1)$$

where τ_a is the total constant envelope delay (which also includes the Tx t-axis shift t_0), $\omega_\text{c}\tau_\text{a} + \varphi$ is the total constant phase delay, $(h * s)(\cdot)$ is the convolution of the transmitted signal $s(t)$ with the impulse response $h(t)$ (modeling the effects in the entire path form the D/A converter in Tx to the A/D converter in Rx), $\tau_\text{clk}(t)$ is a process that slowly varies over time, a is a positive real-valued amplitude coefficient and $\eta(t)$ includes noise, multipath propagation and interference.

Note that we have normalized frequency values by the sampling frequency, $\widetilde{f}_\text{s}$, and time values by the sampling interval, $1/\widetilde{f}_\text{s}$, so that we can simply write $s(t) = s_t$, $t \in \{0, 1, \dots, N-1\}$ (a convenient way to switch between the analog and the digital domain). This, however, does *not* restrict the argument for $s(\cdot)$ to a set of integers – $s(t)$ is still a continuous waveform. This also implies that c is normalized such that $c = \widetilde{c}/\widetilde{f}_\text{s}$ and has a unit [m/sample], where $\widetilde{c} = 3 \cdot 10^8$ m/s. If we need to explicitly write a parameter in physical units, we will use the symbol $\widetilde{\ }$ above it (e.g. $\widetilde{f}_\text{c} = 1.2$ GHz).

Since the estimation algorithm (described in Sec. III) is robust against the effects of $h(t)$, we will omit it. Also, since the algorithm is coherent, it perceives the phase delay φ as a time delay equal to φ/ω_c. So, by substituting $\tau = \tau_\text{a} + \varphi/\omega_\text{c}$, we get a simplified model of the useful signal $s_\text{r}(t)$:

$$s_\text{r}(t) \approx a\text{e}^{-\text{j}\omega_\text{c}\tau} s(t - \tau - \tau_\text{e}(t)), \tag{2}$$

where τ is the total constant delay (for both the envelope and phase) and $\tau_\text{e}(t) = \tau_\text{clk}(t) - \varphi/\omega_\text{c}$ is the excess envelope-only delay (a slowly varying process).

III. THE MEASUREMENT METHOD

A basic measurement consists of acquiring a signal segment of N samples, given by

$$\mathbf{u} = [u(0), u(1), \dots, u(N-1)]^\top \tag{3}$$

and estimating the delay of the sequence $\mathbf{s}$ within that segment by the GCC-type (Generalized Cross-Correlation) delay-estimation algorithm given in [8],

$$\widehat{\tau} = \underset{\tau\in[0,N)}{\arg\max} \operatorname{Re}\left(\mathbf{u}^\text{H}\mathbf{s}_{-\tau}\right) \tag{4}$$

where $\mathbf{s}_{-\tau} = \text{e}^{\text{j}\omega_\text{c}\tau}\left[s(\tau), s(\tau+1), \dots, s(\tau+N-1)\right]^\top$ is a vector of samples of the waveform $s(t)$ time-shifted by τ (or delayed by $-\tau$) *including* the coupled carrier phase shift, Re denotes the real part, $^\top$ matrix transpose, and $^\text{H}$ conjugate transpose. Since $s(t)$ is periodic with period N, a regular time shift is the same as a cyclic time shift, thus we can compute $\mathbf{s}_{-\tau}$ using DFT (Discrete Fourier Transform) as

$$\begin{aligned}
\mathbf{s}_{-\tau} &= \mathbf{F}^\text{H}\mathbf{D}_{-\tau}\mathbf{F}\mathbf{s}, && (5)\\
\mathbf{F} &= 1/\sqrt{N}\exp(-\text{j}2\pi/N \cdot \mathbf{k}\mathbf{n}^\top), && (6)\\
\mathbf{D}_{-\tau} &= \exp(\text{j}\omega_\text{c}\tau)\operatorname{Diag}\{\exp(\text{j}2\pi/N \cdot \mathbf{k}\tau)\}, && (7)\\
\mathbf{n} &= [0, 1, \dots, N-1]^\top, && (8)\\
\mathbf{k} &= [-N/2, -N/2+1, \dots, N/2-1]^\top. && (9)
\end{aligned}$$

$\mathbf{F}$ is a modified DFT matrix such that $\mathbf{F}^{-1} = \mathbf{F}^\text{H}$, so a numerically more efficient form of (4) is

$$\widehat{\tau} = \underset{\tau\in[0,N)}{\arg\max} \operatorname{Re}\left(\mathbf{U}^\text{H}\mathbf{D}_{-\tau}\mathbf{S}\right), \tag{10}$$

where $\mathbf{U} = \mathbf{F}\mathbf{u}$ and $\mathbf{S} = \mathbf{F}\mathbf{s}$ are computed only once in preprocessing.

A. Type-I Measurement

In the *antenna configuration* in Fig. 1, in which the signal cables A_3A_2 and B_2B_3 are connected to the antennas, a basic measurement provides an estimate

$$\widehat{\tau}_\text{ant} = \tau_\text{ses} + \tau_A + \tau_{AB} + \tau_B + \varepsilon_\text{ant}, \tag{11}$$

where τ_A is the delay in antenna A (from A_2 to A_1), τ_B in antenna B (i.e. B_1B_2), τ_ses is the combined effect of the signal cables and front-ends, and ε_ant is the error.

The delay τ_ses is preserved within one driver session with the USRP devices (if we neglect the effects of the drift $\tau_\text{e}(t)$), but it takes a new value (changes unpredictably) each time a new session starts. Therefore, we can perform another basic measurement within *the same* driver session, but in the *guided configuration* (see Fig. 1), in which the signal cables are connected to each other by a short connector of effective length $L = c\tau_L$ (between A_2 and B_2). We get an estimate

$$\widehat{\tau}_\text{g} = \tau_\text{ses} + \tau_L + \varepsilon_\text{g}, \tag{12}$$

where ε_g is the error. From (11) and (12) we get

$$\tau_{AB} = \widehat{\tau}' - \tau_A - \tau_B + \tau_L + \varepsilon', \tag{13}$$

where $\widehat{\tau}' = \widehat{\tau}_{\text{ant}} - \widehat{\tau}_{\text{g}}$, $\varepsilon' = \varepsilon_{\text{g}} - \varepsilon_{\text{ant}}$ is the combined error. Note that we can perform multiple basic measurements in each of the two configurations to get more accurate estimates of $\widehat{\tau}_{\text{ant}}$ and $\widehat{\tau}_{\text{g}}$, thanks to averaging. Also, since the drift in $\tau_{\text{e}}(t)$ accumulates over time, by making the session shorter, i.e. if we change the configurations (disconnect and reconnect the cables) more quickly, the negative effect of $\tau_{\text{e}}(t)$ is expected to be smaller. Taking multiple measurements can also be useful as a way to diagnose this negative effect, especially if they are spread out across the interval of the session, because this effect is expected to grow over time.

We call the procedure of acquiring one or more $\widehat{\tau}_{\text{ant}}$ and one or more $\widehat{\tau}_{\text{g}}$ estimates, all within the same driver session, a type-I measurement.

B. Type-II Measurement

We can obtain τ_L in (13) in a fine measurement by some external means, but the terms τ_A and τ_B remain unsolved. We propose to use antenna C, with the referent point C_1, such that A_1, B_1, and C_1 are colinear as in Fig. 1. In that setup, we would perform a type-I measurement with antennas A and B and another with B and C. We would then remove the antenna B, so that it does not block the propagation from A to C and perform a type-I measurement with A and C. As a result, we get

$$\tau_{AB} = \widehat{\tau}_1' - \tau_A - \tau_B + \tau_L + \varepsilon_1', \tag{14}$$
$$\tau_{BC} = \widehat{\tau}_2' - \tau_B - \tau_C + \tau_L + \varepsilon_2', \tag{15}$$
$$\tau_{AC} = \widehat{\tau}_3' - \tau_A - \tau_C + \tau_L + \varepsilon_3'. \tag{16}$$

Relying on $\tau_{AB} + \tau_{BC} = \tau_{AC}$, we get an estimate of τ_B as

$$\widehat{\tau}_B = \tau_B + \varepsilon'' = \left(\widehat{\tau}_1' + \widehat{\tau}_2' - \widehat{\tau}_3' + \tau_L\right)/2. \tag{17}$$

where ε'' is the combined error. We call this procedure of obtaining $\widehat{\tau}_B$ a type-II measurement.

Note that $\widehat{\tau}_B$ is independent of the distances between the antennas and the delays in antennas A and C, for fixed signal-to-noise ratios, as long as the antennas are in the far-field regions of one another. Additionally, a deviation of B_1 from the line A_1C_1 influences ε'' as a second-order infinitesimal, so this deviation can be neglected.

Type-II measurements can be performed for each of the antennas in an RF anechoic chamber before they are deployed. Once deployed, the estimates $\widehat{\tau}_A$, $\widehat{\tau}_B$, ... can be input into (13) as correction factors, providing

$$\widehat{\tau}_{AB} = \widehat{\tau}' - \widehat{\tau}_A - \widehat{\tau}_B + \widehat{\tau}_L. \tag{18}$$

This way we get an estimate of the effective electrical distance between A and B, $\widehat{d}_{AB} = c\widehat{\tau}_{AB}$, or any other pair of antennas we use to form a distributed antenna array. As a result, the antennas can be placed arbitrarily and then the geometry of the array can be *measured*, by multiple type-I measurements (with appropriate correction factors).

C. Integral and fractional errors

In each of these measurements, the error (such as ε' in (13)) has two components – the first is an integer multiple of the carrier cycle, $1/f_{\text{c}}$, for delays, or the carrier wavelength, $\lambda_{\text{c}} = c/f_{\text{c}}$, for lengths, and the second component is the fractional part (the remainder, which is usually a few orders of magnitude smaller than λ_{c}):

$$\begin{aligned} \varepsilon' &= m/f_{\text{c}} + \varepsilon'_{\text{frac}}, \text{ for delays} \\ c\varepsilon' &= m\lambda_{\text{c}} + c\varepsilon'_{\text{frac}}, \text{ for distances}, \end{aligned} \tag{19}$$

for some $m \in \mathbb{Z}$. The presence of $m\lambda_{\text{c}}$ is known as the (integer wavelength) ambiguity problem and it is characteristic of coherent delay algorithms [11], [12]. This effect occurs because an RF signal and its replica delayed by $1/f_{\text{c}}$ closely resemble each other. The term $\tau_{\text{e}}(t)$ increases the error, but mostly its integral part (the ambiguity). Even though the integral part of the error is usually much larger, it is not as important as the $\varepsilon'_{\text{frac}}$ part. For example, the performance of distributed beamforming is deteriorated mostly by $\varepsilon'_{\text{frac}}$ and very little by the ambiguity.

We propose to solve the ambiguity problem by taking a rough estimate of the distance, d_{AB}, by some external means (mechanical means, laser range finder, or even an RF measurement but at a different carrier frequency). That method only has to be accurate enough to correctly resolve m (e.g., at $\widetilde{f}_{\text{c}} = 1$ GHz, $\lambda_{\text{c}} = 30$ cm, an accuracy of a few centimeters would suffice).

Finally, the effective lengths/distances of the guided parts of the system can depend on $\widetilde{f}_{\text{c}}$, so care should be taken to measure them at different

Fig. 2. The experiment environment.

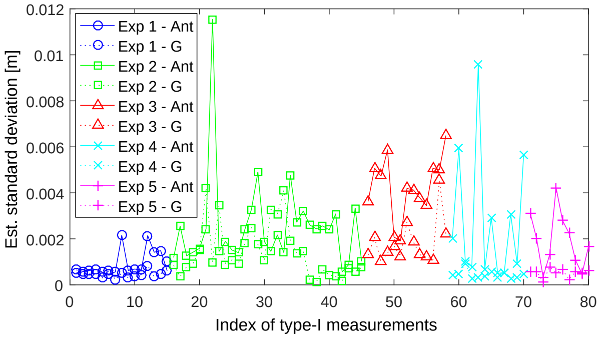

Fig. 3. Estimated standard deviations of lengths obtained within different type-I measurements.

frequencies and later use the correction factors at the correct frequency.

IV. RESULTS OF MEASUREMENTS

We performed experiments with n210 USRP devices with omnidirectional antennas (connected by 25 m long coaxial cables) in an outdoor urban environment in front of the Innovation Center of the School of Electrical Engineering in Belgrade (Fig. 2). Most of the type-I measurements consisted of 8 and 4 basic measurements in the antenna and guided configuration, respectively. To reduce the bias in the estimates, we did not use an attenuator to connect A_2 and B_2. Thus, the Rx signal level was significantly lower in the antenna configuration than in the guided one. So, we used a greater number of measurements (8) in the antenna configuration to compensate for higher error variance. We performed multiple different experiments as a proof-of-concept.

In experiment (exp.) 1, we performed a type-II measurement with antennas A, B, and C in a line in that order, at $\widetilde{f}_\text{c} = 990$ MHz. There were 5 type-I measurements for each pair of antennas (AB, BC, and AC). Fig. 3 shows standard deviations, σ_A and σ_G, of the effective length estimates in the antenna and guided configuration, respectively, within each type-I measurement. In this section, we concentrate on the std. deviations of the fractional part $c\varepsilon'_\text{frac}$ from (19) (throughout these experiments, the std. deviations of the ambiguity m in (19) were grouped around 1 and most of them were in the range between 0 to 3). In most cases, σ_A was greater than σ_G, as expected, and both were less than 7 mm. The resulting 3 groups of estimates (one for each antenna pair) had standard deviations 1.5 mm, 3.5 mm, and 2.9 mm, as shown in Table I. The final (type-II) estimate of exp. 1 (the effective length of antenna B) was $L_B = 54.94$ cm, according to (17). (This was expected because the physical length of B_1B_2 was around 40 cm, with a roughly 1.5 times lower propagation velocity.) Note that this was a two-stage averaging, which made the total number of basic measurements 120 (antenna) and 60 (guided) for this single type-II estimate.

TABLE I

PARAMETERS OF EXPERIMENTS AND STANDARD DEVIATIONS (σ).

Exp.	**Type**	**Ant. pair**	**No. of meas.**	σ **[mm]**	σ/λ_c
1	II	AB	5	1.5	0.005
		BC	5	3.5	0.012
		AC	5	2.9	0.0096
2	II	AB	10	7.7	0.025
		BC	10	2.4	0.008
		AC	10	7.8	0.026
3	II	AB	5	9.3	0.034
		BC	4	3.9	0.014
		AC	4	3	0.011
4	II	BA	4	7.6	0.025
		AC	4	2.6	0.0086
		BC	4	11.3	0.037
5	I	AB	10	5.6	0.018

To reduce the number of times the cables had to be disconnected/reconnected to a half (less wear-and-tear of connectors), we started one type-I measurement in the antenna configuration and ended it in the guided one, and then reversed the order in the next measurement. We continued alternating this order throughout the campaign. Another advantage of this was to partially compensate for the bias created by a clock drift growing in one direction over the course of a driver session. The expected effect of this was an increase in σ of type-I estimates for each pair of antennas and a decrease in the bias in the final estimate of the pair.

To test the repeatability of measurement, exp. 2 was with the same antennas and $\widetilde{f}_{\mathrm{c}}$ as in exp. 1, but in different conditions – different weather conditions (day) and inter-antenna distances. There were 10 type-I measurements for each antenna pair and the σ values of each pair (as well as the ones for the rest of the experiments in this section) are given in Table I. For individual type-I σ values, see Fig. 3. The final estimate was $L_B = 55.08$ cm.

To test the consistency across the frequencies, exp. 3 was carried out with the same setup as exp. 2, but at $\widetilde{f}_{\mathrm{c}} = 1.1$ GHz (in this experiment only). Note that the effective length B_1B_2 (L_B) was not expected to be identical at these two frequencies (even though the physical one was). The final estimate was $L_B = 56.04$ cm.

In exp. 4 the antennas were placed as B-A-C (antenna A in the middle), with the goal of estimating L_A. The final estimate was $L_A = 66.68$ cm.

Exp. 5 consisted of 10 type-I measurements with antennas A and B, but with correction factors from exps. 2 and 4 (using (18)). The aim was to estimate the effective distance between the referent points of these antennas (i.e., in the air only), L_{AB}. According to a mechanical measurement, the distance was 3.45 m. The resulting individual σ values are given in Fig. 3 and the σ value of the final result in Table I. The final estimate was $d_{AB} = 3.32$ m.

In future work, one might consider decreasing the difference in the Rx signal levels in the antenna and guided configuration, in order to reduce the influence of thermal and quantization noise, but without inducing a bias in the delay estimation. Furthermore, compensation of the remaining bias in the estimates is also of interest. Additionally, (dis)connecting cables manually is impractical for deployments of distributed antenna arrays, so the switching (between configurations) may be designed so it would be electronically controlled and automatic, thus decreasing the probability of human error in the experiment.

V. CONCLUSION

In this paper we proposed a method for measuring electronically the effective distance between a pair of antennas. A prototype was built of off-the-shelf equipment. The results of the field tests showed the potential of the presented method, as well as the aspects that require improvement in order to use it in deploying distributed antenna arrays with subwavelength accuracy. Such a method can have a great impact on future wireless systems as an enabler for coherent localization.

REFERENCES

[1] M. Erić, R. Zetik, and D. Vučić, “An approach for determination of antenna positions in distributed antenna system used for UWB indoor self-localization: Experimental results,” in *2013 21st Telecommunications Forum Telfor (TELFOR)*, 2013, pp. 204–207.

[2] H. Yuan, H. Liu, J. Jia, T. Su, and C. Zeng, “A novel algorithm to compute 3d phase center,” *Electromagnetics*, vol. 40, no. 7, pp. 486–499, 2020.

[3] P. N. Betjes, “An algorithm for automated phase center determination and its implementation,” in *AMTA*, 2007, pp. 190–195.

[4] C. Esposito, A. Gifuni, and S. Perna, “Measurement of the antenna phase center position in anechoic chamber,” *IEEE Antennas and Wireless Propagation Letters*, vol. 17, no. 12, pp. 2183–2187, 2018.

[5] N. Basta and M. Erić, “Method for estimation of electrical distance between antennas based on music-type algorithm,” in *7th International Conference on Electrical, Electronics and Computing Engineering (IcETRAN 2020)*, 2020, pp. 1–4.

[6] P. Bidigare, S. Pruessing, D. Raeman, D. Scherber, U. Madhow, and R. Mudumbai, “Initial over-the-air performance assessment of ranging and clock synchronization using radio frequency signal exchange,” in *2012 IEEE Statistical Signal Processing Workshop (SSP)*, 2012, pp. 1–4.

[7] G. Tang, X. Qu, F. Zhang, X. Zhao, and B. Peng, “Absolute distance measurement based on spectral interferometry using femtosecond optical frequency comb,” *Optics and Lasers in Engineering*, vol. 120, pp. 71–78, 2019.

[8] N. Vukmirović, M. Janjić, P. M. Djurić, and M. Erić, “Position estimation with a millimeter-wave massive MIMO system based on distributed steerable phased antenna arrays,” *EURASIP Journal on Advances in Signal Processing*, vol. 2018, no. 1, p. 33, 2018.

[9] N. Vukmirović, M. Erić, M. Janjić, and P. M. Djurić, “Direct wideband coherent localization by distributed antenna arrays,” *Sensors*, vol. 19, no. 20, p. 4582, 2019.

[10] R. Di Taranto, S. Muppirisetty, R. Raulefs, D. Slock, T. Svensson, and H. Wymeersch, “Location-aware communications for 5G networks: How location information can improve scalability, latency, and robustness of 5G,” *IEEE Signal Processing Magazine*, vol. 31, no. 6, pp. 102–112, 2014.

[11] A. J. Weiss and E. Weinstein, “Fundamental limitations in passive time delay estimation – part I: Narrow-band systems,” *IEEE Transactions on Acoustics, Speech, and Signal Processing*, vol. 31, no. 2, pp. 472–486, 1983.

[12] E. Weinstein and A. J. Weiss, “Fundamental limitations in passive time delay estimation – part II: Wide-band systems,” *IEEE Transactions on Acoustics, Speech, and Signal Processing*, vol. 32, no. 5, pp. 1064–1078, 1984.

Resolvability of Transmitters in Coherent Direct Localization

Nenad Vukmirović, Miloš Janjić, and Miljko Erić

***Abstract*—Coherent direct localization promises high accuracies, that are especially useful for improving wireless link performance (the location-aided communication concept). The focus of the paper is to analyze the spatial resolution performance of three different localization algorithms in this category in the context of spectrum sensing – i.e., their ability to successfully resolve multiple transmitters at different positions working in the same band and time interval. Namely, when two transmitters are close to each other, they interfere with the localization process, which can perceive them as a single source (and, therefore, fail to resolve them). We quantify the impact of this interference on the probability of resolution and the localization error for both cooperative and non-cooperative transmitters. The results of simulations show that, even when the distance between the transmitters is lower than the carrier wavelength, given that the inherent ambiguity problem allows, they can be resolved, with a localization error of a small fraction of the wavelength. The resolution rate is extremely high for the algorithm with a priori known waveform (for cooperative transmitters).**

***Index Terms*—Coherent direct position estimation; distributed antenna array; resolvability of multiple transmitters; spectrum sensing**

I. INTRODUCTION

THE focus of the paper is an analysis of spatial resolution performance of coherent localization methods in the context of spectrum sensing. Spatial resolution refers to the ability of an algorithm to correctly perceive two signal sources that are close to each other as two different sources and to estimate their positions, based on the received signals.

Resolution of two known waveforms in noise is analyzed in [1], such as two complex sinusoids of similar frequencies. Resolution performance of direction-of-arrival estimation for sources by a collocated sensor array is assessed in [2]. The paper [3] generalizes the resolution analysis to multiple parameters per signal (such as the spatial coordinates of its source) and multiple signals. The impact of blurring on the resolution in image-forming applications is provided in [4].

The authors of [5] discuss different criteria for successful resolution of acoustic sources for different methods. They propose the valley-to-peak ratio (VPR) as a measure of the quality of resolution. Namely, if a localization method has a criterion function whose maxima represent the estimated positions of the sources and there are two sources of equal intensity close to each other, then their maxima and the minimum between them define the VPR. Our paper is based on simulations in which the maxima corresponding to two radio transmitters are searched for starting at their true positions. If the two search instances (one for each transmitter) end at the same point, it is considered that the transmitters have not been resolved in that attempt. We quantify the performance of resolution by the probability of success and the impact on (deterioration of) the position estimation accuracy. If the VPR is low, the noise and interference have a greater chance of making the resolution process fail (we implicitly rely on the VPR for quantification). Additionally, we generalize the analysis to transmitters of different power levels.

II. PROBLEM FORMULATION

Let us consider a distributed array of M receive (Rx) antennas at known positions $\vec{r}_m$, $m \in \{1, 2, \ldots, M\}$. The Rx antennas are placed in an area where localization of transmitters (Tx) is performed. We analyze the performance of *coherent* localization. This type of localization requires a propagation medium in which the spatial coherence

---

N. V., M. J., and M. E. are with the University of Belgrade, School of Electrical Engineering, Serbia

N. V. and M. J. are also with the Innovation Center of School of Electrical Engineering, University of Belgrade, Serbia

M. E. is also with Vlatacom Institute, Belgrade, Serbia

This paper is a result of the research supported by the Serbian Ministry of Education, Science and Technological Development.

condition holds for (at least) the line-of-sight (LoS) components of the signals which the Txs transmit and the Rx array receives. This condition, [6], [7], allows us to use the additional information embedded in the carrier phases of the signals, to increase the accuracy, unlike non-coherent methods.

The raw received signals are processed by the system performing the localization (therefore the localization is *direct*). Obviously, the receiving channels (the Rx antennas, the Rx front-ends, and the signal cables between them) need to be time, frequency, and phase synchronized (t-, f-, and φ-sync). This can be achieved by means of hardware calibration or by processing beacon signals from a dedicated anchor (say, a base station). The baseband complex form of the signal each Rx channel m receives is

$$\begin{aligned} u_m(t) =& \eta_m(t) + \sum_{q=1}^{Q} s_m^{(q)}(t) \\ s_m^{(q)}(t) =& A_m^{(q)} e^{-\mathrm{j}\omega_{\mathrm{c}}\left(t_0^{(q)}+\tau_m^{(q)}\right)} s^{(q)}\left(t - t_0^{(q)} - \tau_m^{(q)}\right), \end{aligned} \tag{1}$$

where $\eta_m(t) \sim \mathcal{CN}\left(0, \sigma^2\right)$ is an independent white Gaussian noise; Q is the number of Txs; $s^{(q)}(t)$ is the waveform of Tx$_q$; $t_0^{(q)}$ models the lack of t-sync between Tx$_q$ and the Rx system; $\tau_m^{(q)}$ is the propagation time from Tx$_q$ to Rx$_m$ and $A_m^{(q)}$ is the amplitude factor; the carrier phase is in the exponent and $\omega_{\mathrm{c}} = 2\pi f_{\mathrm{c}}$ is the carrier frequency. In this model, the frequencies are normalized by the sampling frequency, $\widetilde{f}_{\mathrm{s}}$, and time values by $\widetilde{f}_{\mathrm{s}}^{-1}$, e.g. $f_{\mathrm{c}} = \widetilde{f}_{\mathrm{c}}/\widetilde{f}_{\mathrm{s}}$, $t = \widetilde{t}\widetilde{f}_{\mathrm{s}}$, $\tau_m^{(q)} = \widetilde{\tau}_m^{(q)}\widetilde{f}_{\mathrm{s}}$, and so on, where the symbol $\widetilde{\ }$ denotes values in physical units (Hz and s). To keep the analysis tractable, we restrict it to the LoS-only scenario. Then the coherence implies that $A_m^{(q)}$ is real valued.

Specifically, we are interested in analyzing the ability of localization algorithms to distinguish between different Txs which transmit in the same band and time interval (the ability to resolve them successfully) even if they are close to each other. A localization algorithm produces an estimate, $\widehat{\vec{r}^{(q)}}$, of the true (and unknown) location $\vec{r}^{(q)}$ of Tx$_q$. If, say, $\widehat{\vec{r}^{(1)}} = \widehat{\vec{r}^{(2)}}$ (to within the numerical precision), than the algorithm has failed to resolve the different transmitters Tx$_1$ and Tx$_2$. We wish to find the minimum distance between them at which they are still resolvable.

III. The Method

Unlike a system with a single classical (collocated) antenna array, which can estimate the direction of arrival of an incoming radio signal, a system with antennas distributed around the Tx area can estimate their positions, even if they are not t-synchronized with it. We perform Monte-Carlo simulations of such a scenario with $Q = 2$ Txs. We cover the inside of the Rx array aperture by a discrete set of nominal Tx points (the Tx grid). This allows us to average the results over the space. In each simulation run, the positions of Tx$_1$ and Tx$_2$ are generated with a specified distance between them and a random orientation at one of the Tx grid points.

A direct localization algorithm in this paper has a criterion function g defined over the area of interest. The only difference between g and a cost function is that a cost function is searched for its minima, whereas g is searched for its maxima. The search is initialized for each of the two Txs at its true location, $\vec{r}^{(q)}$, and it follows the gradient of g to find the maximum, which is the estimate of that Tx's location, $\widehat{\vec{r}^{(q)}}$. Multiple runs are performed at each Tx grid point to achieve a desired statistical sample size. Successful Tx resolutions are counted and the squared Euclidean distance between the estimated and true location of a Tx, $\|\widehat{\vec{r}^{(q)}} - \vec{r}^{(q)}\|^2$, is averaged. Thus, we obtain an estimate of the probability of resolution and the root-mean-square-error (RMSE) of localization for that algorithm.

We use the ML-KS (maximum likelihood – known sequence), ML-US (ML – unknown sequence), and SCM-MUSIC (steered-covariance-matrix multiple-signal classification) algorithms from [6] as representatives of coherent algorithms. ML-KS has stricter requirements for the Tx than the other two. It requires that the modulator in the Tx is coupled with its D/A converter so that the carrier phase is 0 at $t = 0$ (on the local time axis) for each processed signal segment. ML-KS also needs to know the Tx's waveform. This is suitable for localization of cooperative Txs, such as user terminals (UT) in a wireless network, where the base stations allocate training waveforms for the UTs and also perform localization.

ML-US and SCM-MUSIC impose no such restrictions and are suitable even for non-cooperative radio sources. For them, deviations in the modulator phase coupling and carrier frequency can be considered as a part of the Tx waveform itself (since it is unknown to the Rx system, anyway).

A. *Grating Lobes*

Coherent algorithms suffer from the (integer wavelength) ambiguity problem. It can be intuitively explained like this. If the system performs distributed beamforming in the downlink, than there might appear spots in the area other than the UT antenna location where the electric field vector also has an increased intensity. Localization based on uplink signals would then have high lobes in its criterion function at those spots (the sidelobes), not only at the true UT location (the main lobe).

When analyzing Tx resolvability, we have to consider not only the distance between the Tx_1's main lobe and that of the Tx_2, but also to the closest high sidelobe (the closest grating lobe) of Tx_2. This increases the chance the Txs will interfere with each other. However, if they are moving, it is expected that the overlapping of the lobes will happen only for very short periods of time, so that they would be resolvable most of the time. This definitely seems like an important topic for future research.

IV. SIMULATION RESULTS

Let us define SNR_0 as the signal-to-noise ratio (SNR) of a Tx's signal in a channel whose Rx antenna would be 1 m away from the Tx. We performed Monte-Carlo simulations with $Q = 2$ Txs, where we kept the SNR_0 of Tx_2 at 30 dB. The (power) level of Tx_1 was 0 dB, -5 dB, and -15 dB relative to Tx_2. The Rx array had 5 antennas at (x, y) coordinates $(-2.195, -1.243)$, $(0.177, -2.641)$, $(2.961, -1.056)$, $(2.534, 2.206)$, and $(-2.18, 2.237)$ in [m]. Each (Tx and Rx) antenna was assumed to have an omnidirectional radiation pattern in the plane of the array. The area inside the array's aperture was covered by a Tx grid with 28×28 points. For each point we performed $K = 3$ simulation runs. In each run, Tx_1 was placed at the corresponding Tx grid point and Tx_2 was placed randomly (with uniform distribution) on a circle centered at Tx_1 with the radius equal to the given distance between Tx_1 and Tx_2, denoted by $d_{12} = \|\vec{r}^{(1)} - \vec{r}^{(2)}\|$. The waveform of each Tx in each run was generated based on a new independent realization of a random complex Gaussian sequence of $N = 256$ samples, with $\widetilde{f}_\text{c} = 1$ GHz and $\widetilde{f}_\text{s} = 10$ MSample/s.

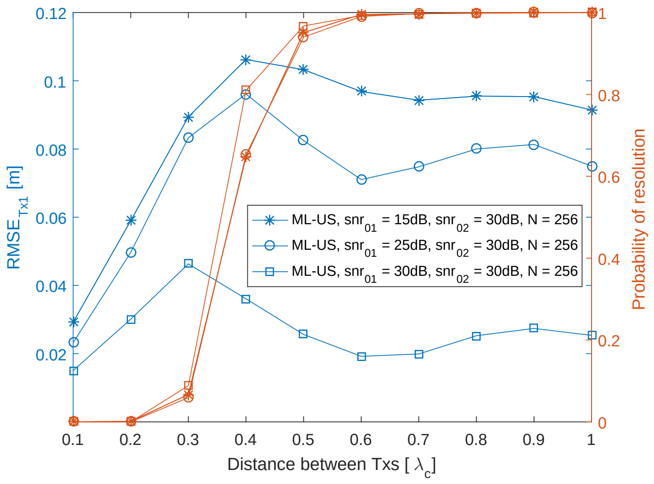

Fig. 1. Probability of resolution and RMSE vs. d_{12} for the ML-US algorithm.

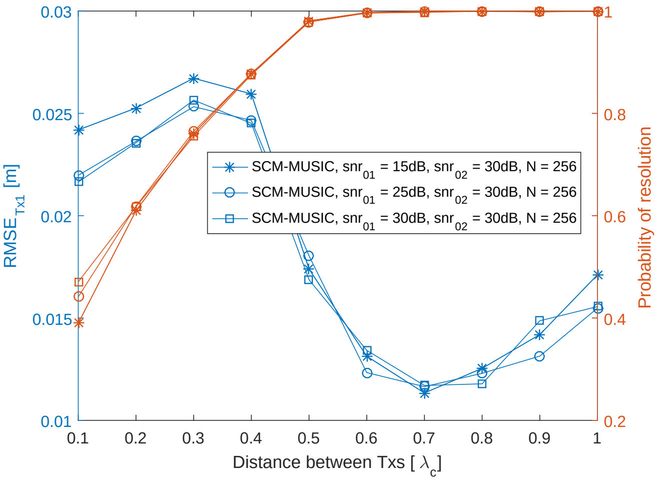

Fig. 2. Probability of resolution and RMSE vs. d_{12} for the SCM-MUSIC algorithm.

The results of simulations for the ML-US algorithm vs. the distance between the Txs (given in carrier wavelengths, λ_c) are shown in Fig. 1. The algorithm resolves the Txs in most cases when $d_{12} \geq 0.5\lambda_\text{c}$ and fails in most cases when $d_{12} \leq 0.3\lambda_\text{c}$. The RMSE for Tx_1 (the Tx with lower or equal power) is approximately in the range 2 cm – 10 cm when the Txs are successfully resolved. Then the RMSE deteriorates with decreasing d_{12}.

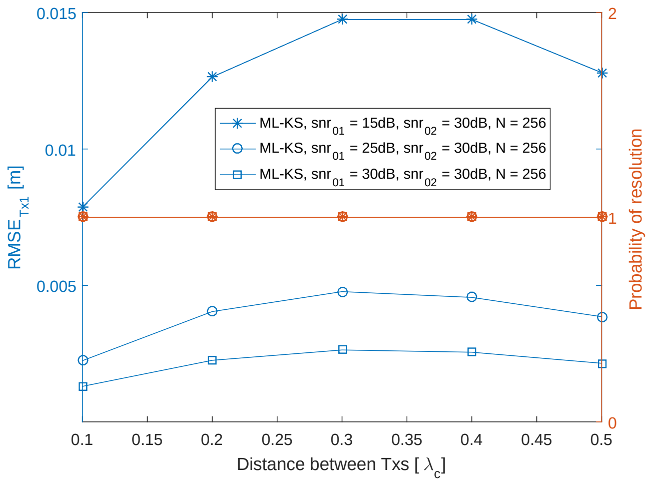

Fig. 3. Probability of resolution and RMSE vs. d_{12} for the ML-KS algorithm.

Note that the RMSE appears to improve for very low d_{12}, but that is just a consequence of Tx$_1$ location estimate being close to Tx$_2$, which itself is closer and closer to Tx$_1$ (there is no actual improvement).

The results for SCM-MUSIC are depicted in Fig. 2. This algorithm has better resolvability in the low-d_{12} region (below $0.5\lambda_c$) than ML-US. Furthermore, all three RMSE curves are similar to the ML-US curve for the best-case scenario of the given three regarding the difference in levels between Tx$_1$ and Tx$_2$ (when they transmit at an equal power), so we conclude that SCM-MUSIC is robust with respect to this difference. Better performance of this algorithm is expected, since it is based on a high-resolution algorithm (the generic MUSIC), although, this comes at the cost of higher numerical complexity.

The results for ML-KS are shown in Fig. 3. We can see that it has an extremely high resolvability across the d_{12} range (nearly 1), owing to the fact that the sequences (and waveforms, as well) of the Txs are nearly orthogonal with high probability (they are independent random vectors). We also see that the RMSE is quite low – in most cases it is below 1 cm and it is not affected much by d_{12}. This comes at a price of increased numerical complexity and the reduced scope of applications (as explained in the previous text) – the algorithm has to know the Tx's sequence, so it is mostly for cooperative applications.

One direction for future research is analyzing the impact of different levels of orthogonality between the Txs' waveforms on localization performance. Another is optimization of the Rx antenna array's geometry to suppress the ambiguity problem, effectively reducing the chance the Txs would interfere with each other in the localization process. It would also be interesting to quantify the effect of the ambiguity on localization and tracking, when the Tx is moving.

V. CONCLUSION

In this paper we presented an analysis of coherent localization performance of multiple transmitters in the same band and time interval, for three different algorithms. The SCM-MUSIC algorithm performs better than ML-US in unfavorable conditions and has the same scope of applications, but at a higher numerical cost. The ML-KS has the best performance, but at a higher numerical cost and it is usually restricted to localization of cooperative transmitters. All in all, each of the analyzed algorithms have a localization error that is a small fraction of the carrier wavelength (as long as the ambiguity problem does not cause them to fail), despite the fact that the transmitters interfere with each other.

REFERENCES

[1] A. Amar and A. J. Weiss, "Fundamental limitations on the resolution of deterministic signals," *IEEE Transactions on Signal Processing*, vol. 56, no. 11, pp. 5309–5318, 2008.

[2] J.-P. Delmas, *Performance bounds and statistical analysis of DOA estimation*. Academic Press library in signal processing, Elsevier, 2015.

[3] M. N. El Korso, R. Boyer, A. Renaux, and S. Marcos, "Statistical resolution limit for multiple parameters of interest and for multiple signals," in *Proc. of International Conference on Acoustics, Speech, and Signal Processing, (ICASSP10)*, 2010, pp. 3602–3605.

[4] G. M. Gasimova, R. C. Masmaliyeva, and G. N. Murshudov, "Resolution and resolvability in one, two and three dimensions," *Journal of Life Sciences and Biomedicine*, vol. 1, no. 1, pp. 29–36, 2019.

[5] D. Fernandez Comesaña, K. R. Holland, and E. Fernandez-Grande, "Spatial resolution limits for the localization of noise sources using direct sound mapping," *Journal of Sound and Vibration*, vol. 375, pp. 53–62, 2016.

[6] N. Vukmirović, M. Erić, M. Janjić, and P. M. Djurić, "Direct wideband coherent localization by distributed antenna arrays," *Sensors*, vol. 19, no. 20, p. 4582, 2019.

[7] N. Vukmirović, M. Erić, and P. M. Djurić, "Performance limits of direct wideband coherent 3d localization in distributed massive mimo systems," *Sensors*, vol. 21, no. 10, p. 3401, 2021.

Performance analysis of LDPC and Polar codes for message transmissions over different channel models

Darija Čarapić, Mirjana Maksimović and Miodrag Forcan

***Abstract*— The realization of a wireless communication system that will meet the demands of the modern world in terms of fast, secure, reliable, and cost-effective information exchange, is a challenging task. Having in mind that the transmission of data takes place in an imperfect channel environment where noise, fading, and interference are present, the achievement of timely communication with a minimum of errors during data transfer requires the right choice of the channel coding scheme. Channel coding is a fundamental component of the communication system and is intended to ensure that the information received is the same as the sent one. Two coding schemes are available in the fifth generation of mobile communications (5G): Low-Density Parity-Check (LDPC) codes for coding user information and Polar codes for coding control information. This paper presents a comparative simulation study of LDPC and Polar codes for message transmissions over different channel models (Additive White Gaussian Noise (AWGN), Rician, and Rayleigh). The Bit Error Rate (BER) performance of these codes was reviewed for all three channel models. The simulations considered variable message sizes and code rates for LDPC and Polar codes, different modulation patterns for LDPC codes, and different decoding schemes for Polar codes. The results of the simulations showed the performances of the LDPC and Polar codes in the case of channel models: AWGN with no fading and AWGN with fading. The LDPC codes have been superior in the case of long messages and the Polar codes have been more efficient in the case of short messages, hence justifying the use of both LDPC and Polar codes within the 5G.**

***Index Terms*— LDPC, Polar, BER, AWGN, Rician, Rayleigh**

I. INTRODUCTION

A communication medium is prone to errors due to random noise, interference, fading, device impairments, etc. Channel impairments lead to the corruption of the original data flow, so the data on the receiving side is not the same as the data that was sent. To correct the errors made during data transmission, channel coding is applied. This means that on the transmitter side, the original data flow is subjected to a series of algorithmic operations (channel encoding). On the receiver side, channel decoding is done by applying other operations set to correct errors. It is obvious that the choice of an adequate coding scheme is of paramount importance for the rapid and reliable transmission of data. Enhanced flexibility, low computation complexity, low latency, low cost, and high reliability are desired features for the coding scheme [1, 2].

In contrast to the previous generations of mobile communication systems (3G and 4G), which used Turbo code as a channel coding technique, the fifth generation of mobile communications (5G) introduces two coding techniques: Low-Density Parity-Check (LDPC) and Polar codes. The reasons Turbo code is not chosen for the 5G are numerous iterations and a significant delay in decoding. As such, Turbo codes are unable to meet the demands of 5G networks in terms of high speed and low delay. LDPC and Polar codes are chosen as 5G channel coding standards due to their features and because the unique coding technology can no meet the needs of all scenarios and users in 5G. LDPC codes have better band utilization, and they perform better for longer block lengths in comparison with Polar codes that are superior for shorter block lengths. Furthermore, compared to other codes, LDPC codes have better decoding latency, throughput, and implementation while Polar codes are simple to implement, can reach the channel capacity and have low encoding and decoding complexity [3]. According to 3rd Generation Partnership Project (3GPP) 5G New Radio (NR) standardization, LDPC coding scheme is proposed for use in data channels while Polar codes are applied in control channels [4].

This paper presents an attempt to simulate the performances of LDPC and Polar codes in the case of different channel models (Additive White Gaussian Noise (AWGN), Rician fading + AWGN, and Rayleigh fading + AWGN) in order to summarize the advantages and disadvantages of 5G channel coding techniques. A comparative simulation study is performed for variable message sizes and code rates. Moreover, different modulation schemes were analyzed in the case of LDPC codes as well as different decoding schemes for Polar codes.

Therefore, the paper is organized in the following manner. A short overview of communication channel models is presented in Section II. Section III presents 5G channel coding schemes while the results of simulations (Bit Error Rate (BER) vs Signal-to-Noise Ratio (SNR) graphs) are given in Section IV. A summary of the performed research and directions for future research are provided in the Conclusion.

II. COMMUNICATION CHANNEL MODELS

The theory of communication is often based on the assumption that the transmitted signals are distorted by a certain noise. The most commonly used noise assumption is additive, white, with Gaussian-distributed values. The

Darija Čarapić is with the m:tel a.d. Banja Luka, Bosnia and Herzegovina, (e-mail: darija_carapic@yahoo.com).

Mirjana Maksimović is with the Faculty of Electrical Engineering, University of East Sarajevo, Vuka Karadžića 30, 71123 East Sarajevo, Bosnia and Herzegovina (e-mail: mirjana.maksimovic@etf.ues.rs.ba).

Miodrag Forcan is with the Faculty of Electrical Engineering, University of East Sarajevo, Vuka Karadžića 30, 71123 East Sarajevo, Bosnia and Herzegovina (e-mail: miodrag.forcan@etf.ues.rs.ba).

model of AWGN channel is used to simulate the influence of naturally occurring random signals on wireless signals. It typically represents the background noise, amplifier noise in the transceivers, and signals from other communication systems in the frequency bands [5].

It is important to highlight that fading, frequency selectivity, interference, non-linearity, or dispersion are not considered in the AWGN channel model what makes it unrepresentative for most wireless connections. A more realistic scenario of wireless channels is the availability of multiple paths between transmitters and receivers. These routes can be direct or formed through reflection, diffraction, or scattering. In this case, the receiver receives distinct copies of the sent signal (with variable attenuation, delay, or phase shift) [6, 7]. Rayleigh distribution (for the scenario when no Line of Sight (LoS) component is present) and Rician distribution (when LoS component is present) are often used to represent multipath fading in wireless communication systems. In the Rician channel model, a receiver receives a direct LoS signal from the source in addition to the other non-LOS components. Rayleigh fading is considered as a special case of Rician. The receiver cannot receive any LoS signal directly from the source. All incoming signals are diffracted, reflected, or diffused. Rayleigh fading channel model is the right choice when there are several objects in the surroundings that scatter the signal before it reaches the receiver [8].

III. 5G CHANNEL CODING SCHEMES

Data transmission over the wireless communication link that is subject to interference and fading can result in the data received is different than the data sent. In order to overcome this problem, additional information is added to the data sent by the transmitter. At the receiver side, complex schemes that need sophisticated algorithms decode this information and retrieve the original data. This process is called Forward Error Correction (FEC) or channel coding and has an immense role in increasing the performance of wireless communication systems.

3GPP 5G NR brings requirements to channel coding at a completely new level. 5G is designed to serve a wide range of applications: enhanced mobile broadband (eMBB), ultra-reliable and low-latency communication (URLLC), and massive machine-type communication (mMTC) [9].

5G introduces the two capacity-achieving channel coding schemes, LDPC and Polar codes, not used in earlier generations of mobile communication systems. Hence, in the 5G communication systems, the channel coding has been separated into channel coding of user information (LDPC coding) and channel coding of control information (Polar coding).

A. LDPC codes

LDPC codes are a sort of linear block code first proposed by Gallager in the early 1960s [10] and rediscovered in the late 1990s thanks to MacKay [11, 12]. The name of these codes comes from the fact that their parity-check matrix is largely zeros (0s) with a minor number of ones (1s). LDPC codes can be described via matrices or represented graphically (Tanner graphs). There are two basic graphs and eight sets of lifting sizes in the 5G NR, hence allowing a variety of block lengths and coding rates. Graph structure sparsity has a strong influence on the algorithmic efficiency of LDPC codes. According to [13], it is not difficult to construct effective LDPC codes. Actually, the random codes have a high probability of success. The issue is that the encoding complexity of these codes is typically quite high. Decoding algorithms for LDPC codes are relatively simple and practical. The belief propagation algorithm, the message passing algorithm, and the sum-product algorithm are the most commonly used [13, 14]. The main advantages of LDPC codes are good block error performance, error floors in much lower BER values, the ability to achieve good error performance without requiring interleavers, and an iterative-based decoding process [15]. Because LDPC codes perform close to a channel's Shannon limit only for long block lengths, they are well suited for use in 5G NR for user data transmission.

3GPP specifies LDPC coding chains for the 5G NR downlink shared transport channels (DL-SCH) and uplink shared transport channels (UL-SCH) [4]. In 5G NR, data are transmitted in units referred to as transport blocks. The term "transport blocks" refers to data sent from the Medium Access Control (MAC) layer to the physical layer. A transport block goes through the processing steps shown in Fig. 1 before transmitting to the Physical Downlink Shared Channel (PDSCH) for scrambling, modulation, layer mapping, and resource/antenna mapping.

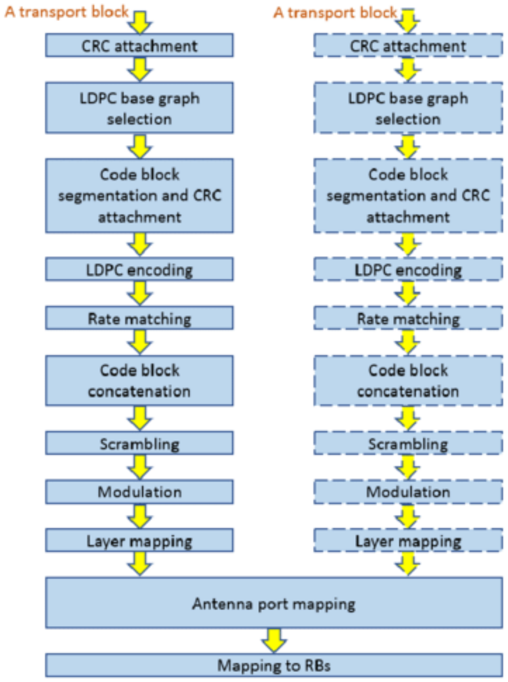

Fig. 1. 5G NR PDSCH physical layer processing [16]

PDSCH is used for a variety of data transmissions, including downlink user data, user equipment specific higher layer information, system information blocks, and paging [16]. Depending on the link conditions, the PDSCH employs an adaptive modulation format (QPSK, 16-QAM, 64-QAM, and 256-QAM). It also employs a flexible coding scheme. When these elements are combined, it results in a flexible coding and data rate [17]. The Physical Uplink Shared Channel (PUSCH) is the PDSCH's counterpart. PUSCH transmits an uplink shared channel (UL-SCH) and its higher mapped channel data. The physical layer of an uplinked transport block is processed similarly to that of a downlinked transport block (Fig. 2). PUSCH also has a very adaptable format. Frequency resources are allocated using blocks of resources as well as a flexible modulation (pi/2-BPSK, QPSK, 16-QAM, 64-QAM, and 256-QAM) and coding scheme depending on the link conditions [16, 17].

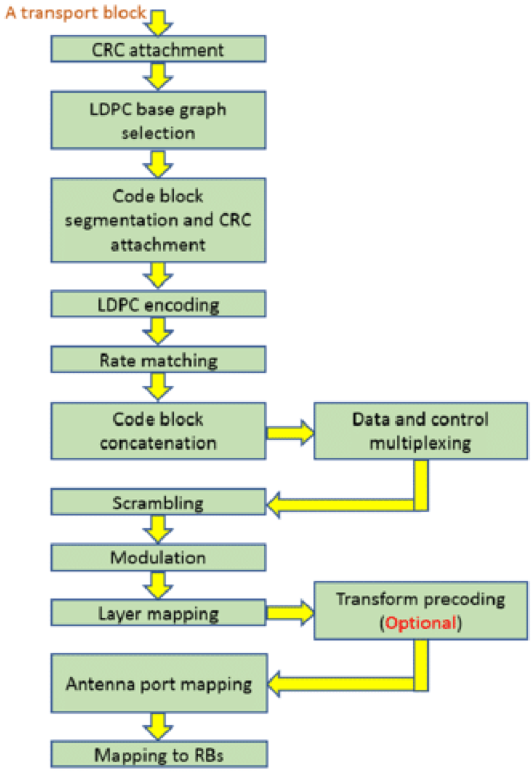

Fig. 1. 5G NR PUSCH physical layer processing [16]

B. Polar codes

Polar codes are another official channel coding scheme accepted in 5G standardization. The idea behind Polar codes, introduced by Arikan [18] in 2009, is to subdivide the original channel into a number of virtual channels, each of which is purely noisy or noiseless. By sending data over noise-free channels while the fixed bits, which are known at both the encoder and decoder, are sent over noisy channels, nearly error-free transmission is possible [19]. Polar codes are applied as channel codes for 5G NR control channels (Physical Downlink Control Channel (PDCCH) and Physical Uplink Control Channel (PUCCH)) where blocks of information are small, and the Hybrid Automatic Repeat Request (HARQ) is not used [14].

As indicated by the name, the 5G PDCCH transports downlink control information (DCI). Its main function is to schedule downlinking transmissions on the PDSCH as well as uplinking data transmissions on the PUSCH. With the exception of small data packets, the PDCCH employs QPSK as a modulation format and Polar coding as a coding scheme [17]. 5G NR PDCCH physical layer processing steps are shown in Fig. 3. It is important to point out that for downlink transmission, the size of the transport block is limited to 36-164 bits (interleaver limit).

The main purpose of PUCCH is to carry Uplink Control Information (UCI) such as HARQ feedback, channel state information, and scheduling request. The PUCCH employs BPSK or QPSK as a modulation format. As a coding scheme, PUCCH uses Polar coding. In the uplink transmission, the size of the transport block is limited to 31-1024 bits. If the payload size is greater than or equal to 1013 bits, code block segmentation for uplink is carried out [16].

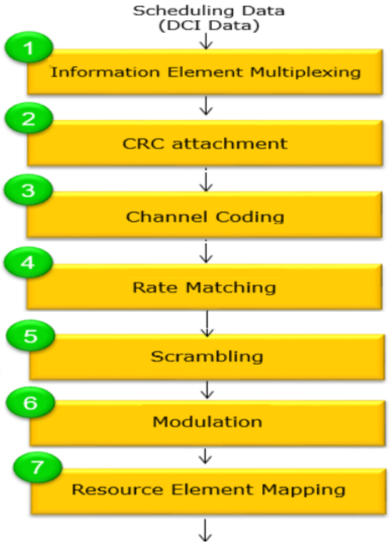

Fig. 3. 5G NR PDCCH physical layer processing [20]

As a starting point for Polar decoding, Arikan proposed decoding using successive cancellation (SC). Despite the advantage of low complexity, it is not adequate for block lengths ranging from short to medium. This problem can be solved by using the successive cancellation list (SCL) decoding algorithm. The SCL decoder uses a list size parameter L (the number of decoding paths that are most likely to be retained) to decode the input bits one by one. In 5G error-correction performance evaluations, Cyclic Redundancy Check (CRC)-aided SCL has been used. Although SCL's effectiveness increases as the list size parameter L increases, so does its implementation complexity. SCL becomes SC when L is set to 1 [14, 21].

IV. 5G CHANNEL CODING SCHEMES' BER PERFORMANCE

The MATLAB R2020a software package [22] was used to simulate the 5G physical communication layer with LDPC and Polar coding schemes. The downlink and uplink coding schemes are implemented in accordance with 3GPP regulations [4]. The performance of BER is analyzed for different message lengths (50, 500, 5000, and 50000 bits) and variable code rates using different communication channels: AWGN, Rician, and Rayleigh. The variances of AWGN channel model are estimated using SNR values. In the case of fading presence, a fading channel block was accompanied by the AWGN channel block that had previously been used. Fading channel property values used in simulations are: sampling rate: 10^5 [s]; path delays: 0, 10^{-7} and 10^{-5} [s] (for the outdoor environment); average path gains: 0, -3, and -3 [dB]; a maximum Doppler shift of 0; and the Rician K factor is set to 3 (K is the power of the LoS component divided by the power of the scattered components) [14, 23]. BER is calculated and plotted against the SNR. Each simulation was performed for 500 frames and continued until the BER of 10^{-6} is achieved. QPSK has been used in all simulations [23].

A. LDPC codes

Fig. 4 shows BER vs SNR graph for LDPC coded uplink transmission (quite similar simulation results are obtained for downlink transmission). Fig. 4. a) presents BER performance for messages of different lengths (50 bits and 5000 bits). The selected code rate is ½. As can be seen, for the longer message LDPC shows better performance. BER performance for different code rates is given in Fig. 4. b). The simulation is performed for 500 bits long message in the uplink direction. Simulation results demonstrate that the lowest code rate means the longest coded word and better BER performance. Since LDPC codes show better performance for longer words, Fig. 4. c) presents BER vs SNR graph for 5000 bits long message in case of different modulation techniques. In uplink directions, pi/2-BPSK, QPSK, 16-QAM, 64-QAM, and 256-QAM modulation schemes are supported while the opposite direction supports QPSK, 16-QAM, 64-QAM, and 256-QAM modulation schemes. Obtained results show the best performance for pi/2-BPSK and QPSK modulation schemes. Since pi/2-BPSK is not supported in both directions, all other simulations have been performed using QPSK modulation scheme.

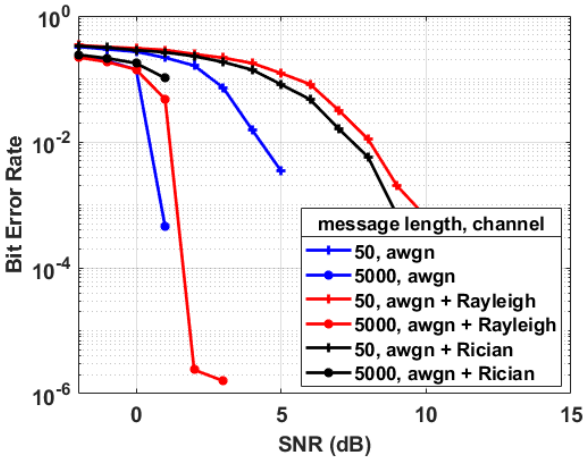

a) variable message length (code rate=1/2);

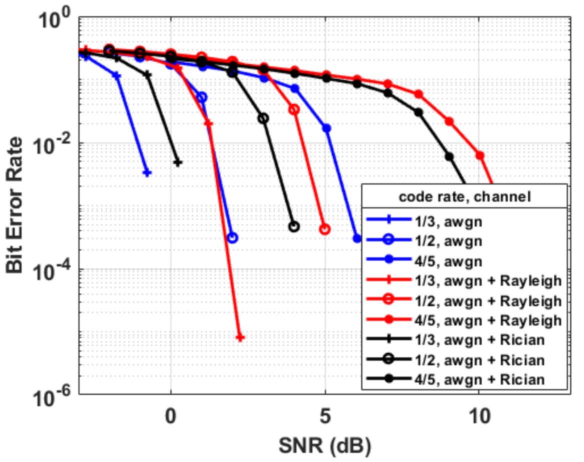

b) variable code rates (message length =500 bits);

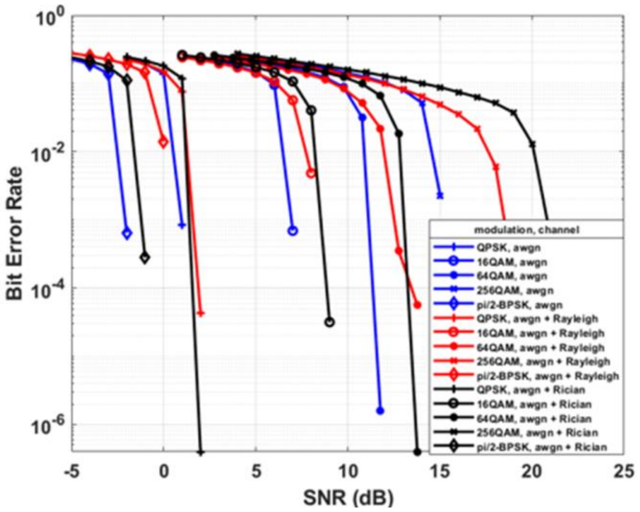

c) different modulation techniques (message length =5000 bits)

Fig. 4. BER performance for LDPC coded uplink data transmission

The common feature of all three graphs in Fig. 4 is that the AWGN channel model achieves the best performance, and the Rayleigh channel model achieves the worst. This is because the performance of the BER is considerably improved in the case of low SNR, but not in the case of high SNR. White Gaussian noise dominates the BER error when SNR is low. In this case BER performance can be improved by increasing SNR. However, when the SNR is high, the phase estimation error dominates the BER error. Simply increasing the SNR will not improve BER performance in this case [8].

B. Polar codes

A similar simulation study was also conducted in the case of Polar codes. Fig. 5 shows the BER vs SNR graphs for uplink transmission of Polar coded messages. Fig 5. a) considers different message lengths (50 bits and 500 bits). Uplink transmission of a longer message is not supported according to 3GPP (the maximum size of input length is 1023 bits). Among selected message lengths, BER performance simulation in downlink directions can be done only for a 50 bits long information message since the maximum input length is 164 bits. Fig. 5. a) results have been achieved for code rate = 1/2. As can be seen, opposite to LDPC, Polar codes show better performance for shorter messages. Since Polar codes show better performances for a shorter message, Fig. 5. b) shows the BER performance for 50 bits long message in case of different code rate values. The best results are achieved for the lowest code rate. Fig. 5 c) shows the simulation results for the CRC-aided SCL decoding algorithm. Variable list sizes *L* (4, 16) have been considered for code rate = 1/2. Results confirm that the larger list size *L* means enhanced Polar coding performance (lower error rate), but implementation complexity increases with higher *L* values.

The same as in the LDPC case, the best simulation results are achieved for the AWGN channel. The Rician channel model outperforms the Rayleigh use case in terms of BER.

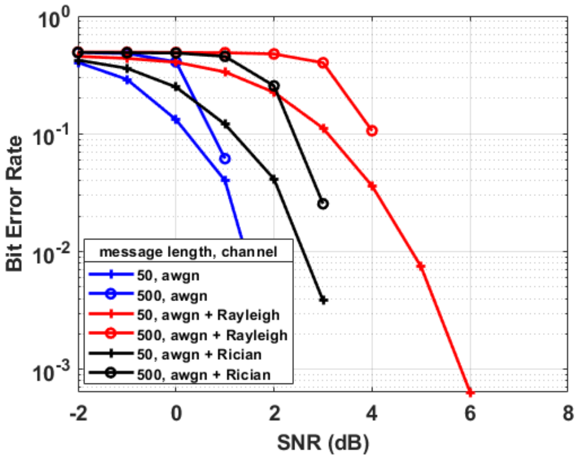

a) variable message length (code rate=1/2);

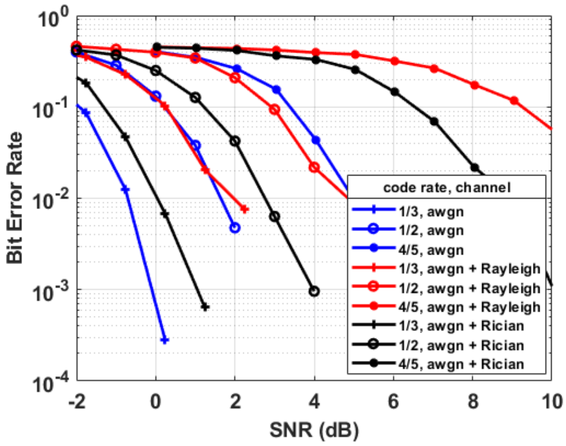

b) variable code rates (message length =500 bits);

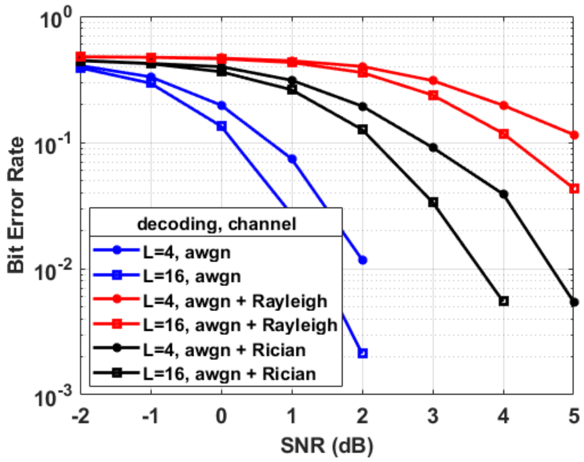

c) different *L* values (message length =50 bits)

Fig. 5. BER performance for Polar coded uplink data transmission

C. LDPC vs Polar codes

Fig. 6 demonstrates a comparison of LDPC and Polar coding techniques in both directions. Fig 6. a) shows BER vs SNR graph for uplink data transmission of 50- and 500 bits messages. Simulation results are achieved for code rate = 1/2, and show that LDPC codes have better performances for longer messages while Polar codes are superior in the case of short messages. Fig. 6 c) considers downlink transmission and knowing that the information message length, in this case, is limited to 164 bits, comparative analysis has been performed only for 50 bits long message. Polar codes outperform LDPC codes because messages are shorter. Fig 6. b), and d) present BER performance for 50 bits long message in case of variable code rates in both directions. For 50 bits long message, Polar codes are better than LDPC in both uplink and downlink directions and at lower code rates show better performance. Following the results from Fig. 6 a), it is evident that the LDPC would have better performance in the uplink transmission of a longer message. In all simulations, the best results are achieved for the AWGN channel model. When comparing fading channel models, the Rician channel model shows better performance in comparison with the Rayleigh channel model.

V. CONCLUSION

Recognizing the importance of selecting the right channel coding scheme to ensure fast and error-free transmission of data, this paper presents an attempt to conduct a comparative simulation study of 5G channel coding techniques. The performance of the LDPC and Polar codes is studied for three channel models (AWGN, Rician, and Rayleigh) taking into consideration the size of the messages and variable code rates. Performance of 5G channel coding techniques is measured by their ability to correct errors at a given SNR. The results have confirmed LDPC codes' superiority for longer messages and Polar codes' superiority for short messages. In this way, using LDPC codes in data channels and Polar codes in control channels is justified. In addition, for lower SNR values, Gaussian noise dominates the BER error and just improving the SNR, BER error can be improved. For higher SNR values, this cannot be performed as the phase estimation error dominates the BER error. That is why the simulation results have shown that BER performance of the AWGN channel model is better than for fading channel models. Apart from measuring the performance of a channel coding techniques via BER vs SNR graphs, it is also important to analyze the maximum possible throughput, latency and the resources and power consumption. This is the direction of our future research.

REFERENCES

[1] M. Maksimovic and M. Forcan, “Application of 5G Channel Coding Techniques in Smart Grid: LDPC vs. Polar coding for Command Messaging,” *7th International Conference on Electronics, Telecommunications, Computing, Automatics and Nuclear Engineering - IcETRAN* 2020, TEI 1.3.1-1.3.6.

[2] D. Čarapić and M. Maksimović, “A Comparison of 5G Channel Coding Techniques – LDPC and Polar codes“, *IJEEC*, Vol.4., No. 2. (2020), pp. 71-82.

[3] S. Cheng, “Comparative Study on 5G Communication Channel Coding Technology”, 3rd International Conference on Mechatronics Engineering and Information Technology (ICMEIT 2019), *Advances in Computer Science Research*, Vol. 87, pp. 74-77, 2019.

[4] 3GPP TS 38.212 V15.8.0 (2019-12) 3rd Generation Partnership Project; Technical Specification Group Radio Access Network; NR; Multiplexing and channel coding (Release 15)

[5] S. Host, “Gaussian Channel,” in *Information and Communication Theory* , IEEE, 2019, pp.237-263, doi: 10.1002/9781119433828.ch9

[6] H. Zarrinkoub, *Understanding LTE with MATLAB: from mathematical foundation to simulation, performance evaluation and implementation*, John Wiley & Sons, Ltd, 2014

[7] M. K. Samimi, G. R. Maccartney, S. Sun, and T. S. Rappaport, “28 GHz millimeter-wave ultrawideband small-scale fading models in wireless channels,” in *Proceedings of the 83rd IEEE Vehicular Technology Conference, VTC Spring 2016*, May 2016.

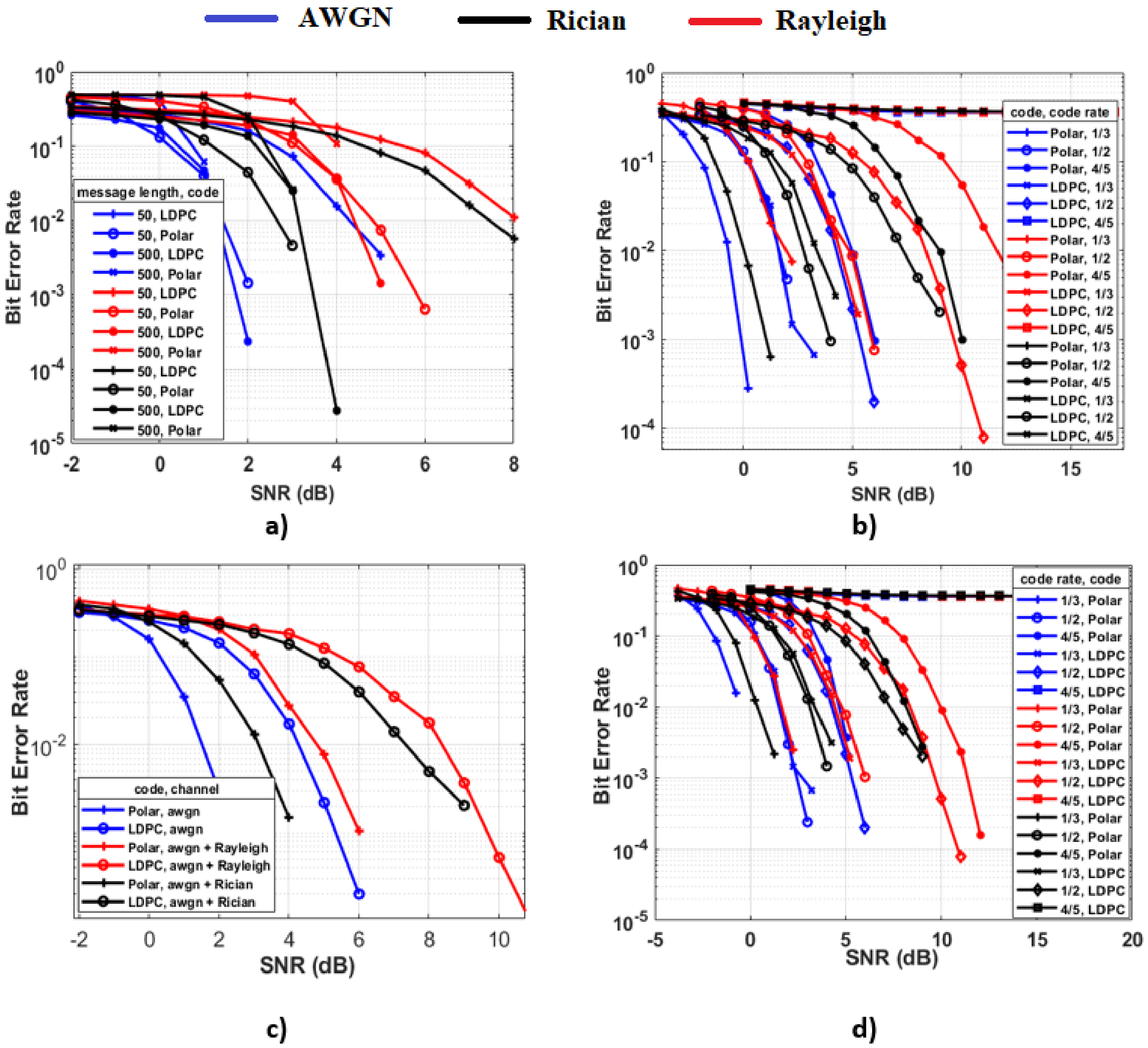

Fig. 6. BER performance – LDPC vs. Polar codes: a) variable message length (code rate=1/2) - uplink; b) variable code rates (message length =50 bits) - uplink; c) message length 50 bits (code rate=1/2) - downlink; d) variable code rates (message length =50 bits) – downlink.

[8] M.S. Chavan, R.H. Chile and S.R. Sawan "Multipath Fading Channel Modeling and Performance Comparison of Wireless Channel Models," *International Journal of Electronics and Communication Engineering*, Vol. 4, Number 2 (2011), pp. 189-203

[9] 3GPP: TR 38.913 Study on Scenarios and Requirements for Next Generation Access Technologies, 2017.

[10] R.G. Gallager, *Low-Density Parity-Check Codes*. Cambridge, MA: MIT Press, 1963

[11] D.J.C. MacKay and R. M. Neal, "Near Shannon limit performance of low density parity check codes." *In Electron. Letters*, Vol.32, August 1996, 1645-1646 (reprinted with printing errors corrected in Vol.33, 457–458)

[12] D.J.C. MacKay, "Good error-correcting codes based on very sparse matrices," *IEEE Transactions on Information Theory*, 1999, 45(2):399-431

[13] B.M.J. Leiner, *LDPC Codes – a brief Tutorial*, [Online]: Available: http://www.bernh.net/media/download/papers/ldpc.pdf

[14] M. Maksimovic and M. Forcan, "5G New Radio channel coding for messaging in Smart Grid," *Sustainable Energy, Grids and Networks*, Vol. 27, 2021, 100495

[15] I. Develi, and Y. Kabalci, "A comparative simulation study on the performance of LDPC coded communication systems over Weibull fading channels," *J. appl. res. Technol*, vol.14, no.2, 2016, https://doi.org/10.1016/j.jart.2016.04.001

[16] X. Lin *et al*., "G New Radio: Unveiling the Essentials of the Next Generation Wireless Access Technology," in *IEEE Communications Standards Magazine*, vol. 3, no. 3, pp. 30-37, 2019, doi: 10.1109/MCOMSTD.001.1800036.

[17] Electronics Note, *5G Data Channels: Physical; Transport; & Logical*, [Online]: Available at: https://www.electronics-notes.com/articles/connectivity/5g-mobile-wireless-cellular/data-channels-physical-transport-logical.php

[18] E. Arikan, "Channel Polarization: A method for constructing capacity-achieving codes for symmetric binary-input memoryless channels," in *IEEE Transactions on Information Theory*, 55(7):3051–3073, 2009

[19] K. Niu, K. Chen, J. Lin and Q. T. Zhang, "Polar codes: Primary concepts and practical decoding algorithms," in *IEEE Communications Magazine*, vol. 52, no. 7, pp. 192-203, July 2014, doi: 10.1109/MCOM.2014.6852102.

[20] Sharetechnote, *5G/NR – PDCCH*, [Online]: Available at: http://www.sharetechnote.com/html/5G/5G_PDCCH.html

[21] V. Bioglio, C. Condo and I. Land, "Design of Polar Codes in 5G New Radio," in *IEEE Communications Surveys & Tutorials*, vol. 23, no. 1, pp. 29-40, 2021, doi: 10.1109/COMST.2020.2967127.

[22] MATLAB, 2020. version R2020a, Natick, Massachusetts: The MathWorks Inc.

[23] D. Čarapić, *Analysis of 5G channel coding techniques*, Master Thesis, University of East Sarajevo, Faculty of Electrical Engineering, June 2021.